Age-Related Macular Degeneration (AMD) - Investigations into the Molecular Mechanisms of Genetic Associations

DISSERTATION ZUR ERLANGUNG DES
DOKTORGRADES DER NATURWISSENSCHAFTEN
(DR. RER. NAT.)
DER FAKULTÄT FÜR BIOLOGIE
UND VORKLINISCHE MEDIZIN
DER UNIVERSITÄT REGENSBURG

vorgelegt von
Christina Kiel
aus Landshut

im Jahr 2021

Das Promotionsgesuch wurde eingereicht am:
24.03.2021

Die Arbeit wurde angeleitet von:
Prof. Dr. Bernhard H.F. Weber

_____

Christina Kiel

Age-Related Macular Degeneration (AMD) - Investigations into the Molecular Mechanisms of Genetic Associations

DISSERTATION ZUR ERLANGUNG DES
DOKTORGRADES DER NATURWISSENSCHAFTEN
(DR. RER. NAT.)
DER FAKULTÄT FÜR BIOLOGIE
UND VORKLINISCHE MEDIZIN
DER UNIVERSITÄT REGENSBURG

vorgelegt von
Christina Kiel
aus Landshut

im Jahr 2021

Parts of this work have been published in the following peer-reviewed journals:

First or shared first authorship

Grassmann F*, Kiel C*, Zimmermann ME, Gorski M, Grassmann V, Stark K, et al. (2017). Genetic pleiotropy between age-related macular degeneration and 16 complex diseases and traits. Genome Med. 9(1): 29. DOI: 10.1186/s13073-017-0418-0.

* These authors contributed equally to this work.

Contribution: Data generation, data analysis, data visualization, contribution to writing of a first draft of the manuscript.

Kiel C, Weber BHF, Grassmann F (2018). Pleiotropic Effects of Risk Factors in Age-Related Macular Degeneration and Seemingly Unrelated Complex Diseases. Adv Exp Med Biol. 1074: 247-255. DOI: 10.1007/978-3-319-75402-4_30.

Contribution: Review – Literature search and contribution to writing of a first draft of the manuscript.

Strunz T*, Lauwen S*, Kiel C*, International AMD Genomics Consortium (IAMDGC), den Hollander AI, Weber BHF (2020). A transcriptome-wide association study based on 27 tissues identifies 106 genes potentially relevant for disease pathology in age-related macular degeneration. Sci Rep. 10(1): 1584. DOI: 10.1038/s41598-020-58510-9.

* These authors contributed equally to this work.

Contribution: Data generation and analysis of pleiotropic effects of AMD-associated genes detected in the transcriptome-wide association study, data visualization, contribution to writing of a first draft of the manuscript.

Kiel C*, Berber P*, Karlstetter M*, Aslanidis A, Strunz T, Langmann T, et al. (2020). A Circulating MicroRNA Profile in a Laser-Induced Mouse Model of Choroidal Neovascularization. Int J Mol Sci. 21(8): 2689. DOI: 10.3390/ijms21082689.

* These authors contributed equally to this work.

Contribution: Methodology, data generation, data analysis, data visualization, contribution to writing of a first draft of the manuscript.

Kiel C*, Strunz T*, International AMD Genomics Consortium (IAMDGC), Grassmann F, Weber BHF (2020). Pleiotropic locus 15q24.1 reveals a gender-specific association with neovascular but not atrophic age-related macular degeneration (AMD). Cells. 9(10): 2257. DOI: 10.3390/cells9102257.

* These authors contributed equally to this work.

Contribution: Conceptualization, study design, data analysis, data visualization, as well as writing of a first draft of the manuscript.

Strunz T*, Kiel C*, Sauerbeck BL, Weber BHF (2020). Learning from fifteen years of genome-wide association studies in age-related macular degeneration. Cells. 9(10): 2267. DOI: 10.3390/cells9102267.

* These authors contributed equally to this work.

Contribution: Conceptualization, methodology, and study design, as well as contribution to writing of a first draft of the manuscript.

Kiel C*, Nebauer CA*, Strunz T*, Stelzl S, Weber BHF (2021). Epistatic interactions of genetic loci associated with age-related macular degeneration. Sci Rep. 11(1): 13114. DOI: 10.1038/s41598-021-92351-4.

* These authors contributed equally to this work.

Contribution: Conceptualization, methodology, study design, data visualization, as well as contribution to writing of a first draft of the manuscript.

Kiel C, Strunz T, Hasler D, Meister G, Grassmann F, Weber BHF (2021). Seed sequence polymorphism rs2168518 and allele-specific target gene regulation of hsa-miR-4513. Hum Mol Genet. ddab292. DOI: 10.1093/hmg/ddab292.

Contribution: Conceptualization, methodology, study design, data analysis, data visualization, as well as writing of a first draft of the manuscript.

Manuscripts with contribution

Berber P, Grassmann F, Kiel C, Weber BHF (2017). An Eye on Age-Related Macular Degeneration: The Role of MicroRNAs in Disease Pathology. Mol Diagn Ther. 21(1): 31-43. DOI: 10.1007/s40291-016-0234-z.

Contribution: Data processing, data visualization.

Grassmann F, Kiel C, den Hollander AI, Weeks DE, Lotery A, Cipriani V, et al. (2018). Y chromosome mocaicism is associated with age-related macular degeneration. Eur J Hum Genet. 27(1): 36-41. DOI: 10.1038/s41431-018-0238-8.

Contribution: Data processing.

Grassmann F, Harsch S, Brandl C, Kiel C, Nürnberg P, Toliat MR, et al. (2019). Assessment of Novel Genome-Wide Significant Gene Loci and Lesion Growth in Geographic Atrophy Secondary to Age-Related Macular Degeneration. JAMA Ophthalmol. e191318. DOI: 10.1001/jamaophthalmol.2019.1318.

Contribution: Data processing.

Winkler TW*, Grassmann F*, Brandl C, Kiel C, Günther F, Strunz T, et al. (2020). Genome-wide association meta-analysis for early age-related macular degeneration highlights novel loci and insights for advanced disease. BMC Med Genomics. 13(1): 120. DOI: 10.1186/s12920-020-00760-7.

* These authors contributed equally to this work.

Contribution: Data generation, data analysis.

Strunz T, Kiel C, Grassmann F, Ratnapriya R, Kwicklis M, Karlstetter M, et al. (2020). A mega-analysis of expression quantitative trait loci in retinal tissue. PLoS Genet. 16(9): e1008934. DOI: 10.1371/journal.pgen.1008934.

Contribution: Data generation, data analysis.

Table of contents

Zusammenfassung 1
Summary 4
1 Introduction 6
1.1 Age-related macular degeneration (AMD) 6
1.2 Genome-wide association studies (GWAS) 8
1.3 The genetics of AMD 10
1.4 Pleiotropy 12
1.5 microRNAs (miRNA) 13
1.6 Aim of this study 15
2 Material 17
2.1 Escherichia coli (E. coli) Strains 17
2.2 Eukaryotic Cell Lines 17
2.3 Cell Culture Media and Supplements 17
2.4 Oligonucleotides Used for miRNA Mimic Transfection 18
2.5 Oligonucleotides Used for miRNA Detection *via* Quantitative Reverse Transcription PCR (qRT-PCR) 18
2.6 Oligonucleotides and Corresponding Probes Used for qRT-PCR 19
2.7 Oligonucleotides for PCR and Sequencing Reactions 21
2.8 Plasmids and Expression Constructs 23
2.9 Primary Antibodies 24
2.10 Secondary Antibodies 25
2.11 Enzymes 25
2.12 Kit Systems 25
2.13 Chemicals and Ready-Made Solutions 26
2.14 Buffers and Solutions 29
2.15 Consumables 30
2.16 Instruments 31
2.17 Software 34
3 Methods 35
3.1 Cell Culture 35
3.1.1 Cultivation of Primary Human Umbilical Vein Endothelial Cells (HUVEC) 35
3.1.2 Cultivation of Human Embryonic Kidney (HEK293T) Cells 35
3.1.3 Transfection of HUVECs 35
3.1.4 Co-Transfection of HEK293T Cells 36
3.2 Laser-induced neovascularization mouse model 36
3.3 RNA isolation 37
3.3.1 Isolation of miRNAs 37

3.3.2 Isolation of mRNA ... 37
3.4 cDNA Synthesis ... 37
3.4.1 polyA tailing and cDNA synthesis of miRNAs ... 37
3.4.2 cDNA synthesis of mRNA ... 38
3.5 Quantitative Reverse Transcription PCR (qRT-PCR) ... 39
3.5.1 Detection of miRNAs ... 39
3.5.2 Detection of mRNA ... 40
3.6 RNA sequencing (RNA-Seq) ... 40
3.6.1 Library preparation ... 40
3.6.2 RNA-Seq ... 41
3.7 Sodium dodecyl sulfate (SDS) Polyacrylamide Gel Electrophoresis ... 41
3.8 Western Blot ... 42
3.9 Generation of luciferase reporter constructs ... 42
3.9.1 Amplification of 3'-untranslated regions (3'-UTR) by PCR ... 42
3.9.2 Agarose gel electrophoresis ... 45
3.9.3 Purification of PCR products from agarose gels ... 45
3.9.4 Ligation into pGEM®-T ... 46
3.9.5 Heat shock transformation in *E. coli* ... 46
3.9.6 Plasmid DNA Miniprep ... 46
3.9.7 Sanger Sequencing ... 47
3.9.8 Restriction digestion ... 48
3.9.9 Dephosphorylation ... 48
3.9.10 Ligation in pmirGLO luciferase reporter vector ... 49
3.9.11 Colony PCR ... 49
3.9.12 Plasmid DNA "Midi" preparation ... 50
3.9.13 Preparation of glycerolstocks for long term storage ... 50
3.10 Dual-Luciferase reporter assay ... 50
3.11 Statistical evaluation ... 50
4 Bioinformatical protocols ... 52
4.1 Identification of altered cmiRNA expression in NGS data ... 52
4.2 Analysis of qRT-PCR data to replicate cmiRNAs and investigate miRNA expression in ocular tissue ... 52
4.3 Generation of a GWAS collection ... 53
4.4 Pleiotropy of AMD-associated genes ... 53
4.5 Description of datasets used to study associations with 15q24.1 ... 54
4.6 Association analysis of rs2168518 with AMD ... 54
4.7 Phenome-wide association analysis of rs2168518 in the UK Biobank dataset ... 55

4.8 Colocalization analysis 55
4.9 Functional annotation of genetic variants at 15q24.1 56
4.10 RNA-Seq analysis 56
4.11 Medical relevance of allele-specific target genes of hsa-miR-4513 57
5 Results 58
5.1 Identification of circulating miRNAs in a mouse model of NV - Workflow 58
5.1.1 Identification of altered cmiRNA expression by NGS 60
5.1.2 Replication of cmiRNAs by qRT-PCR 61
5.1.3 miRNA Expression in retinal and RPE/choroidal tissue 62
5.2 Pleiotropic effects of AMD-associated genes 63
5.3 Characterization of the AMD-associated pleiotropic locus at 15q24.1 68
5.3.1 Refinement of the genetic association signal of rs2168518 with AMD 69
5.3.2 Pleiotropic effect of 15q24.1 assessed in the UK Biobank data 72
5.3.3 Investigation of genetic variants at 15q24.1 regarding alterations in transcription factor binding sites 76
5.4 Influence of seed polymorphism rs2168518 in hsa-miR-4513 on post-transcriptional gene regulation 77
5.4.1 Overexpression of miRNA mimics in primary endothelial cells 78
5.4.2 Allele-specific target genes identified *via* RNA sequencing 79
5.4.3 Replication of allele-specific target genes 81
5.4.4 Validation of exemplary allele-specific target genes *via* Western Blot analysis 82
5.4.5 Validation of selected allele-specific target genes *via* luciferase reporter assay 84
5.4.6 Medical relevance of allele-specific target genes 88
6 Discussion 90
7 References 100
List of abbreviations 117
List of figures 119
List of tables 120
List of supplementary tables 122
Acknowledgements 123
Supplements 124

Zusammenfassung

Die Krankheitsentstehung wie auch die Progression der altersabhängigen Makuladegeneration (AMD) wird durch eine Vielzahl an genetischen sowie umweltbedingten Faktoren beeinflusst, was die AMD als eine sogenannte komplexe Erkrankung klassifiziert. Um den Beitrag der Genetik zu untersuchen wurden mehrere genetische Assoziationsstudien durchgeführt, die verschiedene Aspekte der Pathobiologie untersucht haben. Unter anderem wurden Assoziationen von genetischen Varianten, epigenetischen Regulatoren wie micro-RNAs (miRNA) und spezifischen Genen mit der AMD beschrieben. Die molekularen Mechanismen, die diesen Assoziationen zu Grunde liegen, sind bisher allerdings kaum bekannt. Aus diesem Grund befasst sich die vorliegende Arbeit mit der Fragestellung wie die Erkenntnisse von genetischen Assoziationsstudien zur Entschlüsselung von molekularen Mechanismen führen können, um die Pathologie der AMD zu verstehen und eventuell Zielmoleküle im Sinne einer Präzisionsmedizin offen zu legen.

Im ersten Teilprojekt wurden Assoziationen von epigenetischen Regulatoren mit der AMD untersucht, im Speziellen miRNAs. In einem Mausmodell mit Laser-induzierter choroidaler Neovaskularisation (NV), einem Subtyp der AMD mit schwerwiegenden Manifestationen, wurden drei zirkulierende miRNAs identifiziert (mmu-miR-486a-5p, mmu-miR-92a-3p und mmu-miR-155-5p), die nach der Induktion der NV eine veränderte Expression im Blut der behandelten Tiere aufwiesen. Zusätzlich wurde die Expression von zwei dieser miRNAs, mmu-miR-486a-5p und mmu-miR-92a-3p, im Augengewebe von gelaserten Mäusen untersucht. Beide miRNAs zeigten nach der Induktion der NV eine erhöhte Expression im retinalen Pigmentepithel (RPE)/Aderhaut Komplex, wohingegen keine der beiden miRNAs eine Expressionsveränderung in der Netzhaut aufwies.

Im zweiten Projekt dieser Arbeit wurden Gene, welche mit der AMD assoziiert sind, auf pleiotrope Effekte hin untersucht. Es wurden insgesamt 106 Gene analysiert, die durch eine aktuelle, das gesamte Transkriptom umfassende, Assoziationsstudie (TWAS) gefunden wurden. Bei der Analyse zeigte sich, dass 50 der untersuchten Gene in genomischen Bereichen liegen, die durch Genom-weite Assoziationsstudien (GWAS) bereits mit unterschiedlichen Phänotypen des Menschen assoziiert wurden. Insgesamt zeigte sich neben der AMD-Erkrankung selbst eine Anreicherung von AMD-assoziierten Genen in GWAS Genorten von neurologischen Erkrankungen, metabolischen Phänotypen, Autoimmunerkrankungen und Phänotypen die Organfunktionen beschreiben. Dabei lagen 23 Gene in GWAS Genorten, die eine Assoziation mit mehreren Phänotypen aufweisen, wodurch diese Gene als potenziell pleiotrop eingeordnet werden können. Interessanterweise lagen vier der 23 pleiotropen Gene in Genorten, die bisher nicht mit der AMD in Verbindung gebracht

wurden. Einer dieser vier Genorte wurde im Verlauf dieser Arbeit ausführlich beschrieben, und zwar 15q24.1, welcher das *ULK3* Gen beinhaltet.

Die Assoziation des 15q24.1 Genortes mit der AMD wurde anhand des repräsentativen Polymorphismus rs2168518 untersucht. Interessanterweise war die Assoziation vor allem für den neovaskulären Subtyp der AMD zu beobachten und zeigte des Weiteren einen geschlechtsspezifischen Effekt. Eine Pleiotropie-Analyse anhand der Daten des UK Biobank Projektes zeigte eine Assoziation von 15q24.1 mit 15 Phänotypen, wobei die meisten dieser Phänotypen mit der Regulation des Blutdruckes in Verbindung stehen. Die Tatsache, dass Blutdruck-Assoziationen des 15q24.1 Genortes auf dasselbe genetische Signal wie die AMD-Assoziation zurückzuführen ist, verdeutlicht noch einmal die Bedeutung des 15q24.1 Genortes für den neovaskulären Subtyp der AMD. Die spezifische Assoziation von 15q24.1 mit AMD in Männern könnte womöglich auf Veränderungen in Bindestellen für geschlechtsspezifische Transkriptionsfaktoren beruhen. Des Weiteren liegt der rs2168518 Polymorphismus in der Binderegion eines wichtigen post-transkriptionellen Regulators, der miRNA hsa-miR-4513, wodurch er möglicherweise einen Einfluss auf die durch die miRNA ausgeführte Expressionsregulation ausübt.

Daher wurde in einem weiteren Projekt dieser Arbeit der Einfluss des rs2168518 Polymorphismus auf die regulatorischen Eigenschaften von hsa-miR-4513 untersucht. Insgesamt wurden 23 Gene identifiziert und unabhängig validiert, die spezifisch durch ein Allel des rs2168518 Polymorphismus in hsa-miR-4513 reguliert werden. Des Weiteren wurden sechs Gene exemplarisch im Detail mittels Western Blot Analyse und Luciferase Reporter Assays untersucht. Drei der untersuchten Gene, *CD2BP2*, *CDKN2A* und *KLF6*, zeigten dabei durchgängig Allel-spezifische Effekte. Abschließend wurden öffentlich zugängliche Datenbanken einbezogen, um eine medizinische Relevanz der von hsa-miR-4513 regulierten Gene zu untersuchen. Diese *in silico* Analyse zeigte, dass *CDKN2A* ein vielversprechender Kandidat ist, der möglicherweise zur Pathologie der AMD beiträgt.

Zusammenfassend zeigten die Ergebnisse dieser Arbeit, dass eine Betrachtung von genetischen Assoziationen aus unterschiedlichen Blinkwinkeln mit Fokus auf verschiedene molekulare Mechanismen, wie zum Beispiel Pleiotropie oder Genexpression, unterschiedliche wichtige Aspekte der Krankheitspathobiologie, die einer genetischen Assoziation zu Grunde liegen können, aufdecken können. Dies kann unter Umständen auch zu der Identifikation von mehreren verschiedenen krankheitsrelevanten Genen führen, die aber nur durch eine spezifische Fragestellung identifiziert werden können. So wird außerdem verdeutlicht, wie wichtig umfassende und sich ergänzende *in silico* und *in vitro* Analysen sind, um funktionelle Mechanismen hinter den Assoziationssignalen aufzudecken. Nur wenn die Pathobiologie, die

genetischen Assoziationen zugrunde liegt, verstanden wird, können zukünftig neue Therapieansätze für die AMD entwickelt werden.

Summary

Age-related macular degeneration (AMD) is a complex disease which is characterized by the contribution of a variety of environmental and genetic factors to disease development and progression. In order to elucidate the genetic background of AMD, a broad range of association studies have been conducted, targeting different aspects of disease pathobiology. Those studies revealed associations of genetic variants, epigenetic regulators like microRNAs (miRNA) and also of specific genes with AMD. However, for most of these findings the molecular mechanism of action underlying the association still remains unsolved. Therefore, the present work aimed to investigate how the findings of genetic association studies can lead to the deciphering of molecular mechanisms in order to understand the pathology of AMD and possibly reveal target molecules with regard to precision medicine.

In the first subproject, associations of epigenetic regulators, specifically miRNAs, with AMD were investigated. In a mouse model of laser-induced choroidal neovascularization (NV), one of the subtypes of AMD with severe manifestations, three circulating miRNAs with an altered expression in blood were identified after NV induction, namely mmu-miR-486a-5p, mmu-miR-92a-3p and mmu-miR-155-5p. In addition, expression alterations of two of those miRNAs, mmu-miR-486a-5p and mmu-miR-92a-3p, were investigated in ocular tissue of laser-treated mice. Both miRNAs revealed an overexpression in retinal pigment epithelium (RPE)/choroid complex, while none of them was differentially expressed in the neural retina after NV induction.

In the second project of this work, genes associated with AMD were investigated regarding potential pleiotropy. In total, 106 genes found by a recent transcriptome-wide association study (TWAS) were analyzed. The analysis revealed that 50 of the investigated genes are located in genomic regions that have already been associated with different human phenotypes by genome-wide association studies (GWAS). Overall, AMD-associated genes were found to be enriched in GWAS loci of neurological diseases, metabolic phenotypes, autoimmune diseases, and phenotypes describing organ functions, in addition to AMD disease itself. Moreover, 23 genes overlapped with GWAS loci of different phenotype groups, thus most likely representing pleiotropic genes. Interestingly, four of those 23 genes did not overlap with a known AMD-associated locus. A locus harboring one of those genes, namely *ULK3* at 15q24.1, was further characterized in detail throughout this work.

The association of 15q24.1 with AMD was examined using the representative polymorphism rs2168518. Interestingly, the association was mainly observed for the neovascular subtype of AMD and further showed a gender-specific effect. A pleiotropy analysis using UK Biobank data highlighted associations with 15 phenotypes, most of them related to blood pressure. The fact that blood pressure associations of the 15q24.1 locus correspond to the same genetic signal

as the AMD association further highlights the importance of the 15q24.1 locus for the neovascular subtype of AMD. Additionally, alterations in gender-specific transcription factor binding sites might contribute to the male specific association with AMD. Noteworthy, the representative variant rs2168518 of the 15q24.1 locus is located in the seed region of a miRNA, hsa-miR-4513, and might therefore contribute to post-transcriptional expression regulation mediated through this miRNA.

The impact of hsa-miR-4513 and its seed variant rs2168518 on gene expression regulation was investigated in another project of this work. Overall, 23 target genes of this miRNA were detected and independently validated to be specifically regulated by an allele of the rs2168518 polymorphism in hsa-miR-4513. Moreover, six target genes were exemplary followed up in detail by Western Blot analysis and luciferase reporter assay, whereby three of those genes, namely *CD2BP2*, *CDKN2A* and *KLF6*, consistently revealed allele-specific effects. Finally, publicly available databases were incorporated to investigate medical relevance of hsa-miR-4513 target genes. This *in silico* analysis highlighted *CDKN2A* as a promising candidate potentially contributing to AMD pathology.

In summary, the results of this work showed that examining genetic associations from different perspectives focusing on different molecular mechanisms, such as pleiotropy or gene expression, can reveal different important aspects of disease pathobiology that may underlie a genetic association. In some circumstances, this can also lead to the identification of several different disease-relevant genes, which, however, can only be identified by a specific research question. Therefore, it is crucial to comprehensively investigate single genetic association signals with a combination of complementary *in silico* and *in vitro* analyses to link association data with functional mechanisms. Only by understanding the pathobiology underlying the genetic associations, the development of new therapeutic options for the pathology of AMD will be possible in the future.

1 Introduction

1.1 Age-related macular degeneration (AMD)

In 2015, approximately 200 million people worldwide were affected by age-related moderate to severe visual impairment or blindness [1]. The most frequent diseases concurrent with vision loss are cataract, under corrected refractive error, glaucoma as well as age-related macular degeneration (AMD). The prevalence of these diseases show strong regional differences, although generally the frequencies of glaucoma and AMD is greatest in high-income countries [2]. Attributable to the increasingly aging population structure, the number of visually impaired or even blind people is estimated to increase within the next decades [1,3]. While cataract, under corrected refractive error and glaucoma can be controlled relatively well, there are hardly any effective treatment options for AMD [4–7].

The manifestation of AMD is multifaceted and shows a progressive course. In the early and intermediate stages of AMD, extracellular lipid-rich deposits, so-called drusen, appear between the retinal pigment epithelium (RPE) and Bruch's membrane (**Figure 1A and B**) [5]. In addition, in intermediate AMD first abnormalities of the RPE, characterized by spots of hyperpigmentation and hypopigmentation, can occur [8,9]. These early stages of AMD are usually asymptomatic. However, first visual impairments include reduced visual acuity and non-specific blurred vision [10].

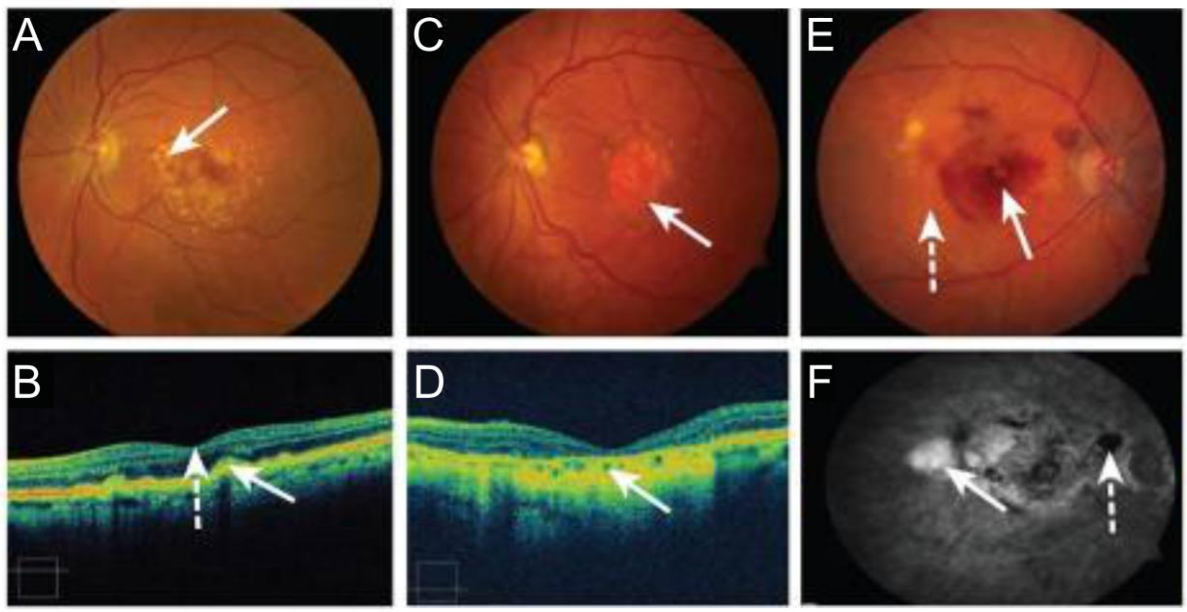

Figure 1. Pathological findings in age-related macular degeneration (AMD).

(A) Fundus photography image of a patient with early or intermediate AMD. The patient has large drusen (indicated with an arrow), but still exhibits good visual function. **(B)** Optical coherence tomography (OCT) image of the same patient with early or intermediate AMD as shown in A. The inner retina is pointing towards the top of the image, while the choroid is shown on the bottom of the image. The solid arrow indicates the location of drusen. The dashed arrow indicates the center of the fovea. **(C)** Fundus photography image of an AMD patient with geographic atrophy

(GA). The GA area centered on the macula. In the anthropic region the neuroretina, retinal pigment epithelium (RPE) and choriocapillaris are lost. Remaining large vessels of the choroid are visible within the atrophic area, as the pigmented RPE is missing (indicated by the solid arrow). **(D)** OCT image of the GA patient shown in C. The retina is thinned and the RPE and choriocapillaris in the center of the macular are lost (indicated by the solid arrow). **(E)** Fundus photography of an AMD patient with choroidal neovascularization (NV). The solid arrow indicates a region with subretinal hemorrhage and the dashed arrow indicates hard retinal exudates. **(F)** Fluorescein angiogram of a NV patient. The white area (solid arrow) shows a hyperfluorescence resulting from leakage of the fluorescein dye through abnormal neovascular complex growth. Hypofluorescence, as indicated by the dashed arrow, results from subretinal hemorrhage, which blocks the fluorescein dye (Figure modified from Swaroop et al., 2009 [8]).

The intermediate stage of AMD can progress to its late form, which leads to loss of central visual acuity and central vision. Late stage AMD can manifest in two different subtypes, the neovascular, which contains also choroidal neovascularization (NV), and the geographic atrophic (GA) form. Both subtypes can occur separately or simultaneously in the same eye [10]. The slower progressing GA is defined as a discrete area with a sharp border, in which depigmentation appears due to loss of photoreceptor cells, RPE and choriocapillaris (**Figure 1C and D**) [5,8]. Although loss of vision occurs gradually in GA, it results in significant deficits of visual function if the fovea is involved. In the NV subtype of AMD, choroidal vessels disrupt the Bruch's membrane, RPE and photoreceptors [5]. Moreover, those blood vessels are leaking blood and fluid, resulting in subretinal hemorrhage, fibrous scaring and retinal detachment (**Figure 1E and F**) [5,8,9]. Overall, NV-AMD is characterized by a more rapid loss of vision [5].

Unfortunately, so far treatment options for AMD are limited. While there is no treatment available for GA at present, the NV subtype can be treated by inhibition of the Vascular Endothelial Growth Factor A (VEGFA), an important angiogenic factor [5,10]. However, not all NV patients benefit from an anti-VEGFA therapy [5]. Further, this treatment can only stabilize or partly improve visual function [11], as it just treats the symptoms of the disease, but is no cure for AMD.

The pathology and etiology of AMD are influenced by both genetic and environmental risk factors, making AMD a complex disease. In addition to the strong risk factor age, which has become a part of the name of the disease, other environmental factors such as smoking were shown to also contribute to the etiology of the disease [12,13]. Nevertheless, in a twin study from 2005 the genetic contribution to AMD severity was estimated to be up to 71 % [14]. This highlights the importance of the genetic background for AMD etiology and pathology.

1.2 Genome-wide association studies (GWAS)

A common approach to investigate the genetic contribution to complex diseases is given by genome-wide association studies (GWAS). The simplicity of the study design, which allows investigation of thousands of individuals and millions of genetic variants in a large-scale approach, is a major advantage of GWAS. This large-scale analysis is achieved by the comparison of allele frequencies between individuals affected by the disease of interest *versus* non-affected but matched (for example age, ethnicity, regional closeness) controls. Furthermore, continuous phenotypic traits such as body height can be investigated. If a genetic variation occurs statistically more often in cases than in controls this variant is assumed to be associated with the disease [15,16]. This rather simple statistics made GWAS incredibly popular after the first successful GWAS provided a proof-of-principle in 2005 [17]. In September 2018 a publicly available GWAS database, called GWAS Catalog, included 5,687 studies for a plethora of phenotypes. Those studies reported 71,673 genetic variant - phenotype associations [18], distributed across the whole genome.

One reason for the success of GWAS is the relatively cost-effective implementation, as it is not necessary to sequence the whole genome. Genetic variants located in physical proximity on a chromosome are usually inherited together. This non-random pattern of inheritance is called linkage disequilibrium (LD), which is indicated by the squared correlation coefficient R^2 (**Figure 2**). In case genetic variants are always inherited together, they are in perfect correlation (perfect LD), which is indicated by a R^2 of 1. In contrast, independently inherited variants are not correlated. Accordingly, the R^2 value equals 0. This principle allows the application of proxy variants from which the allele frequency for correlated variants can be derived [19].

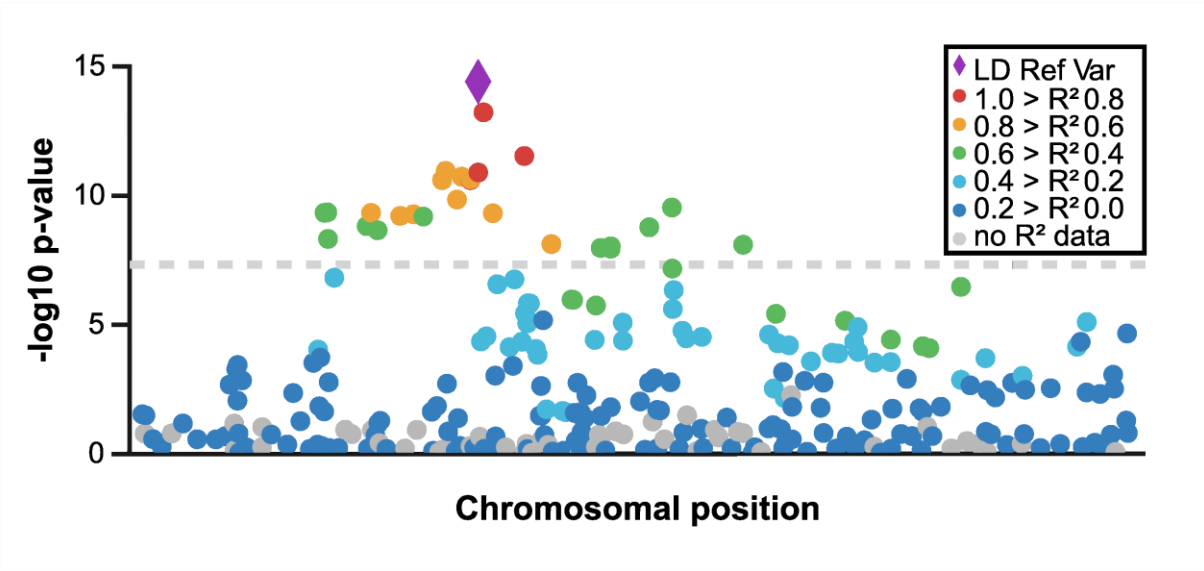

Figure 2. Exemplary plot of a locus detected by a genome-wide association study (GWAS).

Displayed is an exemplary locus identified in a GWAS with genome-wide significance, defined by a p-value < 5 x 10^{-08} (indicated by the grey dotted line). On the x-axis the chromosomal position is indicated and on the y-axis the p-value of the association. The genetic variant with the smallest p-value is shown as a purple diamond and is used as the reference variant for linkage disequilibrium (LD) calculation. The plot represents a simplified and thus modified version of the association signal of the so called *LIPC* locus with AMD [20] and was created with LocusZoom [21].

However, the fact that the allele frequencies are estimated from linked variants points also to one of the major limitations of GWAS. While GWAS were designed to identify genetic regions associated with disease, they do not allow to draw any conclusions about causality of the associated region due to the limited resolution of genetic variants in a region of high LD. This is of particular importance as only a minority of genetic variants identified by GWAS are located in protein-coding regions and therefore are predicted to have a direct functional consequence on the respective protein [22]. In fact, approximately 88 % of GWAS-identified variants are located in intronic or intergenic regions of the genome [23], highlighting the necessity to perform follow-up studies to elucidate the biological mechanism underlying genetic associations. So far, however, functional follow-up studies are rarely performed as demonstrated in **Figure 3** [24] and therefore display an important next step in the post-GWAS era.

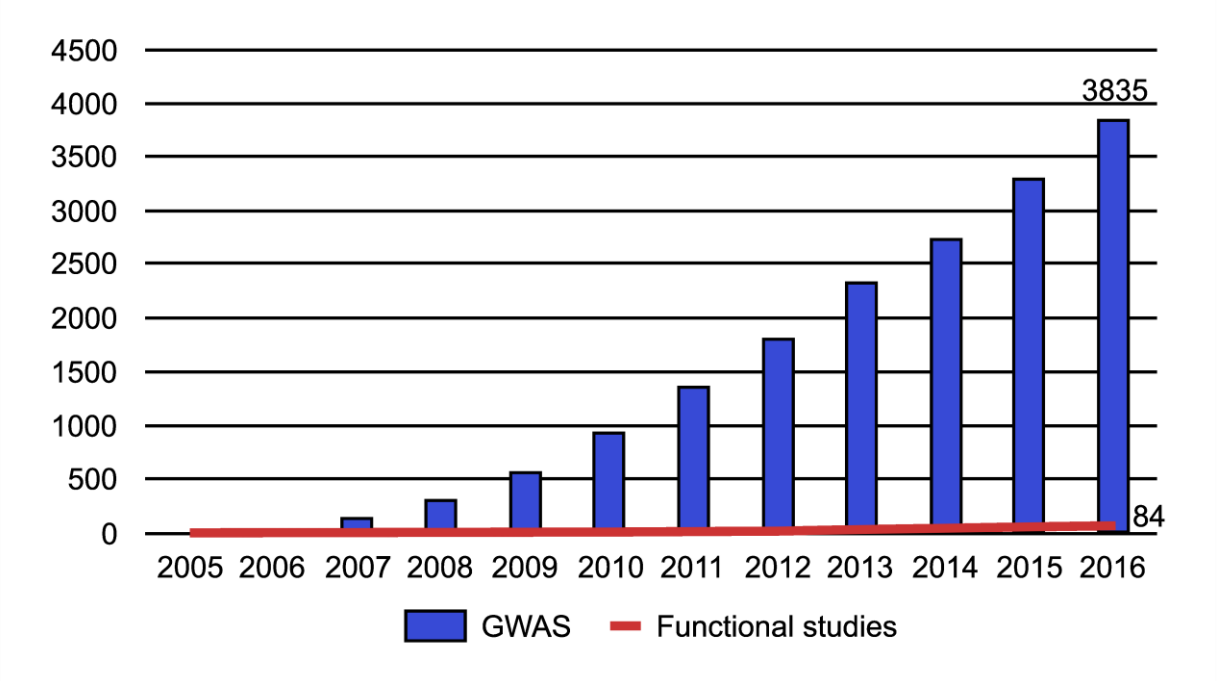

Figure 3. Cumulative GWAS and functional follow-up studies per year.

The number of GWAS was derived from the EBI GWAS catalog reported between 2005 till the end of 2016, which are shown in blue. The number of functional follow-up studies reported for the respective years was derived from article titles, or sometimes from the article abstract, from 23 biomedical research journals, as well as by a keyword

search (keywords “causal variant” and “functional variant”) using PubMed. Detailed information is given in [24] (Figure modified from Gallagher and Chen-Plotkin, 2018 [24]).

1.3 The genetics of AMD

The latest GWAS for AMD was performed in 2016 by the International AMD Genomics Consortium (IAMDGC) and identified 52 independent genetic signals distributed over 34 loci associated with AMD at the level of genome-wide significance [20], which is defined by a p-value threshold of 5×10^{-08}. However, even four years later our knowledge about the functional impact underlying the genetic association of those loci for the AMD pathology is limited. An analysis of the studies, which have cited the two latest AMD GWAS performed in 2013 [25] and 2016 [20], revealed that one third of follow-up articles are review articles and another third are follow-up genetic association studies. Only 19 % of the analyzed articles referred to experimental studies exploring functional consequences of associated genetic variants. Remarkably, locus-specific analyses focused mainly on the *Complement Factor H* (*CFH)*, *Age-Related Maculopathy Susceptibility 2 (ARMS2) / High-Temperature Requirement A Serine Peptidase 1 (HTRA1)* and *Complement C3 (C3)* loci (**Figure 4**) [26]. While two of those loci harbor genes involved in the complement system, thought to play a crucial role in AMD pathology [27,28], the functional mechanism behind the association at the *ARMS2*/*HTRA1* locus is still highly controversial [29–32]. However, for the remaining 31 AMD-associated loci follow-up studies were rarely performed.

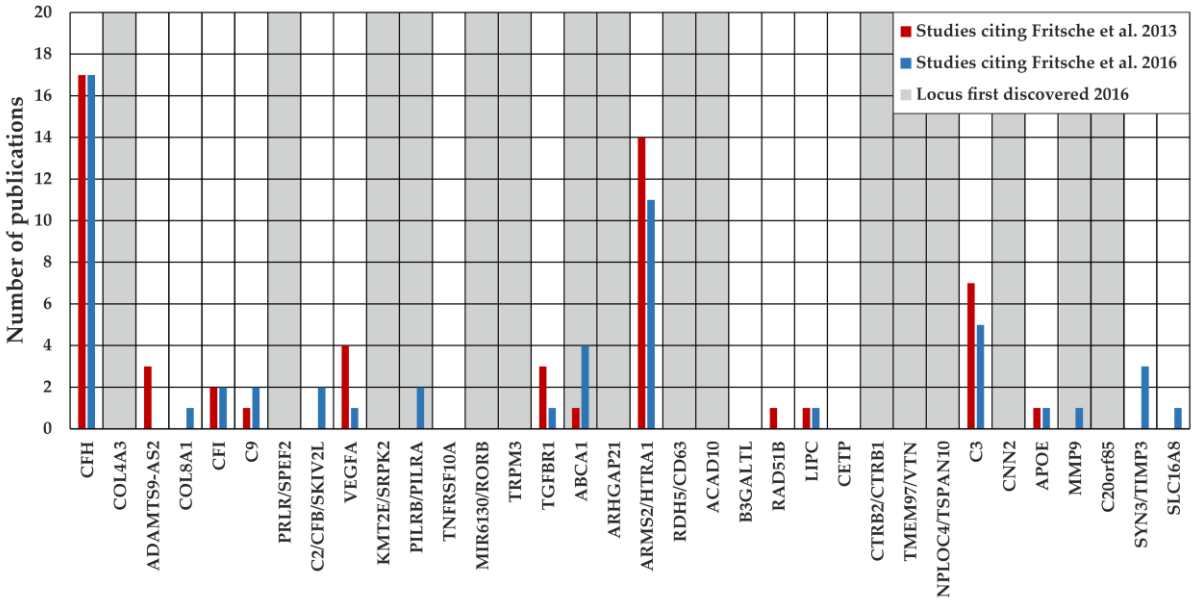

Figure 4. Previously investigated AMD-associated GWAS loci.

Shown are the number of studies, which cited the two latest AMD GWAS performed in 2013 [25] and 2016 [20] and conducted locus-specific analyses. Forty-three publications cited the AMD GWAS performed by Fritsche et al., 2013 (displayed in red) [25] and performed analyses for the AMD-associated loci. Eleven of these studies investigated

several loci and therefore, the overall number of studies referred to this GWAS increased to 55. Additional 38 publications cited the latest AMD GWAS performed in 2016 from Fritsche et al. (shown in blue) [20] and performed follow-up analyses for specific AMD-associated loci. Again, several studies investigated multiple loci resulting in 55 locus-specific analyses. Loci, which were associated with AMD at the level of genome-wide significance in the GWAS from Fritsche et al. (2016) [20] for the first time, are shaded in grey (Figure modified from Kiel et al., 2020 [26]).

It is noteworthy, that several hundred to thousand genetic variants are associated with AMD with nominal significance, only slightly failing the level of genome-wide significance [20]. It is expected that with a larger sample size, more genome-wide associated variants will become obvious. This is based on the fact, that the number of samples used to conduct a GWAS strongly correlates with the number of genetic variants detected [33]. Consequently, a large number of AMD-associated variants has just not yet been identified. Nevertheless, such additional variants may have potentially interesting underlying functional mechanisms, which could contribute to delineate the biological mechanisms involved in AMD etiology and pathology.

In particular, the biological mechanisms behind the association signals are required to understand the disease and, ideally, to develop new treatment options based on defined target molecules. Additionally, the question arises whether genetic markers could be applied to predict disease progression. For instance, to foresee a potential progression from GA to NV would help to start therapy at an early stage, which may slow down or stop the rapidly progressing disease subtype. Of special interest are therefore genetic variants associated with a defined subtype of AMD, as they harbor potential to pinpoint specific biological mechanisms involved in only one subtype of AMD. For this purpose, several GWAS have been conducted for distinct AMD subtypes, but so far they identified only a limited number of sub-phenotype associated genetic variants [34–36]. Therefore, it is even more important to investigate the biological function behind the known genetic associations in more detail, as this offers a promising possibility to discriminate and treat the different subtypes of AMD more precisely in the future.

Uncovering functional mechanisms underlying genetic associations is a challenging task as every single genetic association has to be investigated in detail and ideally with different methods to draw a comprehensive picture (**Figure 5**). Common methods include functional analyses by wet lab experiments [37], gene expression analyses for example by expression quantitative trait locus (eQTL) studies [38], alterations in transcription factor (TF) binding [39], epigenetic modifications [40] or analysis of pleiotropic effects [41]. However, the multitude of genetic associations described for one complex disease makes the functional interpretation even more difficult.

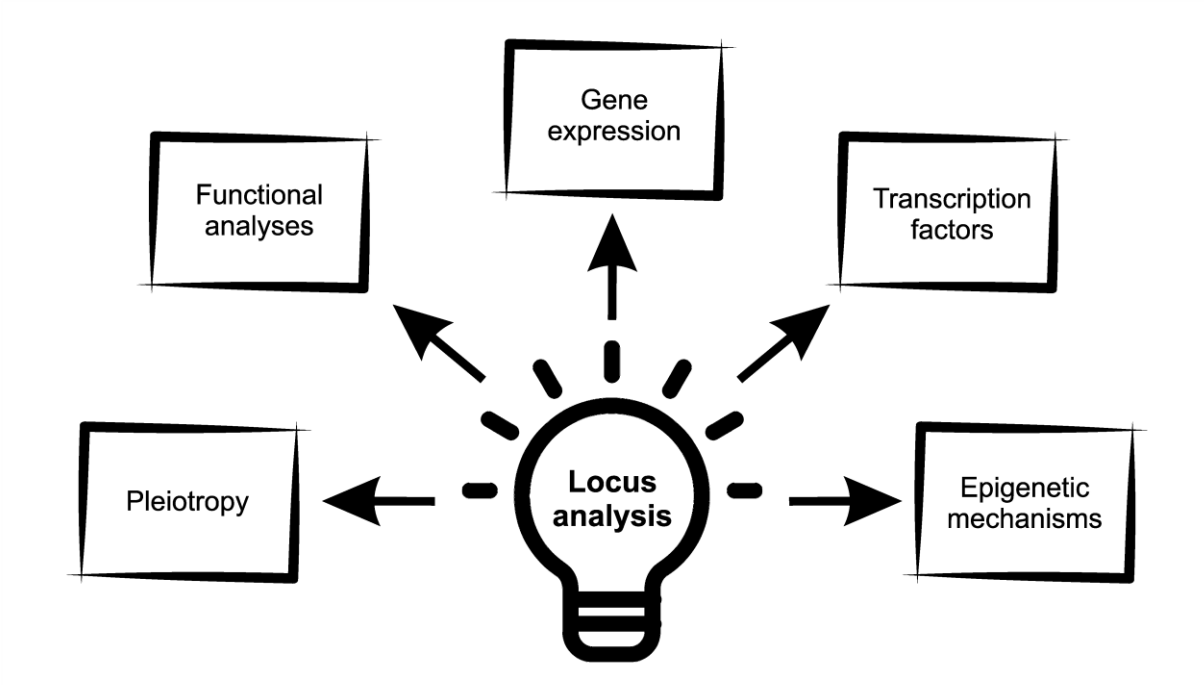

Figure 5. Schematic overview of different ways to characterize genetic associations.
The mind map shows different exemplary methods to functionally address genetic associations.

1.4 Pleiotropy

One option to investigate functionality underlying genetic association signals is the analysis of genetic pleiotropy. Pleiotropy describes the principle, that one gene can influence several seemingly unrelated phenotypes. However, there are several types of pleiotropy, including horizontal and vertical pleiotropy (**Figure 6**) [42,43]. In horizontal pleiotropy, a genetic signal influences an intermediate process, which contributes to two different phenotypes while vertical pleiotropy describes a genetic signal that influences one phenotype and this phenotype in turn has an impact on the second phenotype. This would mean that the second phenotype is actually not directly caused by the genetic signal, but occurs as a secondary effect due to the change in the first phenotype. There are some specific methods to investigate distinct types of pleiotropy, like Mendelian Randomization to study vertical pleiotropy and thereby identify causal relationships [44]. Nevertheless, distinguishing between different types of pleiotropy in general is difficult.

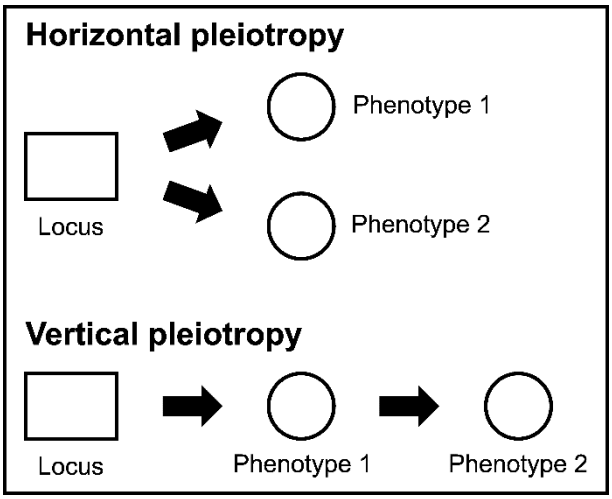

Figure 6. Types of pleiotropy.
Schematically shown are two different types of pleiotropy. In horizontal pleiotropy, one genetic signal contributes to two different phenotypes. In contrast, in the vertical pleiotropy, one genetic signal influences one phenotype and this phenotype in turn influences a second phenotype (Figure based on Jordan et al., 2019 [45]).

One method to study pleiotropy, although without distinguishing different types of pleiotropy, is to use genetic correlations. In fact, it has been demonstrated that several complex diseases genetically correlate [46,47] and also for AMD, genetic correlations with several complex traits have been reported [41]. In case two distinct diseases share a genetic association, the underlying functional mechanism might contribute to both diseases. Furthermore, knowledge about the genetics of different complex diseases may be at different stages of progress. A locus may be well studied for one complex disease while it has received little attention for another disease so far. If the identical genetic signal is underlying the two associations, knowledge about the underlying functional mechanism gained for one phenotype might be transferable to the second phenotype. This way, pleiotropic analyses can be applied to study functionality of association signals. However, analyzing genetic correlations does not allow to make any implications about causality and therefore follow-up approaches like co-localization analyses are required. By co-localization analyses two different genetic association signals are compared to determine whether they correspond to the same genetic signal (as indicated exemplarily in **Figure 2**) or just occur due to coincidence. A combination of different methods therefore represents a powerful tool to investigate pleiotropic effects of genetic association signals and to elucidate the functional mechanism behind an association signal.

1.5 microRNAs (miRNA)

Beside genetic associations detectable through GWAS, several other factors might contribute to the risk and pathology of a complex disease like AMD. One of those factors are epigenetic mechanisms. Epigenetic modifications influence the activation of genes without being attributed to changes of the DNA sequence. Indeed, epigenetic modification arises from external or environmental factors [48,49]. For this reason, epigenetics has recently received a

great amount of attention in the investigation of complex diseases [49–52]. Epigenetic mechanisms include three major systems, including DNA methylation, histone modification and RNA-induced silencing [53]. Especially, induced gene silencing mediated through RNAs, such as microRNAs (miRNAs), has gained attention in recent years, as it offers great potential for clinical applications [54,55]. Also in AMD research, the importance of miRNAs is increasingly being investigated [56–59].

MiRNAs are small post-transcriptional regulators, with an approximate length of 22 bp for the matured form. They play a crucial role in many biological processes and require a complex maturation before they reach an active form (**Figure 7**). First, the miRNA gene is transcribed by the RNA polymerase II, which results in the primary miRNA transcript (pri-miRNA). Subsequently, the RNase III enzyme Drosha processes the pri-miRNA to the precursor miRNA (pre-miRNA), which exhibits a stem-loop structure. At this step, the pre-miRNA is exported from the nucleus *via* the export receptor Exportin 5 to the cytoplasm. Next, the RNase III enzyme Dicer splits off the loop structure of the pre-miRNA. This results in a double-stranded intermediate, which separates soon afterwards. Cellular nucleases degrade one of the single strands and the other strand gets incorporated into the RNA-induced silencing complex (RISC), where it generates the mature miRNA [60,61]. The incorporated mature miRNA in RISC mediates recognition and binding of specific mRNAs by complementary base pairing, mainly in the 3'-untranslated regions (3'-UTR) of the target transcripts. Nucleotides 2 – 7 of the mature miRNA, the so called seed region, are essential for this complementary binding. Finally, binding of the complex to target transcripts leads to recruitment of Argonaute proteins, which can cleave mRNA transcripts or repress the mRNA translation [60,62]. Noteworthy, regulation through a miRNA is not restricted to one target gene, but instead miRNAs are able to regulate the expression of several genes simultaneously [63]. This process is strictly conserved and its importance is highlighted by the fact, that genetic variants in miRNA genes and especially the seed region are extremely rare [64,65].

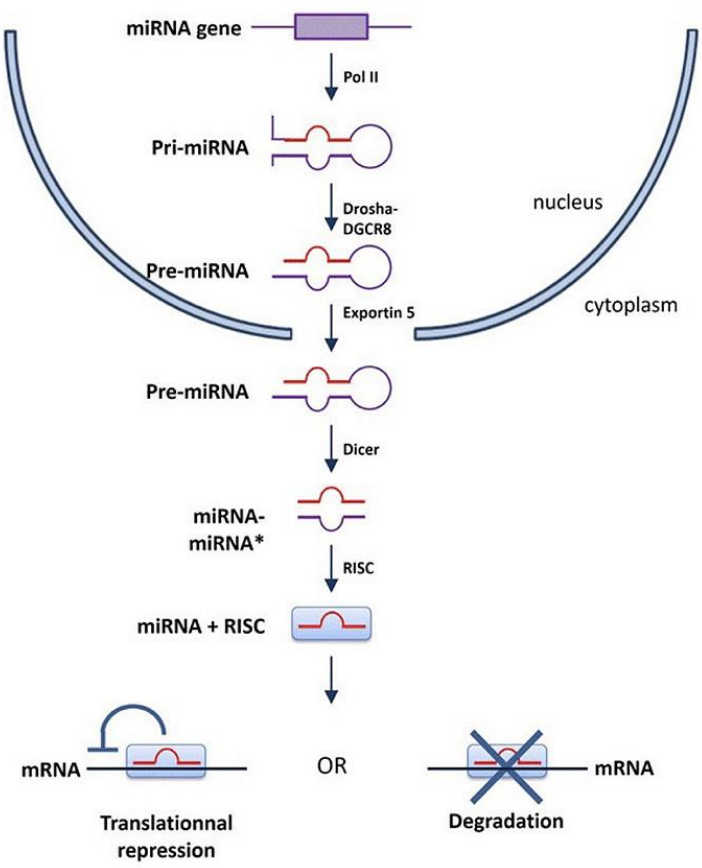

Figure 7. Biogenesis of microRNAs (miRNA).
Schematic overview on the miRNA biogenesis. After transcription of the miRNA by the RNA polymerase II (Pol II), the resulting primary miRNA transcripts (pri-miRNA) gets processed by a complex including Drosha and DGCR8. After processing, the precursor miRNA (pre-miRNA) gets exported from the nucleus of the cell in the cytoplasm by Exportin 5. In the cytoplasm, the pre-miRNA gets processed again, this time by Dicer. One of the miRNA strands (miRNA*) gets degraded, while the second strand gets loaded into the RNA-induced silencing complex (RISC), where the matured miRNA gets generated. The complex gets guided by the miRNA to target mRNAs, where binding of the complex leads to degradation of the mRNA or translational repression (Figure adopted from Jafri et al., 2019 [66]).

It is estimated that over 60 % of protein-coding genes are regulated by miRNAs [67]. Thereby, miRNAs are involved in many crucial biological mechanisms, including amongst others apoptosis [68–70], inflammation [71,72], proliferation [70,73], autophagy [72,74], and differentiation [75]. Hence, dysregulation of miRNA expression might contribute to a variety of diseases [56,57,68,70,76–78]. However, they also display potential new therapeutic targets [79] or might serve as biomarkers, as miRNAs can occur extracellularly in, for example, blood or plasma as circulating miRNAs (cmiRNAs) and are therefore easily accessible [80–82].

1.6 Aim of this study

While the latest GWAS identified 52 independent genetic variants associated with AMD at genome-wide significance, there are thousands of additional variants that display nominal significant associations with AMD [20]. These variants might also have a potential impact on AMD etiology or pathology. Furthermore, recent approaches also linked gene expression [38,83,84] or epigenetic modifiers like miRNAs to AMD, although with often contradictory results for the latter studies [56,76,85–89]. It is of note, that for almost all associations it still remains unclear which mechanism of action underlies the association [26].

The present work aimed to investigate how insight into molecular function can be combined with the mere genetic association of genetic variation with disease, in particular AMD. For this purpose, an established mouse model with laser-induced NV was used to investigate cmiRNA expression alterations after NV induction. Expression changes of the identified cmiRNAs were further analyzed in the ocular tissues directly affected by laser treatment, including retina and RPE/choroid. Furthermore, AMD-associated genes were bioinformatically screened for pleiotropic effects to identify potentially shared mechanisms with other complex diseases to further elucidate AMD disease pathology. The locus of an exemplary pleiotropic gene was further characterized to delineate its association with AMD and its pleiotropic nature. Furthermore, the selected locus harbors a miRNA gene with a seed polymorphism, which has a potential impact on the gene regulatory function of this miRNA. The allele-specific gene regulation of this miRNA was finally investigated to identify allele-specific target genes, which potentially might contribute to AMD etiology or pathology.

2 Material

2.1 Escherichia coli (E. coli) Strains

Table 1. Escherichia coli (E. coli) strains used.

Strain	Source
E. coli strain DH5α	Thermo Fisher Scientific, Waltham, Massachusetts, USA
E. coli strain JM109	Promega Corporation, Madison, Wisconsin, USA

2.2 Eukaryotic Cell Lines

Table 2. Names and tissue of origin of cell lines used.

Cell Line	Organism	Tissue of Origin	Source
HEK293T	*Homo sapiens*	Embryonic kidney	ATCC, Manassas, Virginia, USA
HUVEC	*Homo sapiens*	Umbilical Vein Endothelial Cells	Life Technologies, Carlsbad, California, USA

2.3 Cell Culture Media and Supplements

Table 3. List of cell culture media and supplements/additives used.

Component	Source
DMEM High Glucose Medium (4.5 g/L)	Thermo Fisher Scientific, Waltham, Massachusetts, USA
Dulbecco's phosphate buffered saline (DPBS)	Thermo Fisher Scientific, Waltham, Massachusetts, USA
EBM™ Plus Basal Medium	Lonza, Basel, Switzerland
EGM™ Plus SingleQuots	Lonza, Basel, Switzerland
Fetal Bovine Serum (FBS)	Thermo Fisher Scientific, Waltham, Massachusetts, USA
OptiMEM™ Medium	Thermo Fisher Scientific, Waltham, Massachusetts, USA
Penicillin (10,000 units/mL)/Streptomycin (10 µg/mL)	Thermo Fisher Scientific, Waltham, Massachusetts, USA
Trypsin-EDTA (0.5 %)	Thermo Fisher Scientific, Waltham, Massachusetts, USA

2.4 Oligonucleotides Used for miRNA Mimic Transfection

Table 4. Name, sequence and specification of oligonucleotides used as miRNA mimics for eukaryotic cell transfection.

Name	5'-3' Sequence	Specification
cel-miR-39	UCA CCG GGU GUA AAU CAG CUU G	miRCURY LNA miRNA mimic
hsa-miR-4513-A	AGA CUG AUG GCU GGA GGC CCA U	miRCURY LNA miRNA mimic
hsa-miR-4513-G	AGA CUG ACG GCU GGA GGC CCA U	miRCURY LNA miRNA mimic

All miRCURY LNA miRNA mimics were purchased from Qiagen, Hilden, Germany.

2.5 Oligonucleotides Used for miRNA Detection *via* Quantitative Reverse Transcription PCR (qRT-PCR)

Table 5. Name, sequence and application of oligonucleotides used for miRNA detection *via* quantitative reverse transcription PCR (qRT-PCR).

Name	5'-3' Sequence	Application
cel-miR-39	TCA CCG GGT GTA AAT CAG CTT GAA AA	miRNA detection
hsa-miR-4513-A	TGA TGG CTG GAG GCC CAT AAA A	miRNA detection
hsa-miR-4513-G	TGA CGG CTG GAG GCC CAT AAA A	miRNA detection
mmu-let-7i-3p	CTG CGC AAG CTA CTG CCT	miRNA detection
mmu-let-7i-3p_modified	CGC AAG CTA CTG CCT TGC TAA AA	Primer with poly-A tail for miRNA detection in long-term stored RNA from blood samples or tissue
mmu-miR-148b-5p	GAA GTT CTG TTA TAC ACT CAG GCT	miRNA detection
mmu-miR-155-5p	TTA ATG CTA ATT GTG ATA GGG GT	miRNA detection
mmu-miR-155-5p_modified	TTA ATG CTA ATT GTG ATA GGG GTA AAA	Primer with poly-A tail for miRNA detection in long-term stored RNA from blood samples or tissue
mmu-miR-18a-3p	ACT GCC CTA AGT GCT CCT TCT	miRNA detection
mmu-miR-18a-3p_modified	GCC CTA AGT GCT CCT TCT GGA AAA	Primer with poly-A tail for miRNA detection in long-term stored RNA from blood samples or tissue
mmu-miR-20a-5p	TAA AGT GCT TAT AGT GCA GGT AG	miRNA detection
mmu-miR-298-5p	GGC AGA GGA GGG CTG TTC	miRNA detection

mmu-miR-449a-5p	TGG CAG TGT ATT GTT AGC TGG T	miRNA detection
mmu-miR-449a-5p_modified	TGG CAG TGT ATT GTT AGC TGG TAA AAA	Primer with poly-A tail for miRNA detection in long-term stored RNA from blood samples or tissue
mmu-miR-486a-5p	TCC TGT ACT GAG CTG CCC	miRNA detection
mmu-miR-486a-5p_modified	TCC TGT ACT GAG CTG CCC CGA GAA AA	Primer with poly-A tail for miRNA detection in long-term stored RNA from blood samples or tissue
mmu-miR-92a-3p	TAT TGC ACT TGT CCC GGC	miRNA detection
mmu-miR-92a-3p_modified	GCA CTT GTC CCG GCC TGA AAA	Primer with poly-A tail for miRNA detection in long-term stored RNA from blood samples or tissue
Universal Primer	AAC GAG ACG ACG ACA GAC TTT	miRNA detection
Universal RT oligonucleotide primer	AAC GAG ACG ACG ACA GAC TTT TTT TTT TTT TTT V	Primer annealed to a polyA tail added to mature miRNAs for detection by qRT-PCR

All oligonucleotides were purchased from metabion international AG, Planegg, Germany or Sigma-Aldrich, St. Louis, Missouri, USA.

2.6 Oligonucleotides and Corresponding Probes Used for qRT-PCR

Table 6. Name, sequence and corresponding probe number for oligonucleotides used for qRT-PCR.

Name	5'-3' Sequence	Gene	Roche Universal ProbeLibrary
APOLD1_mir4513_F1_16	TCC AGA AAC AGC CTC AGA TTT T	*APOLD1*	16
APOLD1_mir4513_R_16	AGC AGC AGT CCC TGG AAG		
CANX_mir4513_F_66	ATG GGG CCT GAA GAA AGC	*CANX*	66
CANX_mir4513_R_66	ATC ATC TGC CCC ACA ACG		
CD2BP2_mir4513_F_16	CAT CTT GGC CTC AGA GGA TG	*CD2BP2*	16
CD2BP2_mir4513_R_16	CCT GCA GGT TAA AGG GTG TG		
CDKN2A_mir4513_F1_66	CTA CTG AGG AGC CAG CGT CTA	*CDKN2A*	66
CDKN2A_mir4513_R1_66	CTG CCC ATC ATC ATG ACC T		
DDX46_mir4513_F_15	CCC AAC CAT TAT GAG GAT TAT GT	*DDX46*	15

DDX46_mir4513_R_15	TGA TCC TCT GTG ATA AAA GTA TAA GCA		
EIF4EBP2_mir4513_F_22	GCG CAG CTA CCT CAT GAC TAT	*EIF4EBP2*	22
EIF4EBP2_mir4513_R_22	TCT GTC ATA AAT GAT TCG AGT TCC T		
FSTL1_mir4513_F_2	GCC ATC AAT ATT ACA ACG TAT CCA	*FSTL1*	2
FSTL1_mir4513_R_2	TCA ATG AGA GCA TCA ACA CAG A		
GTF3A_mir4513_F_76	CAG GAG AAA AGC CGT TTG TT	*GTF3A*	76
GTF3A_mir4513_R_76	TTC TTC AAG TTT GAT TTT GTG TTG A		
hHPRT-qRT-F	TGA CCT TGA TTT ATT TTG CAT ACC	*HPRT1*	73
hHPRT-qRT-R	CGA GCA AGA CGT TCA GTC CT		
ITPRIPL2_mir4513_F_82	ATC AGT TAC TCC CTG GTC GTG	*ITPRIPL2*	82
ITPRIPL2_mir4513_R_82	GGC TGT CTC CCT TGC TCT TT		
KLF6_mir4513_F_25	GCA CGA GAC CGG CTA CTT C	*KLF6*	25
KLF6_mir4513_R_25	CCA GCT CTA GGC AGG TCT GTT		
MAP4K4_mir4513_F_29	TTG TGG CAT TAC AGC CAT TG	*MAP4K4*	29
MAP4K4_mir4513_R_29	TTG GAT GCA TGT CAC AGA GAG		
MCFD2_mir4513_F_69	TGG CTT AGA ACT CTC CAC AGC	*MCFD2*	69
MCFD2_mir4513_R_69	CTC ATT AGT GGT GCC TGT TCA C		
MGAT4A_mir4513_F_33	TCT TCT GAG GAA TGG ATG ATT CTA	*MGAT4A*	33
MGAT4A_mir4513_R_33	TAA GAT CCG GCG CTT GAA		
PTGS1_mir4513_F_4	CAC CCA TGG GAA CCA AAG	*PTGS1*	4
PTGS1_mir4513_R_4	TGG GGG TCA GGT ATG AAC TT		
PTPRD_mir4513_F_88	GGC GCC TTA ACT TTC AAA CA	*PTPRD*	88
PTPRD_mir4513_R_88	ATG TGG TCT GCA AGT TCC AA		
RGMB_mir4513_F_35	GGA GCG AAA GGG TTA AGA ATG	*RGMB*	35
RGMB_mir4513_R_35	CGT CCA TGC AGG TCT CGT		
SEC63_mir4513_F_41	TTG GTT AAG TTG ACA AGG CAA A	*SEC63*	41
SEC63_mir4513_R_41	TGT TCC TCT GCA GCA CAG AT		
FAM208A_mir4513_F_18	TGA AAA TTG CCA TCT GTA TGA AG		18

FAM208A_mir4513_R_18	GTC AGC AAT GCC GGA GTT A	*TASOR/ FAM208A*	
TBC1D5_mir4513_F_21	TCC CTG GCA GGA TTA AAA CA	*TBC1D5*	21
TBC1D5_mir4513_R_21	TTC GTT CTC TTC GGC CTC TA		
TCF12_mir4513_F_38	AGT GGG AAA ACT AGA CCA ACT ACA C	*TCF12*	38
TCF12_mir4513_R_38	TGT TGT ACC TCC TCT TTC ATC AAT AC		
TPM3_mir4513_F2_53	AGA CTT GGA ACG CAC AGA GG	*TPM3*	53
TPM3_mir4513_R2_53	CCT CCT CCA GCT CAG AAC AC		
TRPC4AP_mir4513_F_72	TTC TGC AGC TGA AAT CAA TCA	*TRPC4AP*	72
TRPC4AP_mir4513_R_72	AGT TTG CAA AGC CGC TCA		
ZC3HAV1_mir4513_F_81	AGG ACA TCT GCA ACA GCA AG	*ZC3HAV1*	81
ZC3HAV1_mir4513_R_81	TGC CAT GTT TCT ACG ATG TGA		

All oligonucleotides were purchased from metabion international AG, Planegg, Germany or Sigma-Aldrich, St. Louis, Missouri, USA and all probes from Sigma-Aldrich, St. Louis, Missouri, USA.

2.7 Oligonucleotides for PCR and Sequencing Reactions

Table 7. Name, sequence and purpose of oligonucleotides used for PCR and sequencing reactions.

Name	5'-3' Sequence	Purpose
CD2BP2_Nhe1_F	TTT AGC TAG CCT GCT GGG GGC CCA GTT T	Cloning of the 3'-UTR of *CD2BP2* in a luciferase reporter vector
CD2BP2_Xho1_R	AGC CCT CGA GGG TTT TCA CCA GGC TGA AGT	
CD2BP2_seq_F1	AAG TGC AAA CTC AGT GGC CAA GT	
CD2BP2_seq_F2	TTG GGA TCC CAG GTC AGA AAG G	
CD2BP2_seq_R1	CCT TTG ATT CCT GTG ATC TCC AG	
CD2BP2_seq_R2	CTA GAA GGG GCC TCA CAA GAG	
p14ARF_1_Sac1_F	TTT AGA GCT CGC CAT CGC GAT GTC GCA C	Cloning of the 3'-UTR of *CDKN2A* (p14 transcript, ENST00000579755) in a luciferase reporter vector
p14ARF_1_Xho1_R	AGC CCT CGA GGC TTT GGT TCT GCC ATT TGC	

p16INK4a_1_Sac1_F	TTT AGA GCT CAG AAC CAG AGA GGC TCT GAG	Cloning of the 3'-UTR of *CDKN2A* (p16 transcript 1, ENST00000304494) in a luciferase reporter vector
p14ARF_1_Xho1_R	AGC CCT CGA GGC TTT GGT TCT GCC ATT TGC	
p16INK4a_1_Sac1_F	TTT AGA GCT CAG AAC CAG AGA GGC TCT GAG	Cloning of the 3'-UTR of *CDKN2A* (p16 transcript 2, ENST00000578845) in a luciferase reporter vector
p14ARF_2_Xho1_R	AGC CCT CGA GTA CGG TAG TGG GGG AAG GCA	
p16INK4a_3_Sac1_F	TTT AGA GCT CTC ATC AGT CAC CGA AGG TCC	Cloning of the 3'-UTR of *CDKN2A* (p16 transcript 3, ENST00000579122) in a luciferase reporter vector
p14ARF_2_Xho1_R	AGC CCT CGA GTA CGG TAG TGG GGG AAG GCA	
DDX46_Nhe1_F	TTT AGC TAG CGT GGC AGT TGC TGT CTG CA	Cloning of the 3'-UTR of *DDX46* in a luciferase reporter vector
DDX46_Xho1_R	ATA CCT CGA GAA CAT CAA GGT GGG GAC AC	
ITPRIPL2_Xho1_F	ATA CCT CGA GCC ACC TGA CCA AAT GCT CCT	Cloning of the 3'-UTR of *ITPRIPL2* in a luciferase reporter vector
ITPRIPL2_Xba1_R	TTT ATC TAG AGG TCC CCA AAT GAC CCA CAT	
ITPRIPL2_seq_F1	GGG GCT AAT GTT TAG AGG AAC ATA	
ITPRIPL2_seq_F2	GGT TTT TAG CAA ACT CCT TCA CAA	
ITPRIPL2_seq_F3	GTA CTT CCT CAG ACT CTT AAA GCT	
ITPRIPL2_seq_F4	AGT GGG GGA CAT CAA GGG TT	
ITPRIPL2_seq_F5	TTG CAA AAT GAA ACT GAA GCT GAA	
ITPRIPL2_seq_F6	GGC GTG ATA TTT GAA GTC ATC TTT	
ITPRIPL2_seq_F7	CAA CTA GCT GGG ACC ACA GG	
ITPRIPL2_seq_F8	TAT CAT TTT CTG ACT CAG CAG CTC	
ITPRIPL2_seq_F9	AGG TGC CTT GAT TCAG TTG CG	
ITPRIPL2_seq_R1	GTC AAA CAC CTG TGA TTG CAC C	
ITPRIPL2_seq_R2	TTA GAG ACC CAG CAC AAA CCA C	
ITPRIPL2_seq_R3	CAA AAG AGC TCA GAA CTT CAA CAA	
ITPRIPL2_seq_R4	ACG CCC AGC CTT AAA GCT TTA TA	
ITPRIPL2_seq_R5	TCC CTC TCT TGC TTC ACT TTC AT	
ITPRIPL2_seq_R6	CCT GGG AAC TGT GAG TTA AGT GT	

ITPRIPL2_seq_R7	CAT AGG GAG ACC CTG ACT CTA C	
ITPRIPL2_seq_R8	TTC CTT CAC AGT GTT TGC TAG GA	
ITPRIPL2_seq_R9	ACA ATT GTA GCA GCT GAA CCA TAT	
KLF6_Nhe1_F	TTT AGC TAG CGG AGC AGA GAG GTG GAT CCT	
KLF6_Xho1_R	ATA CCT CGA GCT GCC CTC CTT GAC TGA GAG	
KLF6_seq_F1	GAA AAT CTT GGA GGG TGG GCG T	
KLF6_seq_F2	GAG CCT CAA TCA AGC AGA AAC TTT	Cloning of the 3'-UTR of *KLF6* in a luciferase reporter vector
KLF6_seq_F3	GGT GGA TAA AAC CAC TAA CGC TTA	
KLF6_seq_F4	GCT AAC CAC AGG GAT TCT TTT GTA	
KLF6_seq_R1	AAA AGG GGG AGA GAG GCT CTC C	
KLF6_seq_R2	CCG GAA CAG ATT CAA GCA AGA AAG	
KLF6_seq_R3	AAT TGT ATA TTG CCA GGC CCG G	
TPM3_Nhe1_F	TTT AGC TAG CCA GTC CCA CCC TGC TGC T	
TPM3_Xho1_R	ATA CCT CGA GCT CTT TCT CCC AAT CGG CCC	Cloning of the 3'-UTR of *TPM3* in a luciferase reporter vector
TPM3_seq_F	GGT AAG ACC TCT GAG ACC AAA ATT	
TPM3_seq_R1	TTC CAA AAG TGA GAA AGG GAT TCG	
TPM3_seq_R2	GCA GGA AAG CAA TTA AGT GGT CAC	
M13F	CGC CAG GGT TTT CCC AGT CAC GAC	Sequencing primer pGEM vector
M13R	AGC GGA TAA CAA TTT CAC ACA GGA	
pmirGLO_seq_F	GCA AGA TCC GCG AGA TTC TCA T	Sequencing primer pmirGLO vector
pmirGLO_seq_R	CAA CTC AGC TTC CTT TCG GGC T	

3'-UTR = 3'-untranslated region.

All oligonucleotides were purchased from metabion international AG, Planegg, Germany or Sigma-Aldrich, St. Louis, Missouri, USA.

2.8 Plasmids and Expression Constructs

Table 8. List of expression constructs, application and source.

Vector Name	Application	Source

pGEM®-T	Subcloning of vector inserts	Promega Corporation, Madison, Wisconsin, USA
pmirGLO Dual-Luciferase miRNA Target Expression Vector	Luciferase Reporter Assay	Promega Corporation, Madison, Wisconsin, USA
pmirGLO_CD2BP2	Luciferase Reporter Assay	Generated during this project
pmirGLO_CDKN2A_p14	Luciferase Reporter Assay	Generated during this project
pmirGLO_CDKN2A_p16_1	Luciferase Reporter Assay	Generated during this project
pmirGLO_CDKN2A_p16_2	Luciferase Reporter Assay	Generated during this project
pmirGLO_CDKN2A_p16_3	Luciferase Reporter Assay	Generated during this project
pmirGLO_DDX46	Luciferase Reporter Assay	Generated during this project
pmirGLO_ITPRIPL2	Luciferase Reporter Assay	Generated during this project
pmirGLO_KLF6	Luciferase Reporter Assay	Generated during this project
pmirGLO_TPM3	Luciferase Reporter Assay	Generated during this project

2.9 Primary Antibodies

Table 9. Specifications of primary antibodies used for Western Blot.

Antibody	Type	Species	Dilution	Source
ß-Actin (#A5441)	mAB	mouse	1:10,000	Sigma-Aldrich, St. Louis, Missouri, USA
CD2BP2 (#PA5-59603)	pAB	rabbit	1:1,250	Thermo Fisher Scientific, Waltham, Massachusetts, USA
DDX46 (#PA5-57713)	pAB	rabbit	1:1,000	Life Technologies, Carlsbad, California, USA
HSP 90α/β (#sc-13119)	mAB	mouse	1:5,000	Santa Cruz, Dallas, Texas, USA
ITPRIPL2 (#HPA042011)	pAB	rabbit	1:100 – 1:1,000	Sigma-Aldrich, St. Louis, Missouri, USA
KLF6 (#PA5-79560)	pAB	rabbit	1:1,000	Life Technologies, Carlsbad, California, USA
P16 INK4A (#D7C1M)	mAB	rabbit	1:1,000	Cell Signaling Technologies, Danvers, Massachusetts, USA
TPM3 (#720306)	pAB	rabbit	1:1,000	Life Technologies, Carlsbad, California, USA

2.10 Secondary Antibodies

Table 10. Specifications of secondary antibodies used for Western Blot.

Antibody	Dilution	Source
Goat Anti-Mouse, lgG, Peroxidase Conjugated	1:10,000	Merck Chemicals GmbH, Schwalbach, Germany
Goat Anti-Rabbit lgG, Peroxidase Conjugated	1:10,000	Merck Chemicals GmbH, Schwalbach, Germany

2.11 Enzymes

Table 11. List of enzymes used.

Enzyme	Source
Antarctic Phosphatase	New England BioLabs, Ipswich, Massachusetts, USA
DNase	Qiagen, Hilden, Germany
GoTaq® DNA Polymerase	Promega Corporation, Madison, Wisconsin, USA
GoTaq® Long PCR DNA Polymerase	Promega Corporation, Madison, Wisconsin, USA
NheI-HF®	New England BioLabs, Ipswich, Massachusetts, USA
Phusion™ High-Fidelity DNA Polymerase	New England BioLabs, Ipswich, Massachusetts, USA
RevertAid™ Reverse Transcriptase	Thermo Fisher Scientific, Waltham, Massachusetts, USA
SacI-HF®	New England BioLabs, Ipswich, Massachusetts, USA
SuperScript™ III Reverse Transcriptase	Thermo Fisher Scientific, Waltham, Massachusetts, USA
T4 DNA Ligase	New England BioLabs, Ipswich, Massachusetts, USA
XbaI	New England BioLabs, Ipswich, Massachusetts, USA
XhoI	New England BioLabs, Ipswich, Massachusetts, USA

2.12 Kit Systems

Table 12. List of kit systems used.

Kit	Source
Agilent High Sensitivity DNA Kit	Agilent Technologies, Santa Clara, California, USA
BigDye Terminator v3.1 Cycle Sequencing Kit	Thermo Fisher Scientific, Waltham, Massachusetts, USA
Clarity Max™ Western ECL Substrate	Bio-Rad Laboratories, Hercules, California, USA
Clarity™ Western ECL Substrate	Bio-Rad Laboratories, Hercules, California, USA
Dual-Glo® Luciferase Assay System	Promega Corporation, Madison, Wisconsin, USA
HiPerFect Transfection Reagent	Qiagen, Hilden, Germany
Lipofectamine 2000 Transfection Reagent	Thermo Fisher Scientific, Waltham, Massachusetts, USA
mirVana™ miRNA Isolation Kit, with Phenol	Thermo Fisher Scientific, Waltham, Massachusetts, USA
NEXTFLEX® Rapid Directional mRNA-Seq Kit, including NEXTFLEX® Poly(A) Beads	PerkinElmer, Waltham, Massachusetts, USA
NucleoBond® XtraMidi	MACHEREY-NAGEL GmbH & Co. KG, Düren, Germany
NucleoSpin® Gel and PCR Clean-up	MACHEREY-NAGEL GmbH & Co. KG, Düren, Germany
NucleoSpin® Plasmid	MACHEREY-NAGEL GmbH & Co. KG, Düren, Germany
pGEM®-T Vector	Promega Corporation, Madison, Wisconsin, USA
Poly(A) Tailing Kit	Thermo Fisher Scientific, Waltham, Massachusetts, USA
PureLink™ RNA Mini Kit	Thermo Fisher Scientific, Waltham, Massachusetts, USA
Random Hexamer Primer	Thermo Fisher Scientific, Waltham, Massachusetts, USA
Takyon™ Low ROX Probe 2X MasterMix dTTP Blue	Eurogentec, Cologne, Germany
Takyon™ Low ROX SYBR 2X MasterMix blue dTTP	Eurogentec, Cologne, Germany

2.13 Chemicals and Ready-Made Solutions

Table 13. List of chemicals/reagents used.

Chemical/Reagent	Source

5-Bromo-4-chloro-3-indolyl β-D-galactopyranoside (X-Gal), C14H15BrClNO6	AppliChem GmbH, Darmstadt, Germany
10X Antarctic Phosphatase Reaction Buffer	New England BioLabs, Ipswich, Massachusetts, USA
10X CutSmart® Buffer	New England BioLabs, Ipswich, Massachusetts, USA
10X DNA Ligase reaction Buffer	New England BioLabs, Ipswich, Massachusetts, USA
2X Rapid Ligation Buffer	Promega Corporation, Madison, Wisconsin, USA
5X Green GoTaq® Reaction buffer	Promega Corporation, Madison, Wisconsin, USA
5X Phusion™ GC buffer	New England BioLabs, Ipswich, Massachusetts, USA
Agarose (Biozym LE)	Biozym Scientific GmbH, Hessisch Oldendorf, Germany
Ammoniumperoxodisulfat (APS), (NH4)2S2O8	VWR International Germany GmbH, Darmstadt, Germany
Ampicillin sodium salt, C16H18N3NaO4S	Carl Roth GmbH + Co. KG, Karlsruhe, Germany
ß-Mercaptoethanol, HSCH2CH2OH	Sigma-Aldrich, St. Louis, Missouri, USA
Bacto Agar	BD Bioscience, Heidelberg, Germany
Bacto Yeast Extract	BD Bioscience, Heidelberg, Germany
Boric acid, H3BO3	Merck Chemicals GmbH, Schwalbach, Germany
Bromphenolblue sodium salt, C19H9Br4O5SNa	Merck, Darmstadt, Germany
CASYton	Omni Life Science GmbH & Co., Bremen, Germany
Deoxyribonucleosidetriphosphate (dNTPs) (dATP, dGTP, dCTP, dTTP)	Genaxxon Bioscience, Ulm, Germany
Dimethylformamid, C3H7NO	Carl Roth GmbH + Co. KG, Karlsruhe, Germany
Dimethylsulfoxid (DMSO), C2H6OS	AppliChem GmbH, Darmstadt, Germany
Ethanol ≥99,8 p.a, C2H6O	Carl Roth GmbH + Co. KG, Karlsruhe, Germany
Ethidiumbromide, C21H20BrN3 in H2O	AppliChem GmbH, Darmstadt, Germany
Ethylendiamintetraacetat disodium dihydrate salt (EDTA), C10H14N2Na2O8•2H2O	Merck Chemicals GmbH, Schwalbach, Germany
GeneRuler™ DNA Ladder Mix	Thermo Fisher Scientific, Waltham, Massachusetts, USA
Glucose, C6H12O6	Merck Chemicals GmbH, Schwalbach, Germany

Glycerol 87%, C3H8O3	University of Regensburg, Chemical Supplies
Glycine, C2H5NO2	Merck Chemicals GmbH, Schwalbach, Germany
HiDi™ Formamide, CH3NO	Thermo Fisher Scientific, Waltham, Massachusetts, USA
Hydrochloric acid 1M, HCl	Merck Chemicals GmbH, Schwalbach, Germany
Incidin™ Plus	Ecolab Inc., Saint Paul, Minnesota, USA
Isopropaonol, C3H8O	Merck Chemicals GmbH, Schwalbach, Germany
Isopropyl β-D-1-thiogalactopyranoside (IPTG), C9H18O5S	AppliChem GmbH, Darmstadt, Germany
Kalium chloride, KCl	VWR International Germany GmbH, Darmstadt, Germany
Magnesiumchloride hexahydrate, MgCl2•6H2O	Merck Chemicals GmbH, Schwalbach, Germany
Magnesiumsulfate heptahydrate, MgSO4•7H2O	Merck Chemicals GmbH, Schwalbach, Germany
Methanol, CH4O	Merck Chemicals GmbH, Schwalbach, Germany
Nuclease-free Water, H2O	Qiagen, Hilden, Germany
PageRuler™ Prestained Protein Ladder	Thermo Fisher Scientific, Waltham, Massachusetts, USA
Pepton	Carl Roth GmbH + Co. KG, Karlsruhe, Germany
RDD buffer	Qiagen, Hilden, Germany
Rotiphorese Gel 40% Acrylamide/ Bisacrylamide	Carl Roth GmbH + Co. KG, Karlsruhe, Germany
Skimmed Milk Powder	Carl Roth GmbH + Co. KG, Karlsruhe, Germany
Sodiumacetate, C2H3NaO2	VWR International Germany GmbH, Darmstadt, Germany
Sodium chloride, NaCl	VWR International Germany GmbH, Darmstadt, Germany
Sodium dodecyl sulfate ≥99% (SDS), C12H25NaO4S	Merck Chemicals GmbH, Schwalbach, Germany
Tetramethylethylendiamin (TEMED), (CH3)2NCH2CH2N(CH3)2	Merck Chemicals GmbH, Schwalbach, Germany
Tris(hydroxymethyl)-aminomethan (Tris), NH2C(CH2OH)3	Affymetrix, Santa Clara, California, USA
Xylencyanol, $C_{25}H_{27}N_2NaO_6S_2$	VWR International Germany GmbH, Darmstadt, Germany

2.14 Buffers and Solutions

Table 14. Composition of buffers and solutions used.

Buffer/Solution	Composition	Amounts
5x Laemmli Buffer	Bromphenolblue	0.01 %
	Tris-HCl pH 6.8	60 mM
	β-Mercaptoethanol	5 % (v/v)
	SDS	2 % (w/v)
	Glycerol	10 % (v/v)
	H2O dest.	
Antibody Solution for Western Blot	1x TBS	
	Skimmed Milk Powder	5 % (w/v)
Blocking Solution for Western Blot	1x TBS	
	Skimmed Milk Powder	5 % (w/v)
Lysogeny Broth (LB) Agar	Trypton	1 % (w/v)
	Yeast extract	0.5 % (w/v)
	NaCl	1 % (w/v)
	Bacto-Agar	15 % (w/v)
	MgSO4	0.2 % (w/v)
	H2O dest.	
LB Medium	Trypton	1 % (w/v)
	Yeast extract	0.5 % (w/v)
	NaCl	1 % (w/v)
	H2O dest.	
IPTG Solution	IPTG	0.1 M
	H2O	
SDS Running Buffer, pH 8.6	Tris-HCl	0.25 mM
	Glycine	0.2 M
	SDS	1 % (w/v)
	H2O dest.	
SOC Medium	Tryptone	2 % (w/v)
	Yeast extract	0.5 % (w/v)
	NaCl	10 mM
	KCl	2.5 mM
	MgCl2	10 mM
	Glucose	20 mM
Towbin	Glycine	190 mM

	Tris	0.25 mM
	Methanol	20 % (v/v)
	H2O dest.	
Tris-borate-EDTA (TBE), pH 8.0	Tris	100 mM
	Boric acid	100 mM
	EDTA	1 mM
	H2O dest.	
Tris-buffered saline (TBS), pH 7.5	Tris	50 mM
	NaCl	150 mM
	H2O dest.	
X-Gal Solution	X-Gal	0.04 % (w/v)
	Dimethyformamid	

2.15 Consumables

Table 15. List of consumables used.

Consumable	Source
12- well tissue culture plate	Greiner Bio-One International, Kremsmünster, Austria
6-well tissue culture plate	Greiner Bio-One International, Kremsmünster, Austria
96-well tissue culture assay plate, flat transparent bottom	Greiner Bio-One International, Kremsmünster, Austria
96-well tissue culture assay plate, white, flat non-transparent bottom	Greiner Bio-One International, Kremsmünster, Austria
BD Microlance™ 3 Needles 18G, 20G and 23G	Becton Dickinson (BD), Franklin Lakes, New Jersey, USA
BD Plastipak™ 1ml Luer	Becton Dickinson (BD), Franklin Lakes, New Jersey, USA
Cell scraper	VWR International Germany GmbH, Darmstadt, Germany
ClipTip Pipet tips	Thermo Fisher Scientific, Waltham, Massachusetts, USA
CryoPure tube 1.6 mL	Sarstedt AG & Co., Nümbrecht, Germany
Eppendorf tube 0.5 mL	Sarstedt AG & Co., Nümbrecht, Germany
Eppendorf tube 1.5 mL	Sarstedt AG & Co., Nümbrecht, Germany
Eppendorf tube 2 mL	Sarstedt AG & Co., Nümbrecht, Germany

Falcon tube 15 mL	Sarstedt AG & Co., Nümbrecht, Germany
Falcon tube 50 mL	Sarstedt AG & Co., Nümbrecht, Germany
Immobilon-P polyvinylidene difluoride (PVDF) membrane	Merck Millipore, Burlington, Massachusetts, USA
MicroAmp Optical 384-Well Reaction Plate	Thermo Fisher Scientific, Waltham, Massachusetts, USA
Mini cell scrapers	Biotium, Fremont, California, USA
Nitril gloves	VWR International Germany GmbH, Darmstadt, Germany
Optical Adhesive Film	Thermo Fisher Scientific, Waltham, Massachusetts, USA
Pasteur pipet 3 mL	VWR International Germany GmbH, Darmstadt, Germany
PCR-Cups Multiply®-µStrip 0.2 mL chain	Sarstedt AG & Co., Nümbrecht, Germany
PCR-Cup Lids, 8-fold chain, flat	Sarstedt AG & Co., Nümbrecht, Germany
Petri dishes (10 cm)	Sarstedt AG & Co., Nümbrecht, Germany
Pipet tips 10 µL	VWR International Germany GmbH, Darmstadt, Germany
Pipet tips 100 µL	VWR International Germany GmbH, Darmstadt, Germany
Pipet tips 1000 µL	VWR International Germany GmbH, Darmstadt, Germany
Pipet tips, sterile, with filter	Nerbe Plus GmbH, Winsen, Germany
QIAshredder homogenizer	Qiagen, Hilden, Germany
Serological pipettes	Sarstedt AG & Co., Nümbrecht, Germany
Tissue culture dish 10 cm	Sarstedt AG & Co., Nümbrecht, Germany
Tissue culture flask T25 vent. Cap	Sarstedt AG & Co., Nümbrecht, Germany
Tissue culture flask T75 vent. Cap	Sarstedt AG & Co., Nümbrecht, Germany
Transfer membrane	Merck, Darmstadt, Germany
Whatman paper 3 mm	Thermo Fisher Scientific, Waltham, Massachusetts, USA

2.16 Instruments

Table 16. List of instruments used.

Instrument	Source
ABI3130x1 Genetic Analyzer	Applied Biosystems, Waltham, Massachusetts, USA
Accu-jet Pipet Controller	Brand, Wertheim, Germany
Agilent 2100 BioAnalyzer	Agilent Technologies, Santa Clara, California, USA
Autoclave “Autoklav V-150”	Systec, Linden, Germany
Bunsen burner Gasprofi1	WLD Tec, Göttingen, Germany
CASY TT Cell Counter	Omni Life Science GmbH & Co., Bremen, Germany
Centrifuge 5415R	Eppendorf AG, Hamburg, Germany
Centrifuge 5425	Eppendorf AG, Hamburg, Germany
Centrifuge 5810	Eppendorf AG, Hamburg, Germany
Centrifuge Biofuge fresco	Heraeus Holding GmbH, Hanau, Germany
Centrifuge J2-HS	Beckman Coulter, Brea, California, USA
Centrifuge Megafuge 1.0R	Heraeus Holding GmbH, Hanau, Germany
Centrifuge Mikro 120	Hettich Zentrifugen, Tuttlingen, Germany
Centrifuge Sprout Mini	Heathrow Scientific, Vernon Hills, Illinois, USA
Compact shaker KS 15 A	Edmund Bühler GmbH, Bodelshausen, Germany
Equalizer pipette E1-ClipTip	Thermo Fisher Scientific, Waltham, Massachusetts, USA
Fine scale “Feinwaage Explorer”	OHAUS, Nänikon, Switzerland
Gelelectrophoresis chamber Blue Marine200	SERVA Electrophoresis GmbH, Heidelberg, Germany
Icemachine AF 100	Scotsman, Vernon Hills, Illinois, USA
Incubator for bacteria 37 °C	Memmert GmbH, Schwabach, Germany
Incubator Hera Cell 150	Thermo Fisher Scientific, Waltham, Massachusetts, USA
Incubation hood TH 15	Edmund Bühler GmbH, Bodelshausen, Germany
Inverse Microscope DM IL	Leica, Solmis, Germany
Microplate Reader Spark	Tecan, Männedorf, Switzerland
Microwave MW785	Clatronic, Kempen, Germany
Milli-Q-Synthesis Water Purification System	Merck Chemicals GmbH, Schwalbach, Germany

Mini-PROTEAN Tetra Handcast System	Bio-Rad Laboratories GmbH, Munich, Germany
MS2 Minishaker	IKA, Staufen, Germany
NanoDrop® ND1000 Spectrometer	Thermo Fisher Scientific, Waltham, Massachusetts, USA
Odyssey FC Imager	LI-COR Biosciences, Lincoln, Nebraska, USA
pH Meter Lab 850	SI Analytics GmbH, Mainz, Germany
Power Pack Blue Power 500	SERVA Electrophoresis GmbH, Heidelberg, Germany
Power Pack Blue Plus	SERVA Electrophoresis GmbH, Heidelberg, Germany
Precision scale Adventurer ARC120	OHAUS, Nänikon, Switzerland
QuantStudio™ 5 Real-Time PCR System	Applied Biosystems, Waltham, Massachusetts, USA
Shaking incubator 37 °C	Gesellschaft für Labortechnik (GFL), Burgwedel, Germany
Short Plates Mini PROTEAN®	Bio-Rad Laboratories GmbH, Munich, Germany
Spacer Plates Mini PROTEAN® 1.5 mm	Bio-Rad Laboratories GmbH, Munich, Germany
Thermocyler Peqstar 2x gradient	VWR International Germany GmbH, Darmstadt, Germany
Thermocycler T3	Biometra GmbH, Göttingen, Germany
Thermocycler TProfessional Basic	Biometra GmbH, Göttingen, Germany
Thermomixer compact	Eppendorf AG, Hamburg, Germany
Trans-Blot SD Semi-Dry Transfer Cell	Bio-Rad Laboratories GmbH, Munich, Germany
Transferpipette ® 10 µL	Brand, Wertheim, Germany
Transferpipette ® 100 µL	Brand, Wertheim, Germany
Transferpipette ® 1000 µL	Brand, Wertheim, Germany
Transilluminator UST-30_M-8R	BioView Ltd., Billerica, Massachusetts, USA
Vacuumpump MZ 2 C	Vacuubrand GmbH, Wertheim, Germany
Vibra Cell VCX400 Ultrasound device	Sonics & Materials Inc., Newtown, Connecticut, USA
Vortex Genie2	Scientific Industries, Bohemia, New York, USA
Water destiller	GFL GmbH, Burgwedel, Germany
Waterbath W12	Labortechnik Medigen, Arnsdorf, Germany

Workbench Heraguard	Heraeus Holding GmbH, Hanau, Germany
Workbench Herasafe	Heraeus Holding GmbH, Hanau, Germany

2.17 Software

Table 17. List of software used.

Software	Source
Agilent 2100 Expert Software	Agilent Technologies, Santa Clara, California, USA
ApE – A Plasmid Editor v2.0.61	M. Wayne Davis
Corel Draw Version 21.3.0.755	Corel Corporation, Ottawa, Canada
Image Studio Version 4.0	LI-COR Biosciences, Lincoln, Nebraska, USA
ImageJ 1.53d	Wayne Rasband and contributors, National Institute of Health, USA
NanoDrop 1000 Spectrophotometer V3.8	Thermo Fisher Scientific, Waltham, Massachusetts, USA
Microsoft Office	Microsoft Cooperation, Redmond, Washington, USA
QuantStudio™ Design & Analysis Software v1.4.3	Applied Biosystems, Waltham, Massachusetts, USA
R version 3.6.0	The R Foundation for Statistical Computing
SnapGene 2.8.2	GSL Biotech LLC, San Diego, California, USA
TeXstudio 3.0.1	Benito van der Zander, Jan Sundermeyer, Daniel Braun, Tim Hoffmann

3 Methods

3.1 Cell Culture

All cell lines were kept in a Hera Cell 150 incubator at constant temperature of 37 °C and 5 % CO_2 atmosphere. Cell culture media and supplies were stored at 4 °C unless indicated differently by the manufacturer and pre-warmed to 37 °C before use. Passaging of cells was performed under sterile conditions. The current condition and confluency of cells was checked under a microscope before they were passaged or used in experiments.

3.1.1 Cultivation of Primary Human Umbilical Vein Endothelial Cells (HUVEC)

Human umbilical vein endothelial cells (HUVEC) were cultivated in T25 or T75 flasks with ventilated caps in 10 or 20 mL EBM™ Plus Basal Medium supplemented with EGM™ Plus SingleQuots as stated by the manufacturer but without antibiotics. To prevent contamination, all surfaces and material in the cell culture were cleaned with Incidin™ Plus before usage. HUVECs were passaged when they reached 90 – 100 % confluency. Old medium was removed and cells were washed with 5 or 10 mL Dulbecco's phosphate buffered saline (DPBS). Cells were detached by adding 5 or 10 mL 0.05 % Trypsin in ethylenediaminetetraacetic (EDTA) and after 2 min 5 or 10 mL 20 % fetal bovine serum (FBS) in DPBS were added to stop the reaction. The cell suspension was transferred into a falcon tube. The flask was washed with 5 or 10 mL DPBS to remove remaining cells and the solution was also transferred to the falcon tube. Cells were centrifuged for 5 min at 1,200 rpm at room temperature (RT). The supernatant was removed and cells were washed in 5 mL DPBS. Afterwards, cells were centrifuged again with the same conditions as before. The supernatant was removed and cells were resuspended in fresh medium and transferred to new flasks. HUVECs were sub-cultured at a 1:3 ratio twice a week for maintenance. Cells no older than passage 5 were used for experiments.

3.1.2 Cultivation of Human Embryonic Kidney (HEK293T) Cells

Human embryonic kidney (HEK293T) cells were cultivated in 10 cm dishes in 10 mL Dulbecco's Modified Eagle Medium (DMEM) supplemented with 10 % FBS and 1 % Penicillin/Streptomycin (100 units/mL Penicillin and 100 µg/mL Streptomycin). HEK293T cells were passaged when they reached 90 - 100 % confluency. Old medium was removed, cells were washed off the dish with fresh medium and transferred to new dishes. HEK293T cells were sub-cultured 1:5 twice a week for maintenance.

3.1.3 Transfection of HUVECs

One day before transfection, HUVECs were seeded on 12- or 6-well plates so that they reached a confluency of about 70 - 80 % for transfection. HUVECs were transfected with

HiPerFect transfection reagent according to the manufacturer's protocol and miRCURY LNA miRNA mimics. Experiments were performed 48 h after transfection.

3.1.4 Co-Transfection of HEK293T Cells

HEK293T cells were seeded on 96-well plates without antibiotics one day before transfection. Cells were used for transfection with a confluency of approximately 80 %. HEK293T cells were co-transfected with miRCURY LNA miRNA mimics and the pmirGLO Dual-Luciferase miRNA Target Expression Vector with the Lipofectamine 2000 transfection reagent according to the manufacturer's protocol. Each well was transfected with 30 pmol miRNA mimic and 1 µg reporter vector. Experiments were performed 24 h after transfection.

3.2 Laser-induced neovascularization mouse model

Blood and tissue samples of mice with laser-induced NV were obtained from the Laboratory for Experimental Immunology of the Eye (Department of Ophthalmology, Faculty of Medicine and University Hospital of Cologne, Germany, Head Prof. Dr. Thomas Langmann). This animal study was approved by the government of North Rhine-Westphalia (ID: 84-02.04.2015.A413).

Induction of NV with an Argon laser was performed as described previously [90], with minor modifications as given in detail in Kiel et al. (2020) [91]. In this study, female drug and test naïve C57Bl/6J mice were used. Mice used for cmiRNA detection in blood were 78 days old, while mice used for miRNA detection in tissue were 56 days old. Mice used for miRNA detection in tissues on day 14 were also included in cmiRNA analysis in blood as an independent replication batch and were 56 days old.

For investigation of cmiRNA expression after laser treatment by next generation sequencing (NGS), six mice were treated with an Argon laser on day 1 and blood was drawn on day 0 to assess baseline expression, as well as on day 3 and 14. Further, blood was drawn from five untreated control mice age-matched with day 14 laser-treated samples. For replication of cmiRNA expression after laser treatment, two independent batches of laser-treated mice were used and blood was drawn on day 0, 3, 7 and 14. The first batch included six mice and the second batch included 12 mice. For detection of miRNA expression in ocular tissues, the second batch of animals from the cmiRNA replication study was further used to extract retina and RPE/choroid on day 14. In addition, ocular tissue was also extracted from 12 untreated control mice. For detection of miRNA expression in ocular tissue at day 3 and 7, retina and RPE/choroid were extracted from 12 mice per time point and 12 untreated control mice from a batch of animals, which was independent from day 14 treatment.

For blood samples, approximately 40 µL of peripheral venous blood was drawn from the facial vein and mixed with 120 µL PAXgene Blood RNA tube stabilizing solution. For tissue samples, retina and RPE/choroid of mice were extracted and snap frozen in liquid nitrogen.

Isolation of cmiRNAs from blood and isolation of miRNAs from tissue from day 14 and the respective controls was performed by Patricia Berber (Institute of Human Genetics, University of Regensburg, Germany) as described in detail in Kiel et al. (2020) [91].

3.3 RNA isolation

3.3.1 Isolation of miRNAs

For isolation of miRNAs from HEK293T cells, four wells from a 96-well plate were combined to a single sample. For isolation of miRNAs from tissue from day 3 and 7 and the respective controls, samples were homogenized in 300 µL lysis buffer with pestles and disintegrated by subsequently passing them through 18 G, 20 G and 23 G needles prior to miRNA isolation. Isolation of miRNAs from cells and tissue was performed using the mirVANA™ microRNA isolation kit according to the procedures of organic extraction and total RNA isolation with the following minor modifications. The centrifugation step during the phenol/chloroform extraction was extended to 30 min at 4 °C and RNA was eluted twice in 50 µL (tissue) or 100 µL (cells) of nuclease-free water. Concentration of RNA was determined with a NanoDrop® ND1000 Spectrophotometer. RNA was stored at -20 °C for short term usage and at -80 °C for long term storage.

3.3.2 Isolation of mRNA

For isolation of mRNA, total RNA was isolated with the PureLink™ RNA Mini-Kit according to the manufacturer's instructions including an on-column DNase digestion. RNA was eluted twice in 30 to 50 µL of nuclease-free water. RNA concentration was determined with a NanoDrop® ND1000 Spectrophotometer. RNA was stored at -20 °C for short term storage and at -80 °C for long term storage.

3.4 cDNA Synthesis

3.4.1 polyA tailing and cDNA synthesis of miRNAs

Reverse transcription of miRNAs was performed as described elsewhere [92]. Briefly, 300 ng (RPE/choroid samples), 500 ng (retina samples, HUVECs) or 1 µg (HEK293T) of purified RNA were modified with *Escherichia coli* (*E. coli*) Poly (A) Polymerase I. For this purpose, the RNA was diluted in 12.5 µL of nuclease-free water, 7.5 µL of a reaction mix (**Table 18**) were added and the mixture was incubated for 1 h at 37 °C. The *E. coli* polymerase I synthesizes a polyA

tail, which enables binding of a Universal RT oligonucleotide primer containing a polyT stretch. For this, 10 µL of the polyA solution were incubated at 65 °C for 5 min with 3 µL of a mixture containing the Universal RT oligonucleotide primer (**Table 19**). After samples were cooled down to 4 °C, reverse transcription to complementary DNA (cDNA) was performed with a Superscript™ III reverse transcriptase. To this end, 7 µL of a Superscript™ III mixture (**Table 20**) were added to the samples and incubation was performed according to the following scheme: 5 min at 25 °C, 60 min at 50 °C, 15 min at 70 °C, cool down to 4 °C. The polyA tailed RNA and cDNA were stored at -20 °C for short term storage and at -80 °C for long term storage.

Table 18. Composition of poly(A) tailing reaction mix.

Component	Volume
5X E-PAP buffer	4 µL
25 nM MnCl	1.5 µL
10 mM ATP solution	1.5 µL
E. coli Poly(A) Polymerase I	0.8 µL

Table 19. Composition of mixture for Universal RT oligonucleotide primer addition.

Component	Volume
100 µM Universal RT oligonucleotide primer	1 µL
dNTPs (1.25 mM)	1 µL
Nuclease-free H_2O	1 µL

Table 20. Composition of complementary DNA (cDNA) synthesis reaction mix for polyA tailed miRNAs.

Component	Volume
5X first-strand buffer	4 µL
0.1 mM DTT	1 µL
Superscript™ III	1 µL
Nuclease-free H_2O	1 µL

3.4.2 cDNA synthesis of mRNA

For cDNA synthesis of total RNA, up to 3 µg of total RNA were diluted in 11 µL nuclease-free water and mixed with 1 µL Random Hexamer Primers. The mixture was incubated for 5 min at

65 °C and afterwards the cDNA synthesis reaction mix containing a RevertAid™ Reverse Transcriptase (**Table 21**) was added. The mixture was incubated for 10 min at 25 °C, followed by 1 h at 42 °C and finally 10 min at 70 °C. The cDNA was stored at -20 °C for short term storage and at -80 °C for long term storage.

Table 21. Reaction mix for cDNA synthesis of mRNA.

Component	Volume
5X reaction buffer for ReverdAid™ Reverse Transcriptase	4 µL
dNTPs (1.25 mM)	2 µL
RevertAid™ Reverse Transcriptase	1 µL
Nuclease-free H_2O	1 µL

3.5 Quantitative Reverse Transcription PCR (qRT-PCR)

3.5.1 Detection of miRNAs

For detection of miRNAs by quantitative reverse transcription PCR (qRT-PCR), 2.5 µg of cDNA were diluted in 4 µL of nuclease-free water. Afterwards, 5 µL of Takyon™ Low ROX SYBR MasterMix mixed with 10 µM Universal Primer and 10 µM miRNA primer diluted in 1 µL purified water (Millipore) were added to the cDNA. Primers to detect mature miRNAs contain the mature miRNA sequence and were modified as described elsewhere [93] with a polyA overhang to improve performance in long termed stored RNA. The qRT-PCR reactions were conducted in technical triplicates on 384-well plates in a QuantStudio™ 5 Real-Time PCR System. The experiments were set up with the ΔΔCt (cycle threshold) method [94] using SYBR Green reagents as described in **Table 22**.

Table 22. qRT-PCR conditions for miRNA detection.

Stage	Time	Temperature	Cycles
Hold Stage	2 min	50 °C	
	10 min	95 °C	
PCR Stage	15 sec	95 °C	40
	1 min	60 °C	
Melt Curve Stage	15 sec	95 °C	
	1 min	60 °C	
	15 sec	95 °C	

Measurements were excluded if the standard deviation (SD) of technical replicated was greater than 0.4 Ct values. In miRNA overexpression models, expression of the miRNA of interest was normalized to samples transfected with the control miRNA cel-miR-39. Overexpression of the control miRNA was normalized to samples transfected with the miRNA of interest.

3.5.2 Detection of mRNA

Primers for detection of mRNA were designed based on the "Universal Probe Library" of Hoffmann-La Roche. For each qRT-PCR reaction, 50 ng of cDNA were diluted in 2.5 µL and 7.5 µL of a reaction mix as given in **Table 23** were added. Samples were investigated in technical duplicates or triplicates on 384-well plates using a QuantStudio™ 5 Real-Time PCR System. Set up of the experimental qRT-PCR conditions is given in **Table 24**. Data were analyzed according to the ΔΔCt approach [94]. Measurements with a SD of technical replicates greater than 0.4 Ct values were excluded and expression of genes was normalized to the housekeeper gene *Hypoxanthine Phosphoribosyltransferase 1* (*HPRT1*).

Table 23. Composition of qRT-PCR reation mix for mRNA detection.

Component	Volume
Takyon™ Low ROX Probe 2X MasterMix dTTP Blue	5 µL
Primers (forward and reverse, each 10 µM)	1 µL
Probe	0.125 µL
Purified H_2O (Millipore)	1.375 µL

Table 24. qRT-PCR conditions for mRNA detection.

Stage	Time	Temperature	Cycles
Hold Stage	10 min	95 °C	
PCR Stage	15 sec	95 °C	40
	1 min	60 °C	

3.6 RNA sequencing (RNA-Seq)

3.6.1 Library preparation

For RNA sequencing (RNA-Seq) libraries were prepared with the NEXTflex Rapid Directional mRNA-Seq Kit according to the manufacturer's instructions with up to 100 ng of total RNA, which was enriched by Poly(A) Beads included in the kit. In total, eight samples of HUVECs transfected with hsa-miR-4513-A, hsa-miR-4513-G or cel-miR-39 from three independent

experiments were used for sequencing. Successful overexpression of miRNAs was validated by qRT-PCR before library preparation. Quality of generated libraries was verified by Agilent BioAnalyzer DNA High-Sensitivity Chips according to the manufacturer's instructions run on an Agilent 2100 BioAnalyzer.

3.6.2 RNA-Seq

RNA-Seq was performed at the Genomics Core Facility "KFB - Center of Excellence for Fluorescent Bioanalytics" (University of Regensburg, Regensburg, Germany; www.kfb-regensburg.de) as described in detail elsewhere [95].

3.7 Sodium dodecyl sulfate (SDS) Polyacrylamide Gel Electrophoresis

For Western Blot analysis, proteins were separated by reducing sodium dodecyl sulfate (SDS) polyacrylamide gel electrophoresis on 10 % (for DDX46), 12.5 % (for CD2BP2, TPM3 and KLF6) or 15 % (for p16 INK4A) acrylamide gels. Compositions of acrylamide gels are given in **Table 25** and **Table 26** and gels were cast using Bio-Rad MiniPROTEAN® equipment. Samples were prepared by combining two wells from a 6-well plate to obtain total protein extracts by homogenization in DPBS. For this, sonication for 15 sec at 37 % was performed with a Vibra Cell VCX400 Ultrasound device. Afterwards, 5X Laemmli buffer was added and samples were heated at 95 °C for 10 min. 10 to 40 µL of samples were loaded on the acrylamide gels, as well as 3.5 µL of PageRuler™ Prestained Protein Ladder as size standard. Gels were run at 50 V in SDS running buffer until samples entered the resolving gel. At this time point, gels were run at 150 V for 1 to 1.5 h.

Table 25. Composition of acrylamide resolving gels.

Component	Volume 10 % gel	Volume 12.5 % gel	Volume 15 % gel
1 M Tris-HCl pH 8.8	3.8 mL	3.8 mL	3.8 mL
H_2O dest.	3.7 mL	3 mL	2.4 mL
Polyacrylamide (40 %)	2.5 mL	3.1 mL	3.8 mL
SDS (20 %)	100 µL	100 µL	100 µL
APS (10 %)	100 µL	100 µL	100 µL
TEMED	10 µL	10 µL	10 µL

Table 26. Composition of 3 % acrylamide stacking gels.

Composition	Volume

1 M Tris-HCl pH 6.8	2.8 mL
H_2O dest.	1.7 mL
Polyacrylamide (40 %)	0.6 mL
SDS (20 %)	50 µL
APS (10 %)	50 µL
TEMED	5 µL

3.8 Western Blot

After separation of proteins on acrylamide gels, proteins were transferred to Immobilon-P polyvinylidene difluoride (PVDF) membranes by semi-dry blotting technique. Membranes were activated in methanol for 30 sec and equilibrated in Towbin buffer for 5 min. Further, SDS gels and two Whatman papers were also equilibrated in Towbin buffer. Transfer of proteins from SDS gels to membranes was performed at 24 V for 40 min. Afterwards, membranes were transferred to blocking solution for 1 h at RT. After blocking, membranes were incubated over night at 4 °C with primary antibodies. On the next day, membranes were washed three times with TBS for 5 min at RT. Afterwards, membranes were incubated with the secondary antibody for 4 h at RT. Membranes were washed again three times with TBS for 5 min at RT. Visualization of protein bands was performed with Clarity™ ECL Western Blotting Substrate according to the manufacturer's instructions on an Odyssey FC imager. In case proteins display only weak signals, Clarity Max™ Western Blotting Substrate was used. Signal intensities were quantified with the Image Studio software Version 4.0 and proteins were normalized to heat shock protein 90 (HSP90) or β-actin (ACTB) signals from the same blot.

3.9 Generation of luciferase reporter constructs

3.9.1 Amplification of 3'-untranslated regions (3'-UTR) by PCR

To investigate binding of hsa-miR-4513 to the 3'-UTR of target genes, luciferase reporter constructs were generated. Sequences of 3'-UTRs were obtained from the USCS Genome Browser (GRCh38) [96], available at https://genome.ucsc.edu/, and sequences were downloaded with the UCSC Table Browser tool [97]. In case several transcripts were available for one gene, the most prominent transcript found in the RNA-Seq data was used, with the two following exceptions. Two transcripts with a comparable expression in the RNA-Seq data were available for *CD2BP2*. One of those transcripts (ENST00000569466) had a relatively short 3'-UTR with a length of 138 bp, which is also a part of the 3'-UTR of the second transcript (ENST00000305596) with a length of 2,212 bp. Therefore, the 3'-UTR sequence of the longer

transcript was chosen for further investigations. The second exception is *CDKN2A*. Four transcripts of *CDKN2A* displayed a comparable expression in the RNA-Seq data, including one transcript encoding the p14 protein (ENST00000579755) and three transcripts encoding different isoforms of the p16 protein (p16 transcript 1: ENST00000304494, p16 transcript 2: ENST00000578845, p16 transcript 3: ENST00000579122). For all four transcripts luciferase reporter vectors were generated.

3'-UTRs were amplified using 60 – 150 ng cDNA and PCR conditions as indicated in **Table 27**. PCR reaction mix for GoTaq® DNA polymerase is given in **Table 28**, and mixes for Phusion™ High-Fidelity DNA polymerase and GoTaq® Long PCR DNA polymerase are given in **Table 29** and **Table 30**. Thermocycler programs for PCR reactions are given in **Table 31** and **Table 32**.

Table 27. 3'-Untranslated regions (3'-UTR) and their amplification conditions.

3'-UTR	Product length	cDNA origin	Polymerase	Annealing temperature	Elongation time
CD2BP2	2,175 bp	HEK293T cells	GoTaq®	58 °C	2 min
CDKN2A (p14 transcript)	567 bp	HUVECs	GoTaq®	55 °C	1 min
CDKN2A (p16 transcript 1)	459 bp	HEK293T cells	Phusion™	57 °C	1 min
CDKN2A (p16 transcript 2)	200 bp	HUVECs	GoTaq®	58 °C	1 min
CDKN2A (p16 transcript 3)	161 bp	HEK293T cells	GoTaq®	58 °C	1 min
DDX46	410 bp	HEK293T cells	Phusion™ + DMSO	55 °C	1 min
ITPRIPL2	5,520 bp	HEK293T cells	GoTaq® Long PCR	53 °C	6 min
KLF6	3,537 bp	HUVECs	GoTaq® Long PCR	55 °C	3.5 min
TPM3	1,214 bp	HEK293T cells	Phusion™ + DMSO	58 °C	1.5 min

Table 28. PCR reaction mix with GoTaq® DNA polymerase.

Component	Volume
Purified H_20 (Millipore)	16.9 µL
5X Green GoTaq® Reaction Buffer	5 µL

dNTPs (1.25 mM)	1 µL
Primer forward and reverse (each 10 µM)	1 µL
GoTaq® DNA polymerase	0.1 µL

Table 29. PCR reaction mix with Phusion™ High-Fidelity DNA polymerase.

Component	Volume without DMSO	Volume with DMSO
Purified H_20 (Millipore)	13.25 µL	12.5 µL
DMSO	-	0.75 µL
5X Phusion™ GC Buffer	5 µL	5 µL
dNTPs (1.25 mM)	0.5 µL	0.5 µL
Primer forward and reverse (each 10 µM)	1 µL	1 µL
Phusion™ High-Fidelity DNA polymerase	0.25 µL	0.25 µL

Table 30. PCR reaction mix with GoTaq® Long PCR DNA polymerase.

Component	Volume
Purified H_20 (Millipore)	18 µL
2X GoTaq® Long PCR Master Mix	25 µL
Primer forward and reverse (each 10 µM)	2 µL

Table 31. PCR conditions for PCR amplification with GoTaq® and Phusion™ DNA polymerases.

Reaction step	Temperature	Duration	Cycles
Initial denaturation	94 °C	4 min	
Denaturation	94 °C	30 sec	
Annealing	x °C	30 sec	33
Elongation	72 °C	x min	
Final elongation	72 °C	4 min	
Pause	4 °C	∞ min	

X indicates variable temperature and duration, adjusted for each 3'-UTR to be amplified as given in **Table 27**.

Table 32. PCR conditions for PCR amplification with GoTaq® Long PCR DNA polymerase.

Reaction step	Temperature	Duration	Cycles
Initial denaturation	95 °C	2 min	
Denaturation	94 °C	30 sec	
Annealing	x °C	30 sec	35
Elongation	65 °C	x min	
Final elongation	72 °C	10 min	
Pause	4 °C	∞ min	

X indicates variable temperature and duration, adjusted for each 3'-UTR to be amplified as given in **Table 27**.

Noteworthy, it was not possible to amplify the full length of the 3'-UTR of *ITPRIPL2*. Although a protein coding transcript was annotated (ENST00000381440), little is known so far about this transcript and its protein. The annotated transcript has a length of 5,560 bp and all attempts to amplify this 3'-UTR produced a 2,509 bp deletion from nucleotide 2,147 to nucleotide 4,655 of the *ITPRIPL2* 3'-UTR. This might be due to highly complementary regions within the deleted sequences with a length of > 14 bp. To this end, the 3'-UTR sequence of *ITPRIPL2* with the deletion was used to create a luciferase reporter vector.

3.9.2 Agarose gel electrophoresis

Correct product size and purity of PCR products were verified by agarose gel electrophoresis. Agarose gels were prepared by heating 1 – 2 % (w/v) agarose in TBE buffer until the agarose solved completely. The solution was cooled down and 4 drops of a 0.003 % ethidium bromide solution were added.

Bromphenolblue or xylencyanol were added to the PCR products and samples were loaded on the agarose gel with addition of 3 µL GeneRuler™ DNA Ladder Mix as a size standard. Gels were run at 190 V for 20 min.

3.9.3 Purification of PCR products from agarose gels

PCR products of the correct size were excised from gels. Purification of PCR products was performed with the NucleoSpin® Gel and PCR Clean-up kit according to the manufacturer's instructions. DNA was eluted twice with 15 µL of purified water (Millipore) and concentration was determined with a NanoDrop® ND1000 Spectrophotometer. Purified products were stored at -20 °C until further use.

3.9.4 Ligation into pGEM®-T

Amplified 3'-UTRs were ligated into the pGEM®-T vector. For this purpose, the ligation mix given in **Table 33** and the supplied ligase of the pGEM®-T vector kit was used. A molar ratio of 3:1 of the purified PCR and the pGEM®-T vector product was used. Mixtures were incubated over night at 4 °C.

Table 33. pGEM®-T vector ligation mix.

Component	Volume
pGEM®-T vector	1 µL
Purified PCR product	x µL
2X T4 DNA Ligase Buffer	5 µL
T4 DNA Ligase	1 µL
Purified H_2O (Millipore)	Ad. 10 µL

X indicates variable amount of purified PCR product, which was calculated in a 3:1 molar ratio to the amount of vector DNA used.

3.9.5 Heat shock transformation in *E. coli*

Plasmid DNA was introduced into *E. coli* strain DH5α by heat shock transformation. An aliquot of 100 µL competent *E. coli* cells was thawed on ice. The ligation mixture was added to the cells and the tube was flicked to mix cells and the ligation mixture. Afterwards, incubation on ice was performed for 30 min followed by a heat shock step, whereby cells were placed on 42 °C for 45 sec and then returned to ice for 10 min. 400 µL of SOC medium were added to the cells and cells were incubated for 1.5 h at 37 °C. Afterwards, cells were plated on LB plates containing 100 µg/mL ampicillin. In case *E. coli* were transformed with pGEM®-T, a blue/white screening was performed. For this purpose, LB plates were prepared with a mixture of 10 µL Isopropyl-β-D-thiogalactopyranoside (IPTG) and 50 µL 5-Bromo-4-chloro-3-indoxyl-β-D-galactopyranoside (X-Gal) solutions before plating cells.

3.9.6 Plasmid DNA Miniprep

Single clones of transformed *E. coli* cells were picked from LB plates and transferred to 5 mL LB medium containing 100 µg/mL ampicillin. Clones were incubated over night at 37 °C and on the next day DNA isolation was performed with the NucleoSpin® Plasmid kit according to the manufacturer's instructions. Elution of plasmid DNA was carried out with 50 µL of purified water (Millipore) and the concentration was determined with a NanoDrop® ND1000

Spectrophotometer. Plasmid DNA was stored at 4 °C for short term storage and at -20 °C for long term storage.

3.9.7 Sanger Sequencing

Sanger sequencing of the vector inserts was performed to verify the correctness of the inserted 3'-UTR sequences. For this, the BigDye® Terminator v3.1 Cycle Sequencing kit was used. The reaction mixture is given in **Table 34** and the thermocycler program in **Table 35**.

Table 34. Reaction mixture for Sanger sequencing.

Component	Volume
Plasmid DNA (25 ng/µL)	2 µL
BigDye® Terminator Reaction Mix	0.3 µL
5X BigDye® Terminator Sequencing Buffer	2 µL
Primer (10 µM)	1 µL
Purified H_2O (Millipore)	4.7 µL

Table 35. Thermocycler program for cycle sequencing.

Reaction step	Temperature	Duration	Cycles
Initial denaturation	94 °C	5 min	
Denaturation	94 °C	30 sec	
Annealing	55 °C	30 sec	27
Elongation	60 °C	3 min	
Final elongation	60 °C	5 min	
Pause	4 °C	∞ min	

For DNA precipitation, 2 µL of sodium acetate (3 M) and 25 µL of ethanol (100 %) were added to the samples. After 10 min of incubation at RT, samples were centrifuged at 4,000 rpm for 45 min at 4 °C. The supernatant was removed and 100 µL 70 % ethanol was added to the samples. Samples were again centrifuged at 4,000 rpm for 30 min at 15 °C. The supernatant was discarded and 15 µL of HiDi™ formamide was added to the samples. Samples were transferred to a 96-well plate and sequenced on an ABI3130x1 Genetic Analyzer. Sequences were analyzed using SnapGene 2.8.2.

3.9.8 Restriction digestion

After confirmation of correct 3'-UTR sequences as insert in the pGEM®-T vector by Sanger sequencing, 3'-UTRs were transferred from pGEM®-T vector into the pmirGLO Dual-Luciferase miRNA Target Expression vector. To this end, restriction sides were added in the initial amplification of 3'-UTR sequences by the amplification primers. Restriction digestion mixtures were prepared as given in **Table 36** and were incubated over night at 37 °C. Digested DNA was separated by agarose gel electrophoresis, DNA fragments of the correct size were excised from the gel and purified as described before. Concentration of DNA was determined by a NanoDrop® ND1000 Spectrophotometer.

Table 36. Mixture for restriction digestion of plasmid DNA.

Component	Volume
Plasmid DNA	1 µg
Enzyme 1	1 µL
Enzyme 2	1 µL
10X CutSmart® Buffer	2 µL
Purified H_2O (Millipore)	Ad. 20 µL

3.9.9 Dephosphorylation

For transfer of the *ITPRIPL2* 3'-UTR from the pGEM®-T vector into the pmirGLO vector, an additional dephosphorylation step was included as no separation of the pGEM®-T vector and the 3'-UTR by agarose gel electrophoresis was possible due to the same size of the vector backbone and the insert. Restriction digestion and purification was performed as described before and the purified product was dephosphorylated by an Antarctic Phosphatase as described in **Table 37** for 30 min at 37 °C followed by 2 min at 80 °C to prevent religation of the 3'-UTR into the pGEM®-T vector. The dephosphorylated product was purified again with the NucleoSpin® Gel and PCR Clean-up kit as described above. Concentration of DNA was determined by a NanoDrop® ND1000 Spectrophotometer.

Table 37. Composition of Antarctic Phosphatase reaction mixture.

Component	Volume
Purified product	12 µL
10X Antarctic Phosphatase Reaction Buffer	2 µL
Antarctic Phosphatase	1 µL

Purified H_2O (Millipore)	5 µL

3.9.10 Ligation in pmirGLO luciferase reporter vector

3'-UTR sequences were ligated with the pmirGLO luciferase reporter vector in a 3:1 molar ratio using a T4 DNA ligase as described in **Table 38**. Ligation mixtures were incubated over night at 4 °C and transformed on the following day into *E. coli* strain JM109 cells as described before.

Table 38. Reaction mixtures for ligation of 3'-UTRs into the luciferase reporter vector.

Component	Volume
Vector DNA	10 – 30 ng
Insert DNA	x ng
10X T4 DNA Ligase Buffer	1 µL
T4 DNA Ligase	1 µL
Purified H_2O (Millipore)	Ad. 10 µL

X indicates variable amount of insert DNA, which was calculated in a 3:1 molar ratio to the amount of vector DNA used.

3.9.11 Colony PCR

To pre-select single clones of transformed *E. coli* cells and check for insert ligation a colony PCR was performed. Single clones were picked from plates and transferred to 20 µL LB medium containing 100 µg/mL ampicillin. Single clones were incubated for 2h at 37 °C and afterwards a PCR reaction was performed with GoTaq® DNA Polymerase as described in **Table 39** and PCR conditions as described in **Table 31**.

Table 39. PCR reaction mix for colony PCR.

Component	Volume
E. coli culture	3 µL
Purified H_20 (Millipore)	17 µL
5X Green GoTaq® Reaction Buffer	2.5 µL
dNTPs (1.25 mM)	0.5 µL
Primer forward and reverse (each 10 µM)	1.6 µL
GoTaq® DNA polymerase	0.4 µL

3.9.12 Plasmid DNA "Midi" preparation

Pre-selected single clones of successfully transformed *E. coli* cells were used for Plasmid DNA Miniprep and Sanger Sequencing to confirm correctness of the 3'-UTR sequences, both as described before. Clones with correct 3'-UTR sequences were used to prepare 100 mL over night *E. coli* cultures in LB medium containing 100 µg/mL ampicillin. DNA plasmids were isolated using the NucleoBond® XtraMidi kit according to the manufacturer's instructions. Plasmids were eluted twice in 100 µL purified water (Millipore) and DNA concentration was determined using a NanoDrop® ND1000 Spectrophotometer. Concentrations were adjusted to 1,000 µg/µL and plasmid DNAs were stored at -20 °C.

3.9.13 Preparation of glycerolstocks for long term storage

For long term storage of bacterial cultures glycerolstocks were generated. For this, 825 µL of fresh over night cultures were mixed with 175 µL sterile glycerol (87 %). The mixture was immediately frozen at -80 °C and specifications about plasmid constructs were added to the database for glycerol cultures of the Institute of Human Genetics.

3.10 Dual-Luciferase reporter assay

To investigate binding of hsa-miR-4513 to 3'-UTRs of target genes, a luciferase reporter assay was performed. For this purpose, HEK293T cells were co-transfected with miRCURY LNA miRNA mimics and the luciferase reporter vector containing the 3'-UTR of interest in white 96-well plates with non-transparent flat bottoms. A second control 96-well plate with transparent bottom was used to assess confluency and current condition of the cells before transfection. 24 h after co-transfection, a luciferase reporter assay was performed using the Dual-Glo® Luciferase Assay System according to the manufacturer's instructions. Untreated HEK293T cells served as background signal control and the luminescence signal of the firefly luciferase was corrected for transfection efficiency by the internal control *Renilla* luciferase. Six technical replicates were used per condition on each plate and data was only used if the SD of the replicates was below 0.3, whereby up to two outliers of the six replicates were excluded if necessary.

3.11 Statistical evaluation

Wet lab experiments were, if not indicated otherwise, statistically evaluated by a Kruskal-Wallis test performed in R [98]. Correction for multiple testing was performed with the Dunn's multiple comparison test using the Benjamini Hochberg method implemented in the Fisheries Stock

Analysis (FSA) package v0.8.26 [99] in R. For experiments conducted with transfected cell lines, cells transfected with cel-miR-39 served as control.

4 Bioinformatical protocols

4.1 Identification of altered cmiRNA expression in NGS data

NGS data processing and quality control (QC) was performed by Dr. Felix Grassmann (Institute of Human Genetics, University of Regensburg) and validated by Dr. Tobias Strunz (Institute of Human Genetics, University of Regensburg) as described in detail in Kiel et al. (2020) [91]. For the identification of altered cmiRNAs from blood samples of day 3 and day 14 in comparison to their baseline expression on day 0, a linear mixed effects model implemented in the nlme package [100] for the statistical software R [98] was used. To be regarded as potential candidate, cmiRNAs had to fulfill the following criteria: p-value < 0.05 and an absolute slope > 0.4. For the comparison of the two control groups, baseline samples from day 0 and untreated animals, a Firth's bias-reduced logistic regression model implemented in the logistf package [101] was used. Candidates, which fulfilled the same criteria as above (p-value < 0.05 and absolute slope > 0.4) were excluded from further analysis. Finally, candidate cmiRNAs were validated by comparing their expression between day 3 or day 14 samples with untreated control samples. This analysis was performed by applying a linear fixed effects model implemented in R. Candidates were considered to be validated if they replicated their slope direction from the initial comparison with day 0 samples and only cmiRNAs with an absolute slope > 0.2 were kept.

4.2 Analysis of qRT-PCR data to replicate cmiRNAs and investigate miRNA expression in ocular tissue

Data of cmiRNA and miRNA expression in the mouse model of laser-induced NV generated by qRT-PCR were normalized using the trimmed mean of M-values (TMM) method implemented in the edgeR package [102]. Afterwards, expression of cmiRNAs was normalized to the median expression of day 0. Expression of miRNAs in ocular tissue was normalized to the median expression of untreated control animals. All batches were normalized separately. Expression of cmiRNAs was analyzed using a linear mixed effects model as described above. Candidate cmiRNAs were considered to be positively replicated if the slope indicated the same direction as in the initial NGS analysis and the p-value was below 0.05. To analyze expression of miRNAs in ocular tissue, a linear fixed effects model implemented in R was used. Obtained p-values were corrected for multiple testing using the false discovery rate (FDR, q-value) [103] implemented in the multtest package [104]. Q-values < 0.05 were considered significant.

4.3 Generation of a GWAS collection

To study pleiotropic effects of AMD-associated genes, a collection of GWAS results was created. This built on data of a previous study, which included 60 diverse phenotypes [41]. For the present work, this collection was extended to 82 phenotypes, including AMD, which are distributed across 12 different phenotype groups (**Supplementary Table 1**). For this purpose, a literature search was conducted in PubMed and the GWAS Catalog [105], until November 2016, for GWAS including primarily individuals of European descent. Studies were only included if at least three genetic variants reached the threshold of genome-wide significance (p-value < 5×10^{-08}) and if relevant data, including effect sizes, effect alleles and association p-values, were available. Only genetic variants on the autosomes were included. Further, only independent genetic signals were kept for analysis by excluding correlated variants ($R^2 > 0.5$) to avoid multiple assignments of AMD-associated genes to one genetic signal.

4.4 Pleiotropy of AMD-associated genes

AMD-associated genes identified in a recent transcriptome-wide association study (TWAS) [83] by Dr. Tobias Strunz (Institute of Human Genetics, University of Regensburg) were checked for pleiotropy by analyzing them for physical overlap with GWAS loci. For this purpose, GWAS loci were defined by extending GWAS signals from 82 phenotypes from the aforementioned GWAS collection with data from the 1000 Genomes reference data [106]. All variants in LD, defined as $R^2 > 0.5$, with GWAS lead variants were extracted and used to define start and stop position of the GWAS locus. Overlapping GWAS loci were merged. Next, all ensemble annotated genes (version 90) [107] were extracted and mapped to the GWAS loci. AMD-associated genes were extracted and checked for pleiotropic effects.

To determine statistical significance for enrichment of physical overlap of AMD-associated genes with GWAS loci of distinct phenotypes, a Fisher's exact test for count data was used. For this purpose, a list of AMD-associated genes was compared to all 24,388 predictable genes in the TWAS approach in at least one tissue with exception of the major histocompatibility complex locus. The list of all 24,388 predictable genes was scaled down to 106 genes to obtain a comparable number of genes for both groups. Contingency tables were created to compare the physical overlap of genes of interest with all TWAS genes and analyzed by the *fisher.test* function implemented in R.

4.5 Description of datasets used to study associations with 15q24.1

For all AMD association studies, data from the IAMDGC [20] was used. Only unrelated individuals of European descent were included, which comprised 14,352 males and 19,624 females. This dataset included 16,144 late stage AMD cases and 17,832 control individuals. Late stage AMD cases consisted of 10,749 NV patients, 3,235 GA patients and 2,160 patients with combined NV and GA. Additionally, this dataset included 6,657 patients with early or intermediate AMD, which were only included in the early AMD association analysis. Detailed information about selection criteria, ophthalmological grading, QC of the genetic data and imputation protocols are described elsewhere [20]. Prior to analysis, genetic variants with an imputation quality < 0.3 were excluded and genotypes were converted into allele dosage format.

The dataset from the Resource for Genetic Epidemiology Research on Adult Health and Aging (GERA) cohort, a sub-study of the Research Program on Genes, Environment, and Health (RPGEH) [108], was used to increase the sample sizes for the association analysis of rs2168518 with AMD. This dataset included 2,874 AMD cases and 26,306 control individuals, all of European descent and born before 1948. The study comprised 12,734 males and 16,446 females. Detailed information about array design [109], genotyping protocol and QC [110], as well as imputation [111] are reported elsewhere. Genotypes were converted into allele dosage format prior to analysis.

To investigate the pleiotropic effect of rs2168518, publicly available GWAS summary statistics of the UK Biobank cohort [112] were used. These were available for both sexes including 361,194 individuals, as well as separately for females including 194,174 individuals and males including 167,020 individuals. Additionally, original data from the UK Biobank Resource (under application number 44862) were used to extract specific phenotype information. Only self-reported white individuals were included in the analysis and related individuals up to the third degree of kinship were excluded. Further, individuals with inconsistencies in the self-reported sex and the genetic sex were excluded. Overall, 379,356 individuals remained for analysis, including 204,527 females and 174,829 males.

4.6 Association analysis of rs2168518 with AMD

To investigate the association of rs2168518 at 15q24.1 with AMD, an association analysis was performed in the GERA and IAMDGC dataset, separately for each dataset and in the combined dataset. For the association analysis of rs2168518 in the GERA dataset, a proxy of rs2168518 in full LD ($R^2 = 1$), namely rs1378942, was used. For the association analysis of rs2168518 with AMD in the GERA or IAMDGC dataset, a logistic regression model was applied using the

glm function implemented in R [98] with adjustment for gender. For the association analysis with the combined IAMDGC and GERA datasets, adjustment was performed for dataset and gender. For identification of genome-wide significant associations in the combined analysis the p-value threshold was set to 5×10^{-08}.

To investigate the association or rs2168518 with AMD subtypes only the IAMDGC dataset was used, as no information about AMD subtypes was provided for the GERA dataset. A logistic regression model was applied as described above, but with adjustment for age, gender, the first two genotype principle components and the source of DNA (whole genome amplification: yes or no). Correction for multiple testing was performed using the FDR as described above.

A conditional analysis was performed to determine whether a single association signal in the 15q24.1 locus with AMD occurs or if there are multiple independent association signals present. For this purpose, a logistic regression model was used for all late stage AMD samples in the IAMDGC dataset. Adjustment was performed as described above for the AMD subtype analysis, but with additional adjustment for the genetic variant with the smallest p-value of AMD association in the 15q24.1 locus (rs11072508, R^2 to rs2168518 = 0.903 in Europeans).

4.7 Phenome-wide association analysis of rs2168518 in the UK Biobank dataset

To investigate a potential pleiotropic effect of rs2168518, the UK Biobank PheWeb browser [113] was searched for associations of rs2168518 with different phenotypes. The PheWeb database compromises GWAS results of 2,419 phenotypes performed in UK Biobank data of approximately 337,000 unrelated British individuals [114]. Associations of rs2168518 were extracted if the p-value was below 1×10^{-04}. Additionally, the association results of rs2168518 with “Eye problems/disorders: Macular degeneration” were extracted, as it did not reach the p-value threshold. GWAS summary statistics of UK Biobank data for all phenotypes significantly associated with rs2168518 according to the PheWeb browser and for “Eye problems/disorders: Macular degeneration” were downloaded from http://www.nealelab.is/uk-biobank/ [112]. To visualize GWAS results, LocusZoom plots [21,115] were generated with all GWAS summary statistics. These plots were used to manually narrow the region of interest to 0.6 Mbp (Chromosome 15: 75,000,000–75,600,000, GRCh37). This region was defined to include all association signals of the previously selected phenotypes for further investigations.

4.8 Colocalization analysis

A colocalization analysis was performed to investigate whether phenotype association signals at 15q24.1 correspond to the same genetic signal as the association signal of AMD. For this,

GWAS summary statistics from the UK Biobank dataset were compared with association results from the IAMDGC dataset using the coloc package [116] in R. To perform this analysis, coloc requires several information as input, including association results, as well as data about the proportion of cases for case-control phenotypes and the SD of the phenotype measurement for quantitative traits. For UK Biobank GWAS summary statistics of case-control studies, the proportion of cases had to be derived from the indicated sample sizes. Missing individuals were not incorporated in those numbers and therefore had to be considered separately. However, the number of missing individuals only referred to the GWAS performed with both sexes. To estimate the number of missing individuals in the GWAS for the separated sexes, the number of missing individuals was divided by two, with the assumption, that missing individuals were spread evenly across sexes. For quantitative traits, the SD of the phenotype measurement was either extracted from the UK Biobank Data Showcase [117] using the value from the initial assessment visit (for “Creatinine (enzymatic) in urine” and “Sodium in urine”) or directly from the UK Biobank data (for “Diastolic blood pressure, automated reading” and “Systolic blood pressure, automated reading”). The SDs of blood pressure measurements were calculated for both sexes and also separately for females and males.

Colocalization analysis was further performed to investigate gender specificity of association signals in the UK Biobank data. For this purpose, GWAS summary statistics of GWAS performed in females were compared with summary statistics from GWAS for the same phenotype performed in male individuals.

Colocalization probabilities indicate, whether the association signal of two phenotypes are identical or if there are independent association signals for two different phenotypes or respectively sexes. A threshold for coloc probabilities of > 0.8 was used.

4.9 Functional annotation of genetic variants at 15q24.1

For functional annotation of the 15q24.1 locus, all genetic variants in LD with rs2168518 (**Supplementary Table 2**), defined as $R^2 > 0.8$ in Europeans, were analyzed regarding their impact on TF binding by the online database RegulomeDB 2.0 [118,119]. This online database was created to enable the identification of DNA features and regulatory elements in non-coding regions of the human genome. Variants with a RegulomeDB rank smaller than 3 were selected for further analysis, representing only variants with a high evidence to alter TF binding sites.

4.10 RNA-Seq analysis

RNA-Seq data processing and QC was performed by Dr. Tobias Strunz (Institute of Human Genetics, University of Regensburg) as described in detail elsewhere [95]. Processed data

were obtained in counts per million (CPM) format. To identify target genes of hsa-miR-4513, a linear regression model was applied using the *lm* function implemented in R to correlate gene expression with miRNA mimic transfection, including an adjustment for transfection batches. Only protein coding genes were retained for analysis and correction for multiple testing was performed using the FDR as described above. Q-values below 0.01 were considered significant. Allele-specific target genes of hsa-miR-4513 had to fulfill the following criteria: significantly reduced expression in comparison to cel-miR-39 transfected samples and a significantly altered expression between hsa-miR-4513-A and hsa-miR-4513-G transfected samples.

4.11 Medical relevance of allele-specific target genes of hsa-miR-4513

Allele-specific target genes of hsa-miR-4513 identified in the RNA-Seq, which also displayed a significant difference in expression in comparison to the control samples in the independent replication analysis by qRT-PCR for at least one allele of hsa-miR-4513 were investigated for their medical relevance. For this purpose, data were extracted from publicly available databases, including the Online Mendelian Inheritance in Man (OMIM) [120] and the Mouse Genome Informatics (MGI) [121] database. The assignment of genes to clinical phenotypes, for which a relationship with hsa-miR-4513 or the seed polymorphism rs2168518 exists according to the literature, was done as follows: 1. Cancer: gene-phenotype relationship with a cancer subtype according to OMIM, or key words “cell proliferation” or “cell death” in MGI; 2. Cardiovascular phenotypes: mouse phenotype affecting the “cardiovascular system” in MGI; 3. AMD: mouse phenotype affecting “vision/eye” in MGI; 4. Diabetes: key words “cellular glucose” or “insulin resistance” in MGI; 5. Metabolic products in urine: mouse phenotype affecting “homeostasis/metabolism” and “renal/urinary system” in MGI; 6. Lipid traits: Gene Ontology (GO) function “lipid binding” according to MGI.

5 Results

5.1 Identification of circulating miRNAs in a mouse model of NV - Workflow

The first project of the present work aimed to detect functionally relevant miRNAs in AMD pathology, especially for the neovascular subtype. Although several studies screened for altered miRNA expression in AMD patients, results are highly variable and in parts even contradictory [56,76,85–89]. This might be attributed to different study designs or environmental circumstances by which epigenetic markers like miRNAs are potentially influenced. This emphasizes the need for alternative approaches to detect robustly dysregulated miRNAs in a pathological condition like NV. To this end, a mouse model of laser-induced NV, which represents a clinically relevant model system to study NV, was used to investigate the functional impact of miRNAs in AMD.

As miRNAs are intended to be used as potential biomarkers for AMD, expression differences were first analyzed from blood samples which are generally easily accessible. Further, as miRNA expression is highly influenced by environmental factors, the study design focused on reproducibility by including several independent replication steps (**Figure 8**). The initial discovery step was performed by NGS analysis comparing cmiRNA expression of laser-treated animals with their baseline expression before treatment. Afterwards, cmiRNAs were validated by comparing expression of the same laser-treated animals with untreated control animals. The remaining cmiRNAs were replicated in an independent experiment by qRT-PCR using two independent batches of laser-treated animals and comparison was performed with their baseline expression. Finally, expression of remaining miRNAs was analyzed by qRT-PCR in ocular tissue directly affected by the laser treatment, including retina and RPE/choroid.

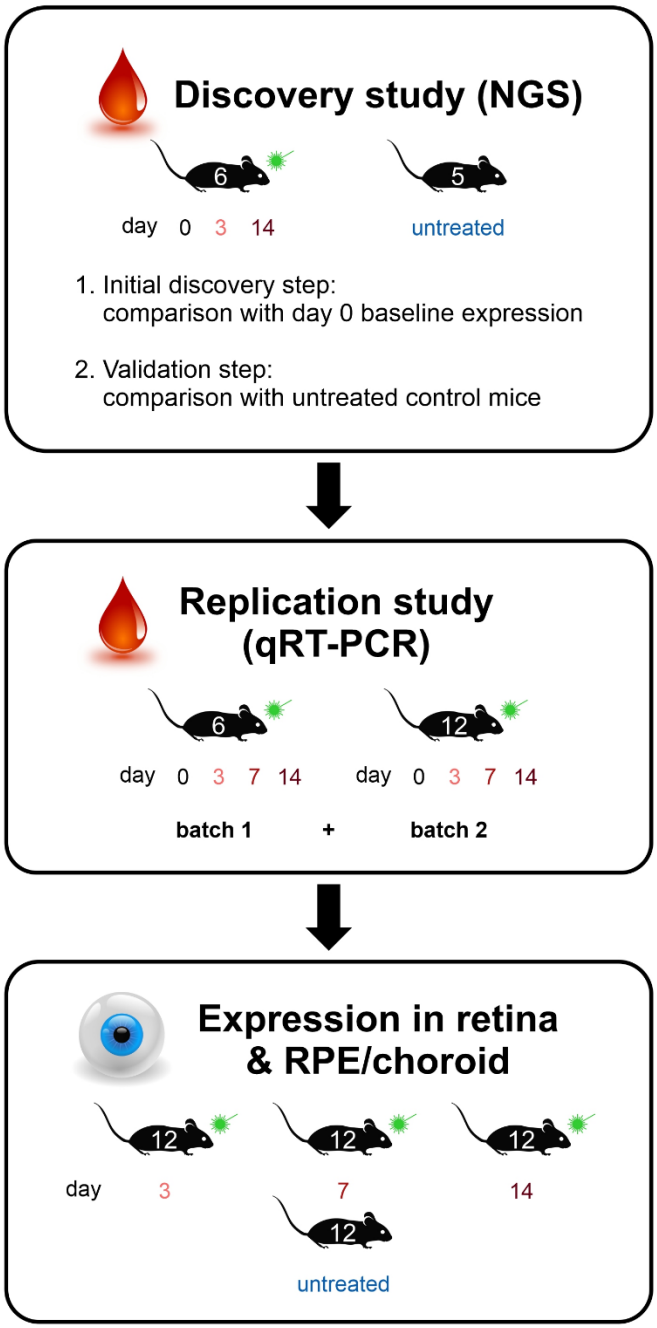

Figure 8. Workflow of the study design for identification of circulating miRNAs (cmiRNA) in a mouse model of laser-induced NV.

For the initial discovery study for identification of cmiRNAs in blood of mice with laser-induced NV by next generation sequencing (NGS) six mice were treated with an argon laser on day 1 and blood was drawn one day before treatment (day 0, baseline) and on day 3 and 14. Additionally, blood was drawn on the same time points from 5 untreated control animals. Expression of cmiRNAs of laser treated mice was first compared with the baseline expression on day 0 and cmiRNAs with an altered expression were validated by comparison with untreated control animals. Afterwards, an independent replication of altered cmiRNAs was performed by quantitative reverse transcription PCR (qRT-PCR). For this purpose, two independent batches of mice were treated, one included six and one 12 animals, and blood was drawn additionally on day 7. MiRNAs with a robustly altered expression in blood were further investigated in ocular tissue affected by NV, the retina and RPE/choroid. Therefore, miRNA expression from tissue of 12 mice per timepoint was compared with 12 untreated control animals.

The project was performed in cooperation with the Laboratory for Experimental Immunology of the Eye (Head Prof. Dr. Thomas Langmann, Department of Ophthalmology, Faculty of Medicine) at the University Hospital Cologne (Germany). Dr. Alexander Aslanidis, PD Dr. Marcus Karlstetter and Prof. Dr. Thomas Langmann performed laser treatment of female C57Bl/6J mice, drew blood from the animals and extracted ocular tissue. The materials were then sent to the Institute of Human Genetics in Regensburg for evaluation. Subsequently, first experiments were done by Patricia Berber and Dr. Felix Grassmann (both Institute of Human Genetic, University of Regensburg, Germany). This included isolation of cmiRNAs from blood

samples and from tissue samples from day 14, NGS library generation and data processing, as well as participation in the generation of qRT-PCR data.

5.1.1 Identification of altered cmiRNA expression by NGS

To detect cmiRNAs with an altered expression in a clinically relevant mouse model of NV, NGS analysis was performed with blood samples of six laser-treated mice from day 0 (baseline expression before treatment), 3 and 14, as well as five untreated animals. Overall, a stable cmiRNA expression profile between all investigated samples was observed (**Figure 9**). To detect cmiRNAs with an altered expression after laser-treatment, samples from day 3 and day 14 were compared with the baseline cmiRNA expression at day 0. CmiRNAs had to fulfill the following two criteria to be considered as a cmiRNA with an altered expression: (1) p-value < 0.05 (linear mixed effects model) and (2) absolute slope > 0.4. In total, 8 cmiRNAs were identified for day 3 and seven cmiRNAs for day 14 (**Supplementary Table 3**). One cmiRNA, namely mmu-miR-148b-5p, was detected in both comparisons.

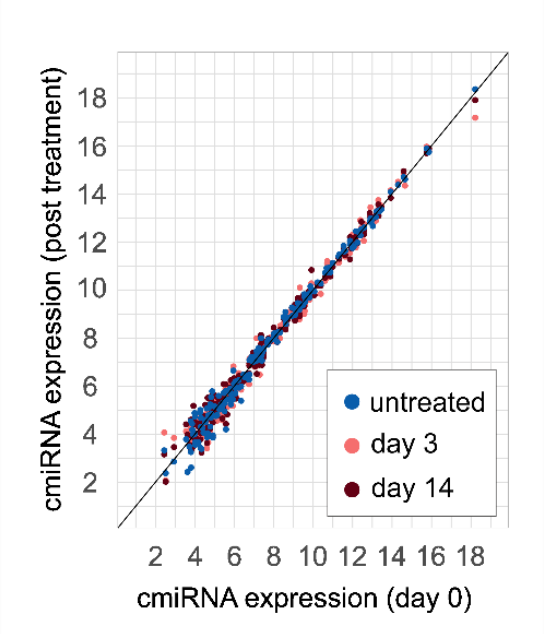

Figure 9. Comparison of cmiRNA profiles in NGS data. CmiRNA profiles, consisting of 180 different cmiRNAs, from blood of six laser-treated mice drawn on day 0 (before treatment, baseline), 3 and 14, as well as five untreated control mice (age matched with day 14 samples) were generated by NGS. Overall, cmiRNA expression after laser treatment was stable (Figure modified from Kiel et al., 2020 [91]).

CmiRNAs identified in the first comparison to the baseline expression of day 0 were further compared to untreated control samples with the assumption, that baseline cmiRNA expression on day 0 and untreated animals are comparable. To check this assumption for validity, candidate cmiRNAs were first tested for differential expression between day 0 samples and untreated mice with the same criteria as above (p-value < 0.05, absolute effect size > 0.4). CmiRNA mmu-miR-326-3p reached statistical significance in this analysis (Firth's bias-reduced logistic regression model, p-value = 0.047) and was therefore excluded from further analysis.

The expression of the remaining 13 cmiRNAs was tested in comparison with untreated control samples. Candidates were kept for further analysis, if they replicated the slope direction of the day 0 comparison and showed an absolute slope > 0.2 (linear fixed effects model) (**Figure 10, Supplementary Table 3**). In total, nine cmiRNAs fulfilled those criteria, namely mmu-miR-148b-5p, mmu-miR-18a-3p, mmu-miR-20a-5p, mmu-miR-298-5p, mmu-miR-449a-5p, mmu-miR-486a-5p, mmu-miR-92a-3p, mmu-let7i-3p, and mmu-miR-155-5p.

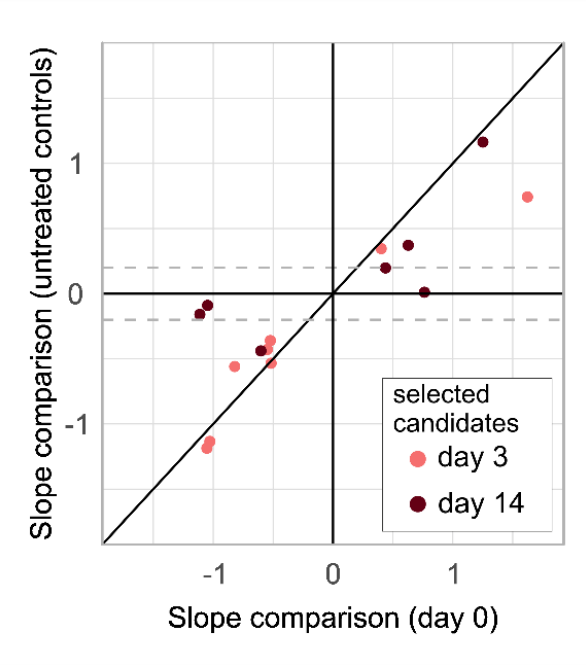

Figure 10. Comparison of slopes from differential expression models of day 3 and 14 samples compared with day 0 baseline controls and untreated control samples.
On the x-axis, slopes from comparison of day 3 and 14 samples with day 0 (baseline) samples are shown. The slope of the respective cmiRNA is displayed on the y-axis when compared with the untreated control samples. The dotted lines represent the slope threshold of an absolute slope > 0.2. Candidates in between the dotted lines were excluded from further analysis (Figure modified from Kiel et al., 2020 [91]).

5.1.2 Replication of cmiRNAs by qRT-PCR

The nine cmiRNAs with a consistently altered expression in the NGS analysis were replicated by qRT-PCR in two independent batches of animals, consisting of six and twelve laser-treated mice. Blood was drawn on day 0 as baseline control and on day 3, 7 and 14. By extending the timepoints examined by day 7 a more accurate cmiRNA expression profile over time could be established. Out of the nine investigated cmiRNAs, seven displayed effect directions identical to the initial NGS analysis, excluding mmu-miR-20a-5p and mmu-let-7i-3p (**Supplementary Table 4**). Three of the seven replicated cmiRNAs displayed significant expression differences in comparison to day 0 at one or more time points after laser treatment (linear mixed effects model, p-value < 0.05), namely mmu-miR-486a-5p (day 0 vs day 3 p-value = 0.003, day 0 vs day 7 p-value = 0.005), mmu-miR-92a-3p (day 0 vs day 3 p-value = 0.032) and mmu-miR-155-5p (day 0 vs day 14 p-value = 0.023) (**Figure 11**).

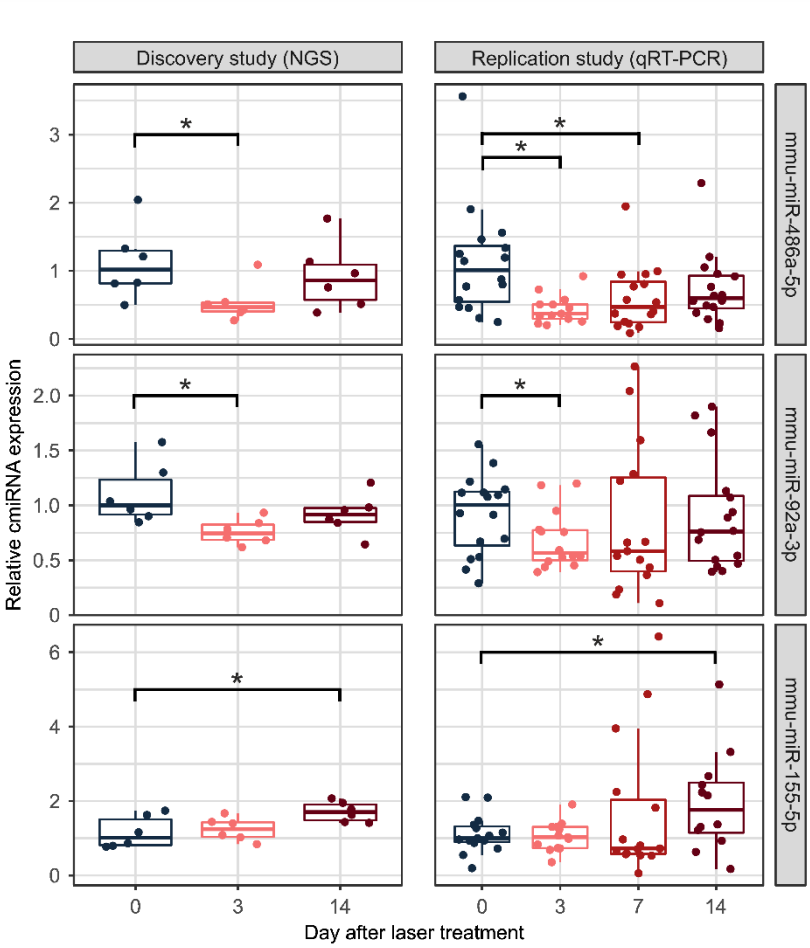

Figure 11. Validated cmiRNAs with a significant change in expression after laser-treatment in the qRT-PCR replication study. Relative expression of cmiRNAs with a significantly altered expression on day 3, 7 or 14 after laser-treatment in the discovery study conducted by NGS (n = 6) and the independent replication study by qRT-PCR (n = 18). Shown are relative expression values normalized to the median expression on day 0. * p-value of linear regression model < 0.05 (Figure modified from Kiel et al., 2020 [91]).

Mmu-miR-155-5p was excluded from further analysis due to high expression fluctuations and a small effect size in the linear regression model (slope [95 % Confidence interval, CI] = 0.059 [0.012 – 0.106]).

5.1.3 miRNA Expression in retinal and RPE/choroidal tissue

The expression of the remaining two robustly dysregulated cmiRNAs, mmu-miR-486a-5p and mmu-miR-92a-3p, was further analyzed in ocular tissue to investigate their expression in tissues affected by laser treatment and possibly in disease pathology. For this purpose, expression of mmu-miR-486a-5p and mmu-miR-92a-3p was analyzed in retina and RPE/choroid of 12 laser-treated mice per time point in comparison to untreated control mice *via* qRT-PCR.

In retinal tissue, none of the two miRNAs displayed significant differences in expression between the time points investigated (**Figure 12, Supplementary Table 5**). In contrast, both miRNAs displayed a significant upregulation in RPE/choroidal tissue after laser treatment on at least two time points in comparison to untreated controls (linear regression model followed by FDR correction, q-value < 0.05). The highest upregulation of mmu-miR-486a-5p was observed on day 3 (slope [95 % CI] = 0.408 [0.188–0.628]). The other miRNA, mmu-miR-92a-

3p displayed a steadily increasing expression over time after laser treatment (slope on day 14 [95 % CI] = 0.466 [0.084–0.848]).

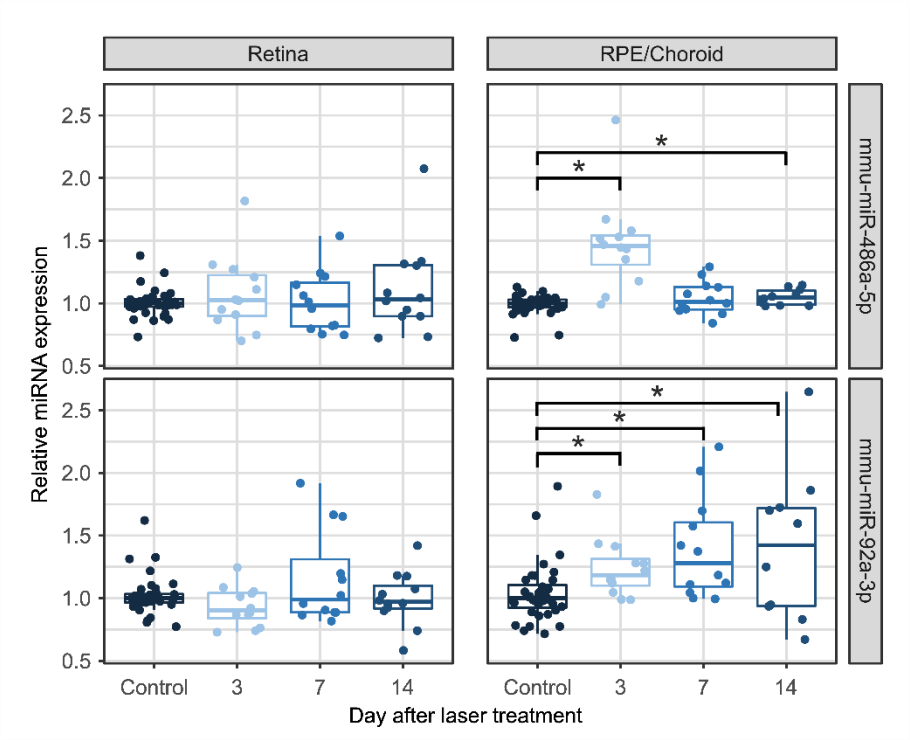

Figure 12. Relative expression of two miRNAs identified in blood of laser-treated mice in ocular tissue. Relative expression of mmu-miR-486a-5p and mmu-miR-92a-3p, both identified as dysregulated cmiRNAs in blood of mice with laser-induced NV, in retina and RPE/choroid. Shown is the relative expression normalized to the median of untreated control mice. Twelve mice were analyzed per timepoint after laser treatment and in total 24 control animals were investigated. Statistical significance was determined by a linear regression model followed by false discovery rate (FDR) correction. * q-value < 0.05 (Figure modified from Kiel et al., 2020 [91]).

Overall, mmu-miR-486a-5p and mmu-miR-92a-3p represent robustly dysregulated cmiRNAs in a laser-induced mouse model of NV. While both miRNAs did not show expression differences in the retina after laser induction, both were significantly upregulated in RPE/choroid.

5.2 Pleiotropic effects of AMD-associated genes

The second project aimed to characterize AMD-associated genes recently identified in a TWAS [83] in light of potential pleiotropy. A TWAS approach combines gene expression and genotype data to predict the influence of multiple genetic variants on gene expression. TWAS can therefore be applied to identify disease-associated genes. In the case of AMD, this approach revealed 106 disease-associated genes [83]. Investigating those genes for pleiotropic effects might highlight shared biological mechanisms between different complex diseases, which can help to further elucidate AMD disease pathology.

To assess a potential pleiotropic effect of the 106 AMD-associated genes, a collection of GWAS results was generated. This collection was built on previous work including GWAS data

of 60 different phenotypes [41] and was expanded to 82 complex traits and diseases, including AMD, which can be categorized into 12 phenotype groups (**Table 40**, detailed information are given in **Supplementary Table 1**). GWAS lead variants were used to define GWAS loci ($R^2 > 0.5$). In case genomic positions of different GWAS loci overlapped, these loci were merged. Afterwards, AMD-associated genes were screened to assess whether they physically overlap with GWAS loci (**Figure 13**).

Table 40. Overview of phenotype groups.

Phenotype group	Number of phenotypes	Number of GWAS
Aging	1	1
Anthropometric traits	4	4
Autoimmune diseases	10	15
Blood cell traits	9	2
Cancer	12	30
Cardiovascular phenotypes	5	3
Eye phenotypes	6	5
Immune-related phenotypes	3	2
Lifestyle	2	2
Metabolic phenotypes	19	13
Neurological diseases	5	6
Organ function traits	5	7

AMD was excluded from the phenotype grouping. GWAS = genome-wide association study.

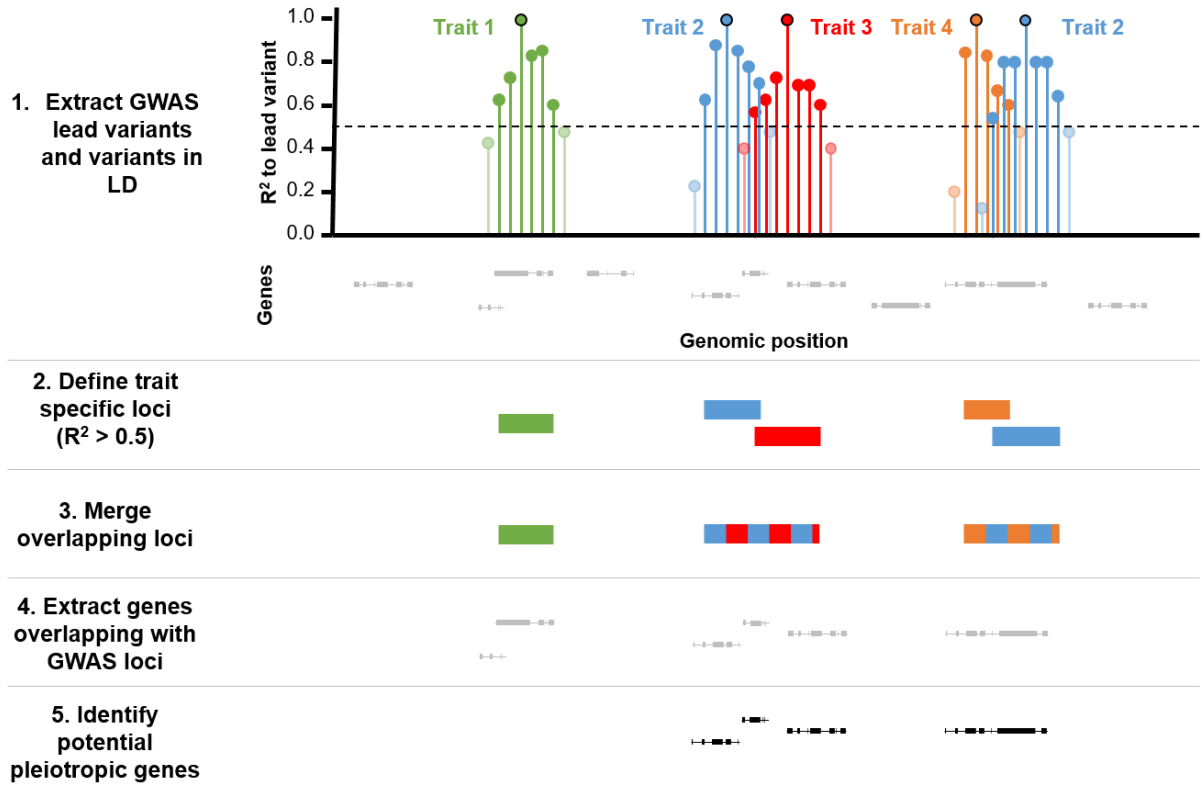

Figure 13. Study design to identify pleiotropic effects of AMD-associated genes.
GWAS lead variants and variants in LD ($R^2 > 0.5$) of 82 phenotypes were used to define GWAS loci. Physically overlapping GWAS loci were merged. Afterwards, genes associated with AMD were screened whether they overlap these loci. Only genes overlapping loci associated with more than one phenotype were regarded as pleiotropic (Figure adopted from Strunz et al., 2020 [83]).

Overall, 50 out of 106 AMD-associated genes overlapped generally with a GWAS locus of the 82 phenotypes investigated (**Figure 14**), including 38 genes located in a previously described AMD locus. This relatively small number of genes in AMD loci is attributed to the fact, that a TWAS approach is independent of the initial GWAS loci reported.

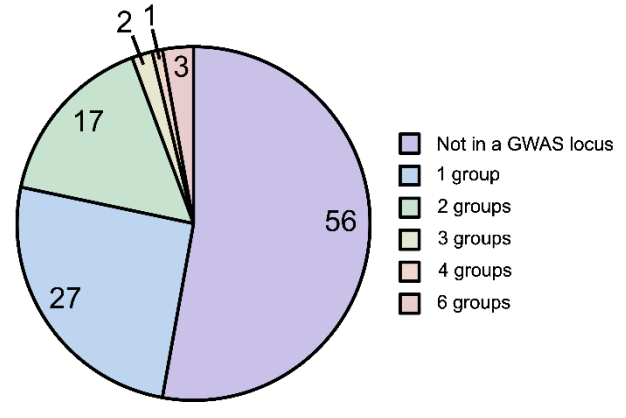

Figure 14. AMD-associated genes overlapping with GWAS loci.
106 AMD-associated genes were screened for a physical overlap with loci identified in GWAS of 82 phenotypes corresponding to 12 phenotype groups. Shown are the number of genes which overlapped with GWAS loci of those phenotype groups (Figure modified from Strunz et al., 2020 [83]).

Next to AMD, the second most phenotype group represented in this analysis, is the neurological disease group (15 genes in the respective GWAS loci), followed by metabolic phenotypes (10 genes) and autoimmune diseases (9 genes) (**Figure 15**). The enrichment of AMD-associated genes in GWAS loci of AMD, neurological diseases, metabolic phenotypes, autoimmune diseases and organ function traits is statistically significant when compared with all predictable genes in the TWAS approach (in total 24,388 genes, Fisher's exact test, p-value < 0.05).

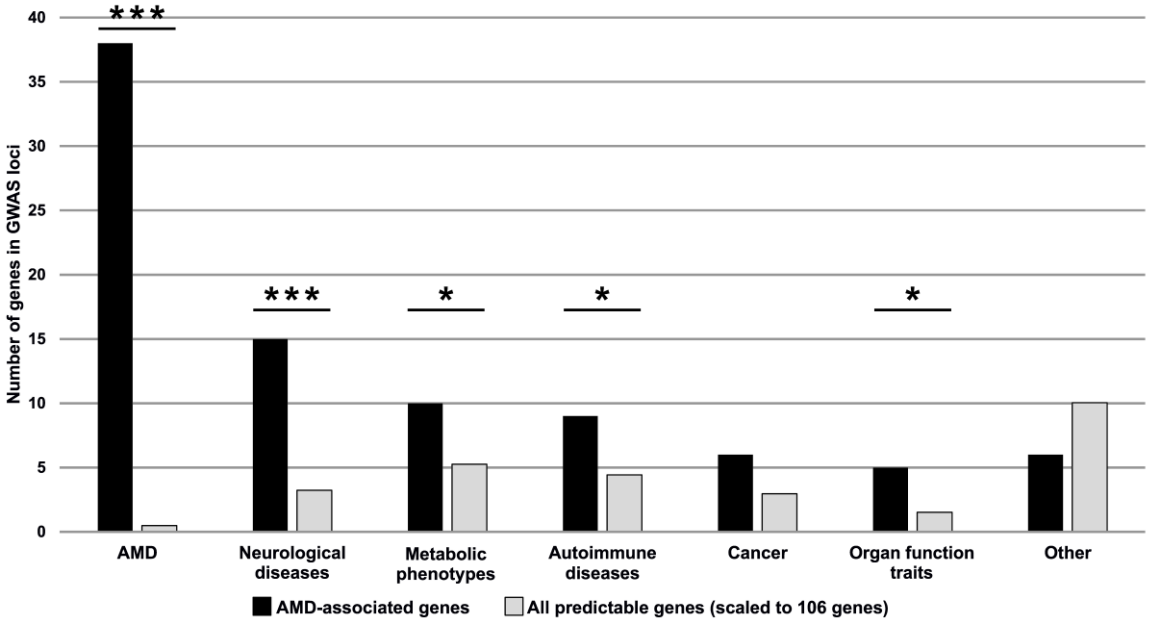

Figure 15. Overlap of AMD-associated genes with GWAS loci of different phenotype groups.
Enrichment of AMD-associated genes (black) in GWAS loci of different phenotype groups was compared to all predictable genes in the transcriptome-wide association study (TWAS) approach (in total 24,388 genes) scaled down to 106 genes for a better comparability. The group "Other" includes the phenotype groups "Aging", "Anthropometric traits", "Blood cell traits", "Cardiovascular phenotypes", "Eye phenotypes", "Lifestyle" and "Immune-related traits". Significance was assessed with a Fisher's exact test. * p-value < 0.05, ** p-value < 0.01, *** p-value < 0.001 (Figure modified from Strunz et al., 2020 [83]).

To identify pleiotropic genes, genes overlapping with GWAS loci of phenotypes belonging to different groups were considered. This stringent filter was applied as many phenotype groups include closely related sub-phenotypes, like levels of low-density lipoprotein (LDL) and high-density lipoprotein (HDL), which could lead to a high number of repetitive results. Twenty-seven of the 50 genes overlapping with GWAS loci, intersected with loci corresponding to one phenotype group. The remaining 23 genes overlapped with GWAS loci of different groups and are therefore potentially pleiotropic (**Table 41**).

Table 41. AMD-associated genes overlapping with GWAS loci of more than one phenotype group (Table modified from Strunz et al., 2020 [83])**.**

Gene	Locus R^2 [hg19]	Phenotype groups in locus	Single phenotypes in locus
OL4A3	chr2:228083236-228100488; chr2:228126494-228231432	AMD; Eye phenotypes	AMD; CCT
PMS2P1 *STAG3L5P* *PILRB* *PILRA* *ZCWPW1* *TSC22D4* *NYAP1*	chr7:99894971-100111776	Neurological diseases; AMD	AD; AMD
RP11.325F22.2	chr7:104581402-105063372	AMD; Neurological diseases	AMD; SCZ
PLEKHA1 *ARMS2* *HTRA1*	chr10:124124669-124235355	Neurological diseases; AMD	MIG; AMD
RDH5	chr12:56115585-56213297	AMD; Eye phenotypes	AMD; MYP
RIN3	chr14:93068516-93118229	Cancer; Organ function traits	BRC; BRConly; FEV1; LGF
ALDH1A2	chr15:58671721-58692118; chr15:58718529-58742418	Blood cell traits; Metabolic phenotypes; AMD	HB; RBC; HDL; TC; TG; AMD
ULK3	chr15:75031521-75449869	Cardiovascular phenotypes; Autoimmune diseases; Blood cell traits	DBP; GBP; HTN; SBP; SLE; MCV; RBC
CETP	chr16:56985514-57006829	AMD; Metabolic phenotypes	AMD; HDL; LDL; TC; TG
BCAR1 *CFDP1* *TMEM170A*	chr16:75233867-75516739	Organ function traits; Cancer; Neurological diseases; Autoimmune diseases; Metabolic phenotypes; AMD	FEV1FVC; LGF; PanC; MIG; T1D; T2D; AMD

FUT2 *MAMSTR*	chr19:49158532-49252574	Metabolic phenotypes; Autoimmune diseases	ALP; LEP; TC; CD; IBD; GGT
BAIAP2L2	chr22:38295271-38503972; chr22:38505356-38614129	AMD; Anthropometric traits; Metabolic phenotypes; Cancer	AMD; BFP; TG; CMM

AD = Alzheimer's disease; ALP = alkaline phosphatase; AMD = Age-related macular degeneration; BFP = Body fat percentage; BRC = Breast cancer – maximal effect size of different types of breast cancer; BRConly = Breast cancer - only BRC; CCT = Central corneal thickness; CD = Crohn's disease; CMM = Cutaneous malignant melanoma; CSCC = Cutaneous squamous cell carcinoma; DBP = Diastolic blood pressure; FEV1 = forced expiratory volume in 1 second; FEV1FVC = forced expiratory volume in 1 second/forced vital capacity; GBP = General blood pressure; GGT = γ -glutamyl transferase; HB = Hemoglobin; HDL = High-density lipoprotein; HTN = Hypertension; IBD = Inflammatory bowel disease; LDL = Low-density lipoprotein; LEP = Liver enzymes in plasma; LGF = Lung function; MCV = Mean cell volume; MIG = Migraine; MYP = Myopia; PanC = Pancreatic cancer; RBC = Red blood cell phenotypes; SBP = Systolic blood pressure; SCZ = Schizophrenia; SLE = Systemic lupus erythematosus; T1D = Type 1 diabetes; T2D = Type 2 diabetes; TC = Total cholesterol; TG = Triglycerides.

Approximately one quarter of the AMD-associated genes identified through a recent TWAS are likely pleiotropic genes, which highlight shared biological mechanisms between AMD and neurological diseases, metabolic phenotypes and autoimmune diseases. Altogether, 19 out of 23 putatively pleiotropic AMD-associated genes overlap with known AMD loci, while 4 genes do not, namely *RIN3*, *ULK3*, *FUT2* and *MAMSTR*. However, the analysis conducted did not allow any further conclusions whether there is true pleiotropy or just a random physical overlap of the GWAS loci with the AMD associated genes. One locus of an AMD-associated gene that is not located in a previously reported AMD locus according to the latest AMD GWAS from 2016 [20], namely *ULK3* located at 15q24.1, was selected for a closer examination.

5.3 Characterization of the AMD-associated pleiotropic locus at 15q24.1

Following, an exemplary locus harboring an AMD-associated gene, namely *ULK3* at 15q24.1, was further investigated to elucidate the underlying biological mechanism. Even though this locus has not yet been associated with AMD at genome-wide significance in a classical GWAS [20], a recent meta-analysis applying a multivariate GWAS model introduced as multiple trait analysis of GWAS (MTAG) [122] highlighted a genome-wide association of a genetic variant in this locus (rs1378940) with AMD [123]. Furthermore, a proxy of this variant (rs2168518, R^2 = 1 in European individuals) has gained some interest in AMD research due to its location in the seed region of a miRNA (hsa-miR-4513), which could have a possible effect on the

regulatory function of this miRNA [124]. Variant rs2168518 has not yet been associated with AMD at the level of genome-wide significance (p-value = 3.3 x 10^{-06}) [124] and the MTAG approach was based on dependent datasets, which may be critical. Therefore, the genetic association of 15q24.1 with AMD was investigated including rs2168518 as a representative variant of this locus.

At first, the association of rs2168518 with AMD was separately investigated in two independent datasets, namely the dataset of the latest AMD GWAS performed by the IAMDGC [20] and the GERA cohort, a study cohort from the Kaiser Permanente Research Program [108]. Overall, a nominal association of rs2168518 with AMD in the GERA dataset (logistic regression model, p-value = 3.88 x 10^{-03}, n = 29,180) and the IAMDGC dataset (p-value = 3.05 x 10^{-06}, n = 33,976) was observed (**Figure 16**). A meta-analysis revealed a genome-wide significant association of rs2168518 with AMD (p-value = 4.52 x 10^{-08}, n = 63,156).

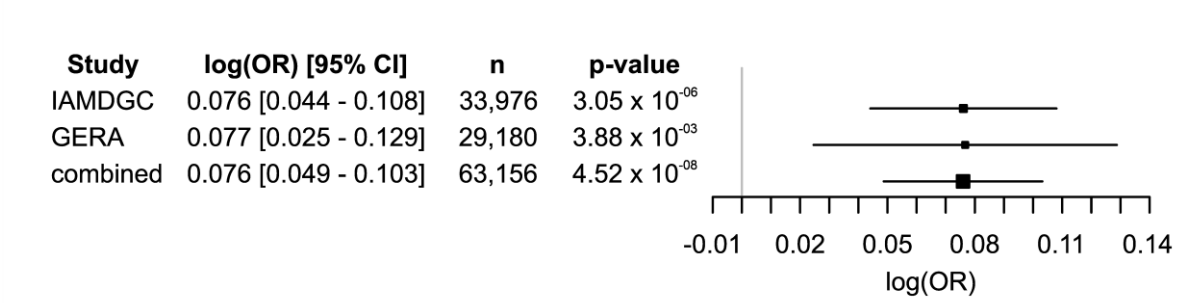

Figure 16. Genome-wide association of rs2168518 with AMD.

The association of rs2168518 with AMD was calculated separately in the IAMDGC and Genetic Epidemiology Research on Adult Health and Aging (GERA) dataset. In both datasets rs2168518 displayed a nominal association with AMD. A logistic regression model based on the combined dataset revealed an association of rs2168518 with AMD at the level of genome-wide significance (p-value < 5 x 10^{-08}). For all associations, the A allele of rs2168518 indicated the effect allele. OR = odds ratio, CI = confidence intervals, n = sample size (Figure modified from Kiel et al., 2020 [125]).

5.3.1 Refinement of the genetic association signal of rs2168518 with AMD

A genome-wide association provides evidence about a likely contribution of a genetic variant to disease, but does not reveal any causalities underlying its association. It could be advantageous to investigate associations with specific AMD subtypes, which may give indications of disease mechanisms and therefore could help to elucidate the function behind an association signal. For this purpose, the IAMDGC dataset is well suited, as it contains detailed information about AMD subtypes, in contrast to the GERA dataset.

The association of rs2168518 was calculated with five different subtypes of AMD, including the overall late stage form, GA, NV, the combined manifestation of GA and NV and also early stage AMD. The genetic variant rs2168518 was associated with three of these manifestations,

namely late stage AMD, GA as well as NV (logistic regression model, FDR corrected, q-value < 0.05) (**Table 42**). Remarkably, the association of rs2168518 with NV (q-value = 1.87 x 10^{-05}) is clearly stronger than with GA (q-value = 0.024). It should be noted, that for the combined manifestation of GA and NV the statistical power to detect an association might be insufficient, as the subgroup was relatively small with only 2,160 individuals affected by combined GA and NV.

Table 42. Association of rs2168518 with AMD subtypes in the IAMDGC dataset (Table modified from Kiel et al., 2020 [125]).

	n	OR [95% CI]	p-value	q-value
Late stage AMD	33,976	1.089 [1.052 - 1.127]	8.74 x 10^{-07}	4.00 x 10^{-06}
Geographic atrophy (GA)	21,067	1.077 [1.016 - 1.142]	0.013	0.024
Neovascular AMD (NV)	28,581	1.091 [1.050 - 1.133]	8.29 x 10^{-06}	1.87 x 10^{-05}
GA & NV	19,992	1.073 [1.001 - 1.150]	0.048	0.054
Early stage AMD	24,489	1.036 [0.992 - 1.081]	0.112	0.112
< 75 years	17,326	1.121 [1.066 - 1.177]	7.41 x 10^{-06}	1.87 x 10^{-05}
> 75 years	15,825	1.055 [1.005 - 1.108]	0.030	0.039
Male	14,352	1.139 [1.081 - 1.200]	8.89 x 10^{-07}	4.00 x 10^{-06}
Female	19,624	1.053 [1.007 - 1.102]	0.025	0.038

For all associations the A allele indicates the effect allele. Associations were calculated in comparison with the respective non-AMD individuals. OR = odds ratio, CI = confidence intervals, n = sample size.

In addition, the association of rs2168518 with late stage AMD was calculated separately for individuals younger and older than 75 years of age. Thereby, an association of rs2168518 with late stage AMD in individuals younger than 75 years of age became apparent (q-value = 1.87 x 10^{-05}), while there was only a weak association in individuals over the age of 75 (q-value = 0.039).

Further, the association of rs2168518 with late stage AMD was analyzed regarding gender specificity. Interestingly, a strong association of rs2168518 with AMD was detected in male individuals (q-value = 4.00 x 10^{-06}), but only a weak association was detected in females (q-value = 0.038) (**Figure 17**). A gender-specific association of rs2168518 with AMD is supported by the fact, that the sample size in the female group of the IAMDGC dataset was larger (n AMD cases = 9,612, n controls = 10,012) in comparison to the male sample sizes (n AMD cases = 6,532, n controls = 7,820).

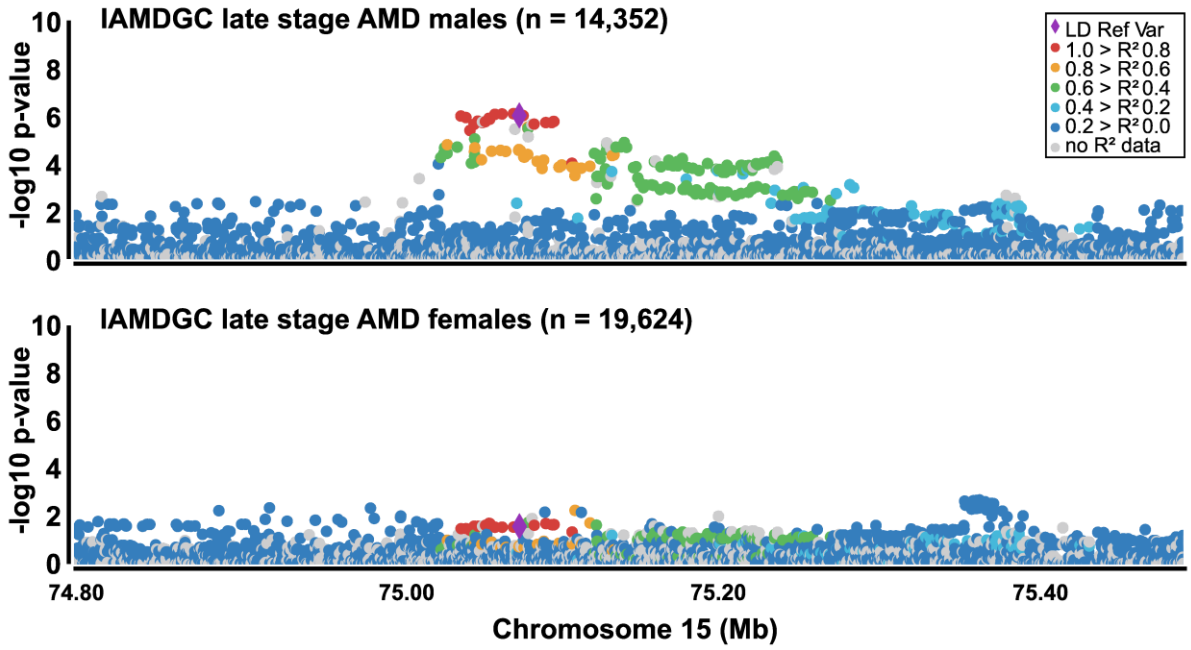

Figure 17. Association of rs2168518 with AMD in male and female individuals.

The IAMDGC dataset was divided by gender and the association of rs2168518 with AMD was determined separately. In male individuals an association signal was evident, while there was no association signal detectable in female individuals. Rs2168518 is presented as purple diamond and serves as LD reference variant. Plots were created with LocusZoom [21]. n = sample size (Figure modified from Kiel et al., 2020 [125]).

Finally, a conditional analysis was performed to clarify whether the association signal with AMD at 15q24.1 consists of one or more independent signals. After adjustment for the genetic variant with the smallest p-value in the initial analysis, no further variants were significantly associated with AMD (**Figure 18**), suggesting that the association with AMD at this locus ascribed exclusively to a single genetic signal.

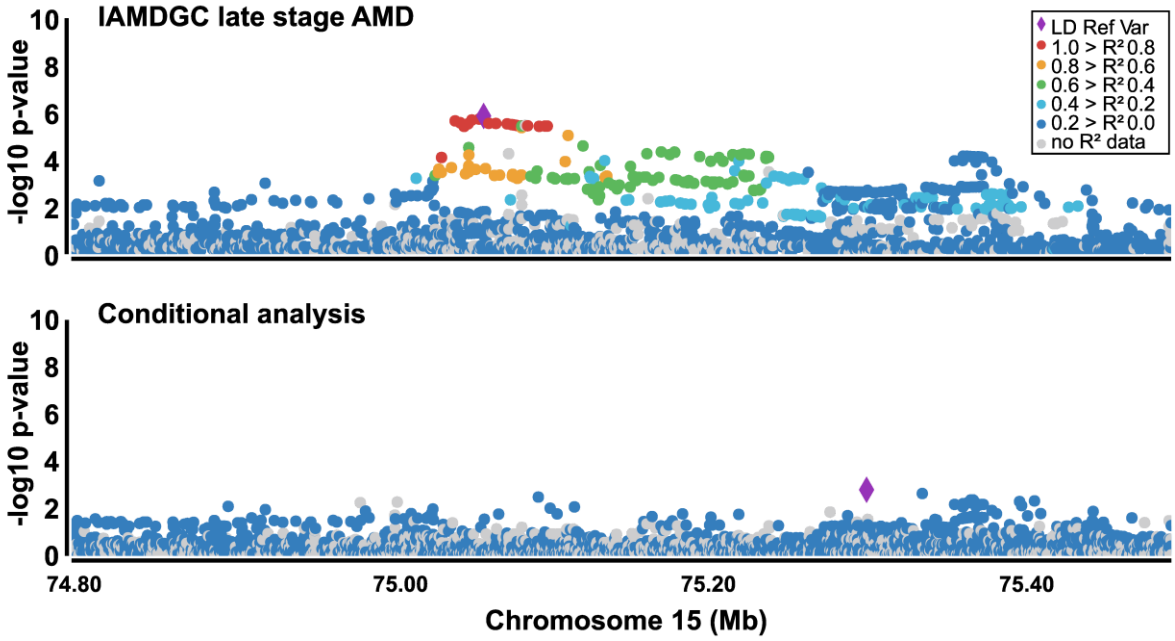

Figure 18. Conditional analysis to dissolve the association signal at 15q24.1.

The association signals at 15q24.1 with AMD in the IAMDGC dataset are displayed before (upper plot) and after adjustment (lower plot) for the variants with the smallest p-value. In the upper plot rs2168518 is presented as purple diamond and served as LD reference variant. In the lower plot, the genetic variant with the smallest remaining p-value presents the LD reference variant and is presented as purple diamond. Plots were created with LocusZoom [21] (Figure modified from Kiel et al., 2020 [125]).

Overall, rs2168518 revealed a NV-related and gender-specific association with AMD, mostly in individuals under the age of 75 years. Further, the association with AMD can be ascribed to a single genetic association signal at the 15q24.1 locus.

5.3.2 Pleiotropic effect of 15q24.1 assessed in the UK Biobank data

Analyses of pleiotropic AMD-associated genes detected *ULK3* in 15q24.1 to physically overlap with GWAS loci of cardiovascular phenotypes [126], autoimmune diseases [127] and blood cell phenotypes [128]. Further, studies performed for the miRNA seed polymorphism rs2168518 in 15q24.1 also reported associations with cardiovascular phenotypes [129–131], fasting glucose and lipid traits [129]. To dissolve the pleiotropic effect of 15q24.1, data from the UK Biobank [132] cohort were analyzed by applying the PheWeb browser tool [113]. This online tool contains GWAS results of over 2,000 phenotypes in the UK Biobank dataset. An exploratory threshold for significance of p-value < 1×10^{-04} revealed 15 significant associations of rs2168518 with different phenotypes (**Figure 19**, **Supplementary Table 6**). Eight of those 15 associations reached genome-wide significance (p-value < 5×10^{-08}), including seven phenotypes related to blood pressure. In contrast, the phenotype code representing AMD in

the UK Biobank data, “Eye problems/disorders: Macular degeneration”, failed to reach significance. This may be attributable to the relatively low sample size of AMD patients with approximately 5,000 self-reported cases in the UK Biobank dataset [117].

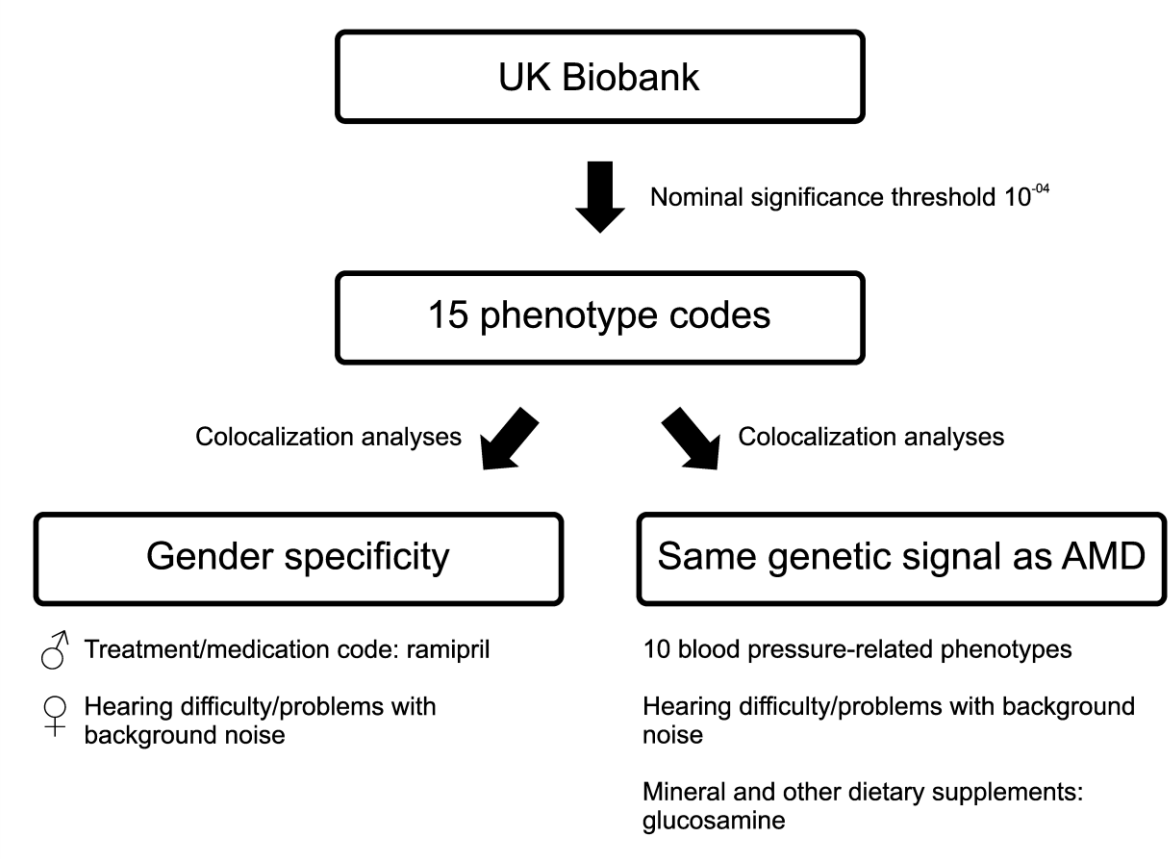

Figure 19. Schematic summary of pleiotropy analyses of rs2168518 in the UK Biobank data.
To identify phenotypes associated with rs2168518 at a level of nominal significance (p-value < 1 x 10^{-04}), the PheWeb browser [113] containing GWAS summary statistics of the UK Biobank data [132] was searched. In total, fifteen phenotype codes reached the significance threshold and were therefore regarded to be associated with rs2168518. To study gender specificity and a colocalization with the AMD association signal in the IAMDGC dataset [20], publicly available GWAS summary statistics of the UK Biobank data [112] were used. Gender specificity was determined by colocalization analysis comparing summary statistics of GWAS performed for the same phenotype separately for males and females. Gender specificity was defined by a probability of > 0.8 in one gender. To study if the association signals correspond to the same genetic signal as the AMD association signal in the IAMDGC dataset [20], a colocalization analysis was performed. The colocalization analysis was performed for UK Biobank GWAS data of both sexes, as well as females and males separately, and was always compared to IAMDGC data of both sexes. A phenotype was regarded to correspond to the same genetic signal as AMD, in case at least one gender analysis reached the colocalization probability threshold of > 0.8. Detailed information is available in **Supplementary Table 6**.

To gain a deeper insight into the association results, the 15 phenotypes associated with rs2168518 in the UK Biobank data were grouped manually into related groups. Further, gender

specificity and colocalization with the AMD association signal was examined, the latter by comparing UK Biobank GWAS summary statistics [112] with the IAMDGC data [20].

The first group of phenotypes associated with rs2168518 is represented by blood pressure phenotypes. Ten of the 15 significant association results are categorized to blood pressure traits, including seven phenotypes reaching genome-wide significance (p-value < 5×10^{-08}). Remarkably, the AMD risk increasing allele "rs2168518:A" displayed a consistent protective effect on high blood pressure measurements, including direct measurements of diastolic blood pressure (DBP), systolic blood pressure (SBP) and hypertension, but also on indirect hypertension measurements like treatment with Ramipril (ACE inhibitor; therapy for arterial hypertension, heart failure, and prophylaxis of cardiological conditions) or Bendroflumethiazide (thiazide diuretic; treatment of arterial hypertension, heart failure, and edema). Moreover, GWAS focused on control individuals, including "Vascular/heart problems diagnosed by doctor: None of the above" and "Medication for cholesterol, blood pressure or diabetes: None of the above" showed adverse effect sizes for the same allele as expected and therefore represent internal controls.

Gender analysis revealed a gender-specific association signal for rs2168518 with Ramipril treatment, which was exclusively detected in male individuals (p-value = 4.03×10^{-08}), while there was no significant association in females (p-value = 0.103). This result was confirmed by a colocalization analysis, which determines whether association signals of two traits (or in this case two sexes) correspond to the same underlying genetic signal by comparing GWAS summary statistics. This analysis revealed a coloc probability of 0.853 for a signal in male GWAS summary statistics only. None of the other blood pressure traits revealed gender-specific association with rs2168518.

Interestingly, the colocalization analysis of the association signal at rs2168518 with blood pressure traits in the UK Biobank data [112] and the AMD association signal in the IAMDGC data [20] revealed that the majority of association signals are identical genetic signals (coloc probabilities for the same signal > 0.8, **Figure 20**). Exceptions are DBP and SBP, for which only the association signal in females corresponds to the same genetic signal as AMD.

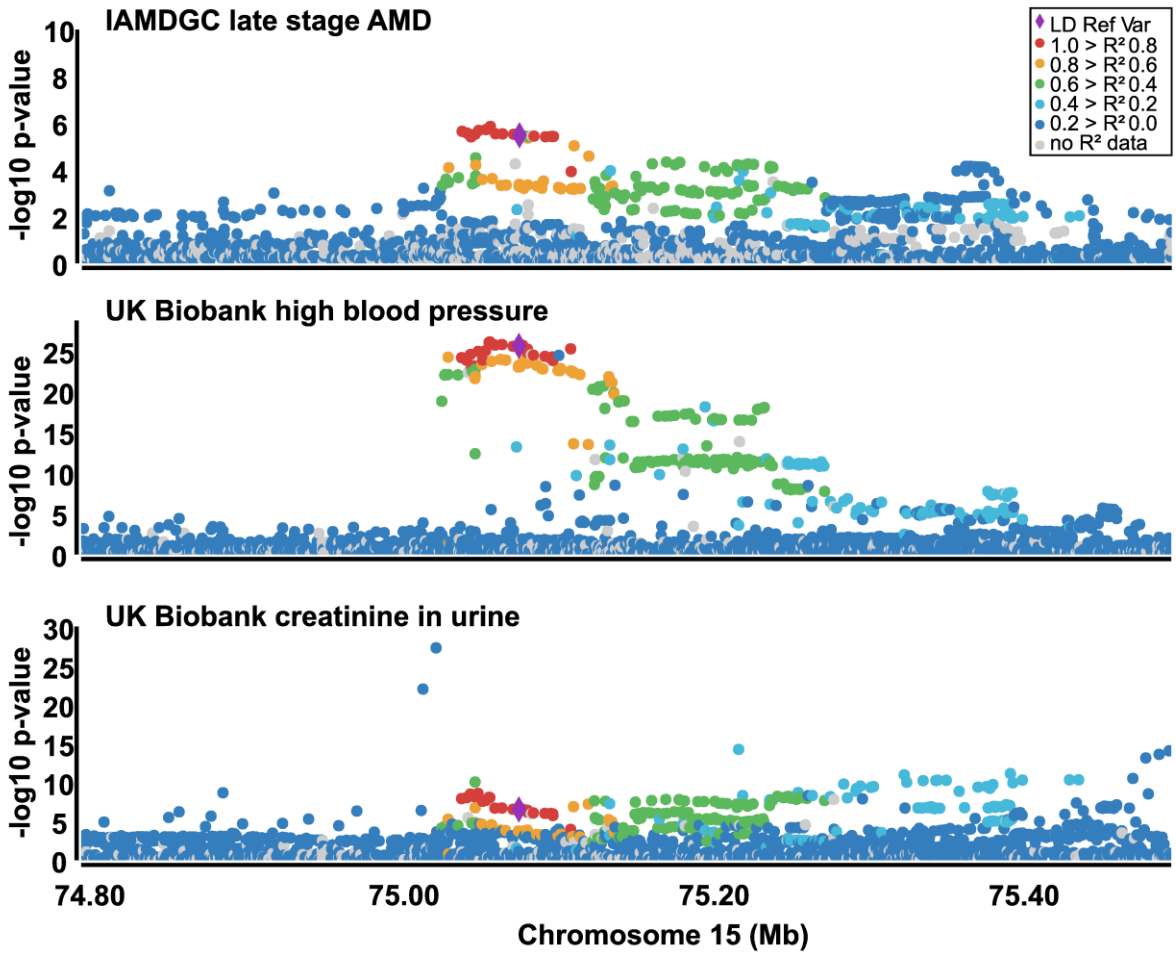

Figure 20. LocusZoom plots of association signals at 15q24.1.

Association signals of 15q24.1 with late stage AMD (IAMDGC data [20]), an exemplary blood pressure trait ("Vascular/heart problems diagnosed by doctor: High blood pressure", UK Biobank data [112]) and an exemplary phenotype of the metabolic product in urine group ("Creatinine (enzymatic) in urine", UK Biobank data [112]). The genetic association signal of blood pressure traits represents the same genetic association signal as for AMD (coloc probability = 0.976). In contrast, the association signal of creatinine in urine corresponds to a different genetic signal (coloc probability = 0.037). rs2168518 serves as LD reference variant and is shown as purple diamond. Plots were created with LocusZoom [21] (Figure modified from Kiel et al., 2020 [125]).

The second group of phenotypes associated with rs2168518 in the UK Biobank cohort are metabolic products in urine, including two phenotype codes, namely "Creatinine (enzymatic) in urine" and "Sodium in urine". While there is a genome-wide association of rs2168518 with creatinine in urine (p-value = 5.30×10^{-09}), there is only a nominal association with sodium in urine (p-value = 7.20×10^{-05}). The AMD risk allele "A" displayed a protective association against high levels of both metabolic products in urine. No gender-specific association was detectable. Comparing these association signals at 15q24.1 with the AMD association signal (IAMDGC dataset [20]) revealed that the association signals for metabolic products in urine correspond

to a different genetic signal than the AMD association signal (coloc probabilities for different signals > 0.8, **Figure 20**).

While the first two groups display logical entities, the last group of phenotype codes associated with rs2168518 in the UK Biobank cohort is composed of three individual effects, namely "Hearing difficulty/problems with background noise" (p-value = 4.10 x 10^{-06}), "Birth weight of first child" (p-value = 1.20 x 10^{-05}) and "Mineral and other dietary supplements: glucosamine" (p-value = 2.50 x 10^{-05}). Remarkably, the association signal with "Hearing difficulty/problems with background noise" showed a gender-specific association opposite to AMD, with a genome-wide significant association in females (p-value = 6.01 x 10^{-09}), while there is no association in male individuals (p-value = 0.345). The gender-specificity of the association signal is confirmed by the colocalization analysis, which revealed a coloc probability for a genetic association signal in females only of 0.886. Colocalization analysis with the AMD association signal revealed, that the association signals of "Hearing difficulty/problems with background noise" (both sexes and female only), as well as "Mineral and other dietary supplements: glucosamine" (both sexes) both colocalize with the genetic signal of AMD.

Overall, the analysis of pleiotropic effects of rs2168518 in data of the UK Biobank cohort revealed associations with several phenotypes, including blood pressure-related traits, metabolic products in urine, as well as several single effects with nominal significance. While the genetic association signals underlying blood pressure phenotypes correspond to the same genetic signal as for AMD, the genetic signals underlying the metabolic products in urine associations are independent from the AMD signal.

5.3.3 Investigation of genetic variants at 15q24.1 regarding alterations in transcription factor binding sites

So far, genetic association signals for 15q24.1 were determined and characterized, but no functional mechanisms behind those signals were investigated. One way to address this issue is to identify genetic variants located in TF binding sites, which may result in alterations of transcriptional regulation. For this purpose, genetic variants in high LD with rs2168518 (R^2 > 0.8 in Europeans, **Supplementary Table 2**) were screened for their impact on TF binding *via* RegulomeDB 2.0 [118,119]. Overall, RegulomeDB ranked 8 out of 27 variants to have a potential influence on TF binding or gene expression regulation. Two variants (rs1378942 and rs2470890) were predicted to influence the expression of *ULK3* in monocytes. The remaining six genetic variants were predicted to influence TF binding by matching DNase peaks and footprints, namely rs3784789 (binding site for TFs SPI1, ZSCAN4C), rs11632414 (MAFG, NFE2L1), rs12909307 (FOXD3, FOXP1, NANOG), rs11072507 (SOX9, SOX21, SOX30 and SRY), rs11636952 (ZFX), as well as rs1378941 (HENMT1, NHLH1, PLAG1 and ZNF524).

Remarkably, one genetic variant (rs11072507) was predicted to alter the binding of the TFs SRY, located on the Y chromosome, and SOX9, which is known to be regulated directly by SRY. Both TFs play an important role in sex determination [133]. In addition, another genetic variant (rs11636952) is predicted to alter a binding site for the TF ZFX, located on the X chromosome. Therefore, the three TFs ZFX, SRY and SOX9 may contribute to sex-specific transcriptional regulation mechanisms at 15q24.1, which in turn can lead to differences in association signals between genders (**Figure 21**). In addition to gender-specific regulation mediated through TFs at this locus, there is also an important post-transcriptional regulator located at 15q24.1, miRNA hsa-miR-4513. The effect of hsa-miR-4513 on gene expression was investigated in the final project of the present work.

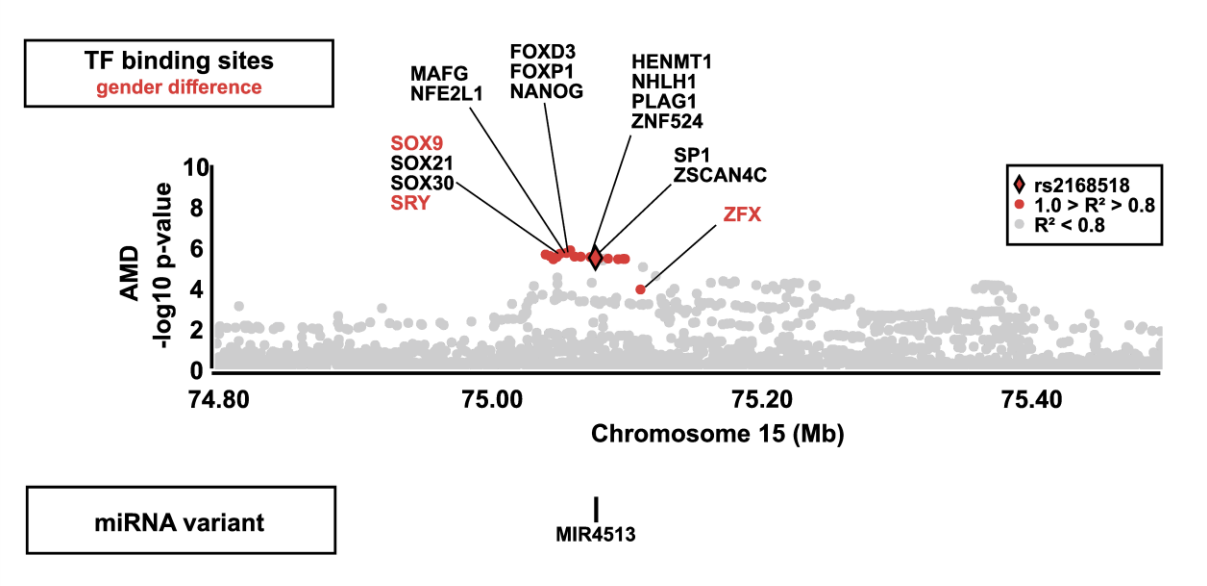

Figure 21. Schematic overview of altered transcription factor (TF) binding sites at 15q24.1.
Locus scheme of functional mechanisms within the AMD association signal at locus 15q24.1. The Manhattan plot shows association p-values with late stage AMD. Rs2168518 is represented as red diamond and all genetic variants in high LD with rs2168518 ($R^2 > 0.8$ in Europeans) are shown as red dots. TF binding sites potentially altered by those genetic variants are shown with regard to their approximate chromosomal position. TFs related to gender differences are highlighted in red. Relationship to gender differentiation was determined *via* chromosomal position with location on sex chromosomes (SRY and ZFX) or if TFs were directly regulated by TFs located on sex chromosomes (SOX9). Below the Manhattan plot hsa-miR-4513 is shown with regard to its chromosomal position, the miRNA harboring rs2168518 in its seed region. The raw version of the Manhattan plot was created with LocusZoom [21] (Figure modified from Kiel et al., 2020 [125]).

5.4 Influence of seed polymorphism rs2168518 in hsa-miR-4513 on post-transcriptional gene regulation

The last project as part of this thesis deals with the regulatory effect of hsa-miR-4513 located at 15q24.1 on gene expression, specifically investigating the impact of its AMD-associated

seed polymorphism rs2168518. For this purpose, RNA-Seq was performed followed by multiple validation approaches, including Western Blot analysis and luciferase reporter assay. Allele-specific target genes were further screened for their medical relevance in several phenotypes to identify valid candidates, which might be underlying different phenotype association signals (**Figure 22**).

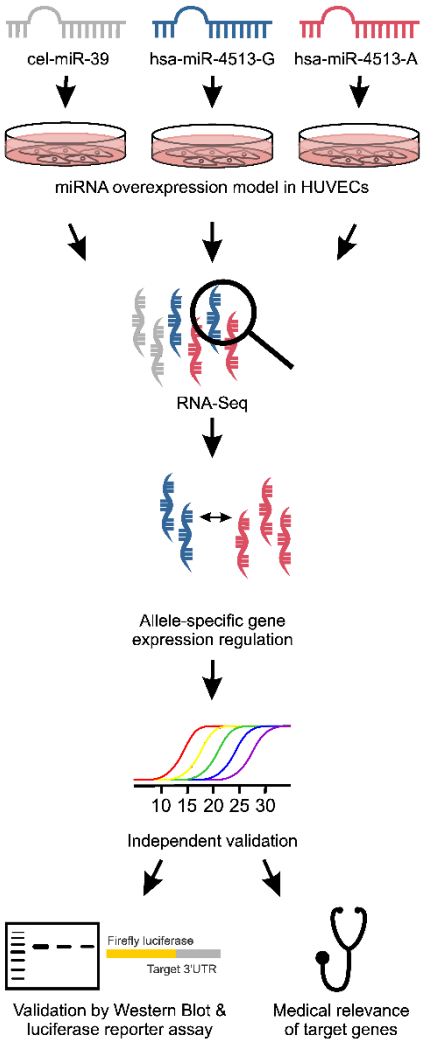

Figure 22. Schematic study design for identification of allele-specific target genes of rs2168518 in hsa-miR-4513.
Human umbilical vein endothelial cells (HUVEC) were transfected with miRNA mimics of hsa-miR-4513 harboring the A or G allele of rs2168518 or the control miRNA cel-miR-39. RNA was isolated and sequenced (RNA-Seq). Allele-specific target genes were identified and independently replicated *via* qRT-PCR. Selected candidate genes were validated by Western Blot analysis and luciferase reporter assay. Further, all replicated allele-specific target genes were screened for their medical relevance by publicly available databases (Figure modified from Kiel et al., 2021 [95]).

5.4.1 Overexpression of miRNA mimics in primary endothelial cells

Establishing a valid miRNA overexpression model, HUVECs were transfected with miRNA mimics of hsa-miR-4513-A, hsa-miR-4513-G or the control cel-miR-39, the latter having no sequence homologue in human. Transfection efficiency was validated by qRT-PCR 48 h after transfection. Thereby, cel-miR-39 served as control for hsa-miR-4513-A and hsa-miR-4513-G, while cells transfected with hsa-miR-4513-A and hsa-miR-4513-G served combined as control for cel-miR-39. For all three miRNAs a robust overexpression was detectable, which ranged between 676-fold to 1,458-fold in comparison to the respective control (**Figure 23**).

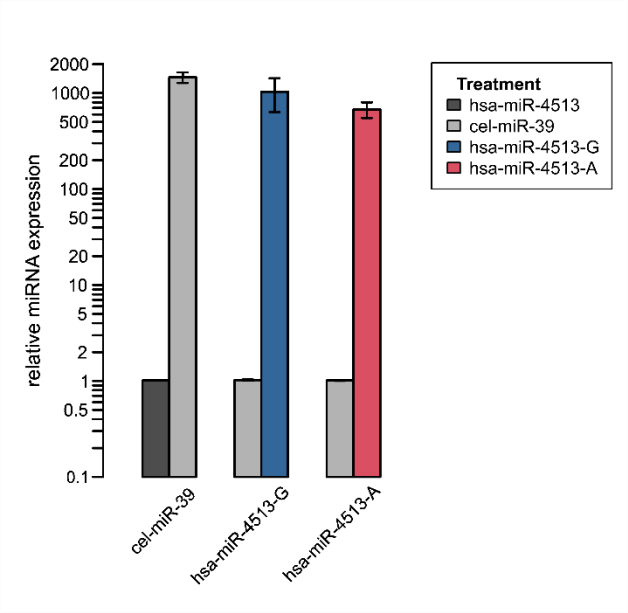

Figure 23. Relative miRNA expression in HUVECs 48 h after transfection.

HUVECs were transfected with miRNA mimics of hsa-miR-4513-A, hsa-miR-4513-G or the control cel-miR-39. RNA was isolated 48 h after transfection and transfection efficiency was determined *via* qRT-PCR. Relative miRNA expression was determined in comparison to the respective control. Cel-miR-39 served as control for hsa-miR-4513-A and hsa-miR-4513-G, while cells transfected with hsa-miR-4513-A and hsa-miR-4513-G served combined as control for cel-miR-39. Shown are mean values from three independent experiments, with 3-6 replicates each. Bars indicate standard error (SE) (Figure modified from Kiel et al., 2021 [95]).

5.4.2 Allele-specific target genes identified *via* RNA sequencing

HUVECs were transfected with miRNA mimics of hsa-miR-4513-A, hsa-miR-4513-G and the control cel-miR-4513. RNA was isolated 48 h after transfection and libraries for RNA-Seq were generated. RNA-Seq was performed by the Genomics Core Facility “KFB – Center of Excellence for Fluorescent Bioanalytics” (University of Regensburg) and raw RNA-Seq data were processed and normalized by Dr. Tobias Strunz (Institute of Human Genetics, University of Regensburg) as described elsewhere [95,134]. Allele-specific target genes of hsa-miR-4513 with rs2168518 were identified by the following two criteria including (1) significantly altered expression between hsa-miR-4513-A and hsa-miR-4513-G transfected samples (linear regression model, FDR corrected, q-value < 0.01) and (2) a significantly reduced expression in comparison to samples transfected with the miRNA control cel-miR-39 (q-value < 0.01) to be considered as direct target genes. In total, fifteen direct target genes were characterized for hsa-miR-4513-G (**Figure 24A, Supplementary Table 7**) and eight direct target genes for hsa-miR-4513-A (**Figure 24B, Supplementary Table 8**).

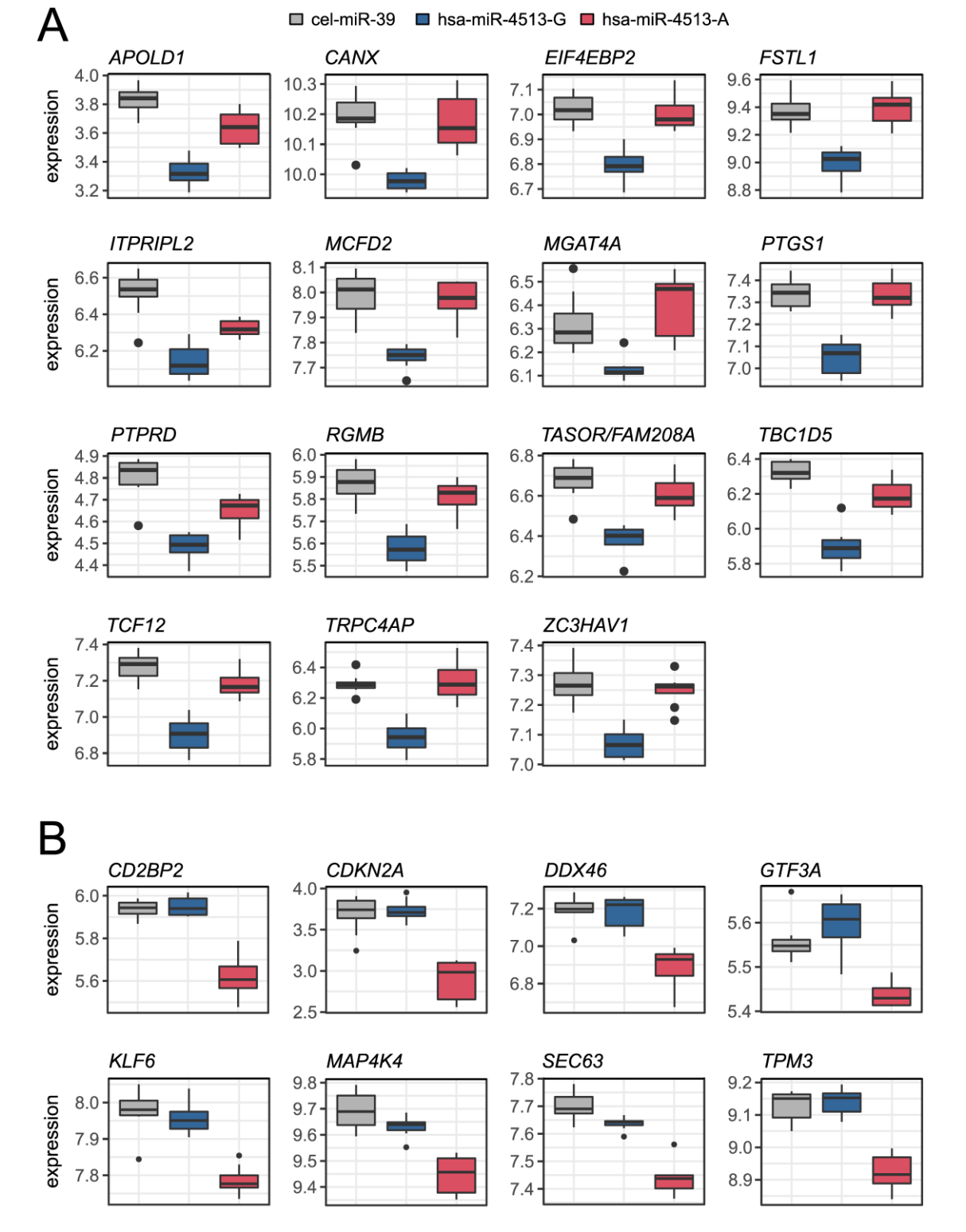

Figure 24. Allele-specific target genes of hsa-miR-4513.

Boxplots show the expression of allele-specific target genes of **(A)** hsa-miR-4513-G and **(B)** hsa-miR-4513-A. HUVECs were transfected with hsa-miR-4513-A, hsa-miR-4513-G or the control cel-miR-39 and RNA-Seq was performed. In total, 15 genes were considered as direct target genes of hsa-miR-4513-G and 8 genes as direct target genes of hsa-miR-4513-A, all displaying significant expression differences (q-value < 0.01) in comparison to

samples transfected with the alternative allele of rs2168518 in hsa-miR-4513 and the control cel-miR-39 (Figure modified from Kiel et al., 2021 [95]).

5.4.3 Replication of allele-specific target genes

All 23 allele-specific target genes identified in the RNA-Seq data were independently replicated *via* qRT-PCR. For this purpose, RNA was isolated from independently transfected HUVECs, again with hsa-miR-4513-A, hsa-miR-4513-G and the control cel-miR-39. Overall, for all allele-specific target genes the expression trend from the RNA-Seq analysis was replicated, although not all reached statistical significance (Kruskal-Wallis test, p-value < 0.05) (**Figure 25, Supplementary Table 9**).

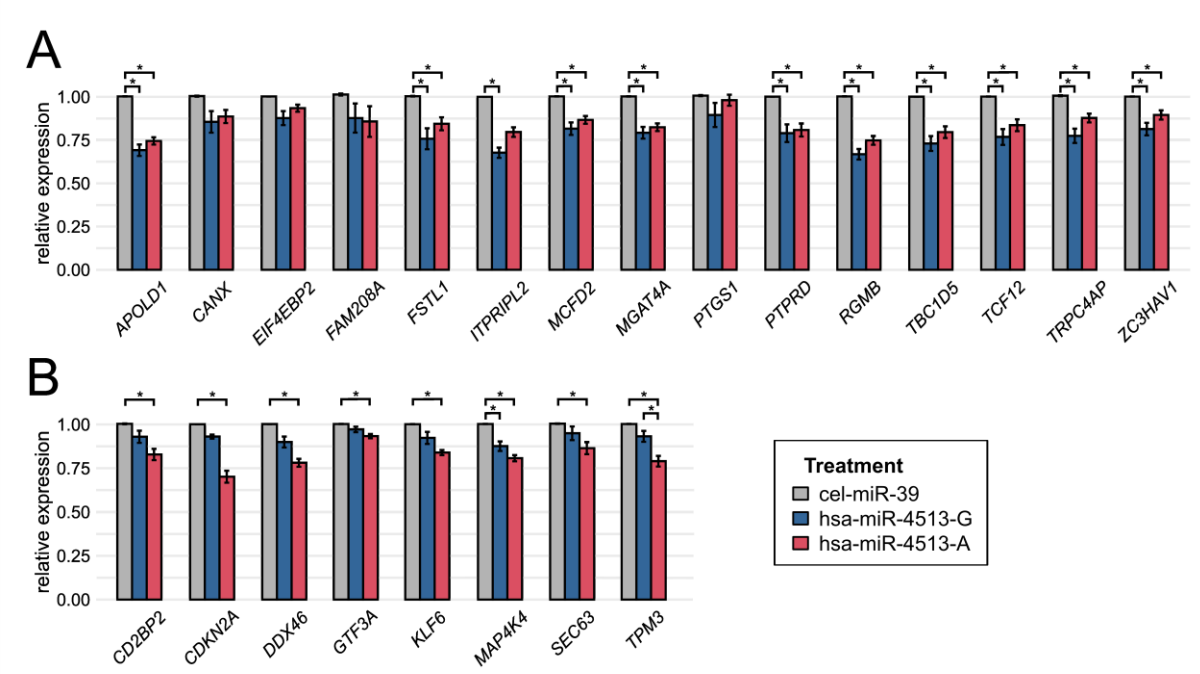

Figure 25. Replication of allele-specific target genes *via* qRT-PCR.

Allele-specific target genes identified in the RNA-Seq data were independently replicated in HUVECs *via* qRT-PCR. Therefore, cells were transfected with hsa-miR-4513-A, hsa-miR-4513-G or the control cel-miR-39 and RNA was isolated after 48 h. The relative expression was normalized to the cel-miR-39 transfected samples. **(A)** Allele-specific target genes of hsa-miR-4513-G and **(B)** allele-specific target genes of hsa-miR-4513-A. Shown are mean values from five to six independent experiments, with two to three replicates each. Bars indicate SE. Statistical significance was analyzed with the Kruskal-Wallis test followed by Dunn's multiple comparison test to correct for multiple testing. * adjusted p-value < 0.05 (Figure modified from Kiel et al., 2021 [95]).

Out of 15 allele-specific target genes of hsa-miR-4513-G, eleven showed a statistically significant reduced expression in the replication when compared to the cel-miR-39 control samples (Dunn's multiple comparison test, adjusted p-value < 0.05). In addition, ten of the

eleven genes also displayed a significantly reduced expression in hsa-miR-4513-A transfected samples in comparison to the control samples (adjusted p-value < 0.05), but no gene displayed a significant expression difference between hsa-miR-4513-A and hsa-miR-4513-G expressing samples.

Further, all eight potentially allele-specific target genes of hsa-miR-4513-A displayed a significantly reduced expression in the replication analysis in comparison to the control group (adjusted p-value < 0.05). One of those genes, namely *MAP4K4*, also displayed a significantly reduced expression in hsa-miR-4513-G expressing samples in comparison to the control group (adjusted p-value = 0.030). Only one gene, *TPM3*, showed a significant difference in expression between hsa-miR-4513-A and hsa-miR-4513-G transfected samples (adjusted p-value = 0.021).

For further investigation of allele-specific target genes by Western Blot analysis and luciferase reporter assay, genes were selected according to the following criteria: (1) significant expression difference in the replication analysis between the three investigated groups (Kruskal-Wallis test p-value < 0.05), (2) high expression in HUVECs (Ct-value < 25), (3) absolute expression difference between the hsa-miR-4513 samples with the allele of interest and the control samples transfected with cel-miR-39 of > 15 % and (4) significant expression difference for only one of the two hsa-miR-4513 alleles in comparison to the control samples (Dunn's multiple comparison test, adjusted p-value < 0.05). Overall, six genes fulfilled those criteria, one target gene of hsa-miR-4513-G, namely *ITPRIPL2*, and five target genes of hsa-miR-4513-A, namely *CD2BP2*, *CDKN2A*, *DDX46*, *KLF6* and *TPM3*.

5.4.4 Validation of exemplary allele-specific target genes *via* Western Blot analysis

Western Blot analysis was performed for validation of an allele-specific effect of rs2168518 in the seed region of hsa-miR-4513 on protein expression of exemplary target genes. In total, protein products of five allele-specific target genes of hsa-miR-4513-A were analyzed, namely CD2BP2, DDX46, KLF6, TPM3 and the isoform p16 as protein product of the *CDKN2A* gene. All of them showed a significantly decreased protein level in the hsa-miR-4513-A samples in comparison to the control samples transfected with cel-miR-39 (Dunn's multiple comparison test, adjusted p-value < 0.05) (**Figure 26**). One of the proteins, namely DDX46, also displayed a significantly reduced protein amount in hsa-miR-4513-G transfected samples in comparison to the control miRNA (adjusted p-value = 0.023). In addition, two proteins, p16 and KLF6, showed a significant expression difference between the two hsa-miR-4513 alleles (adjusted p-value = 0.042 and 0.044).

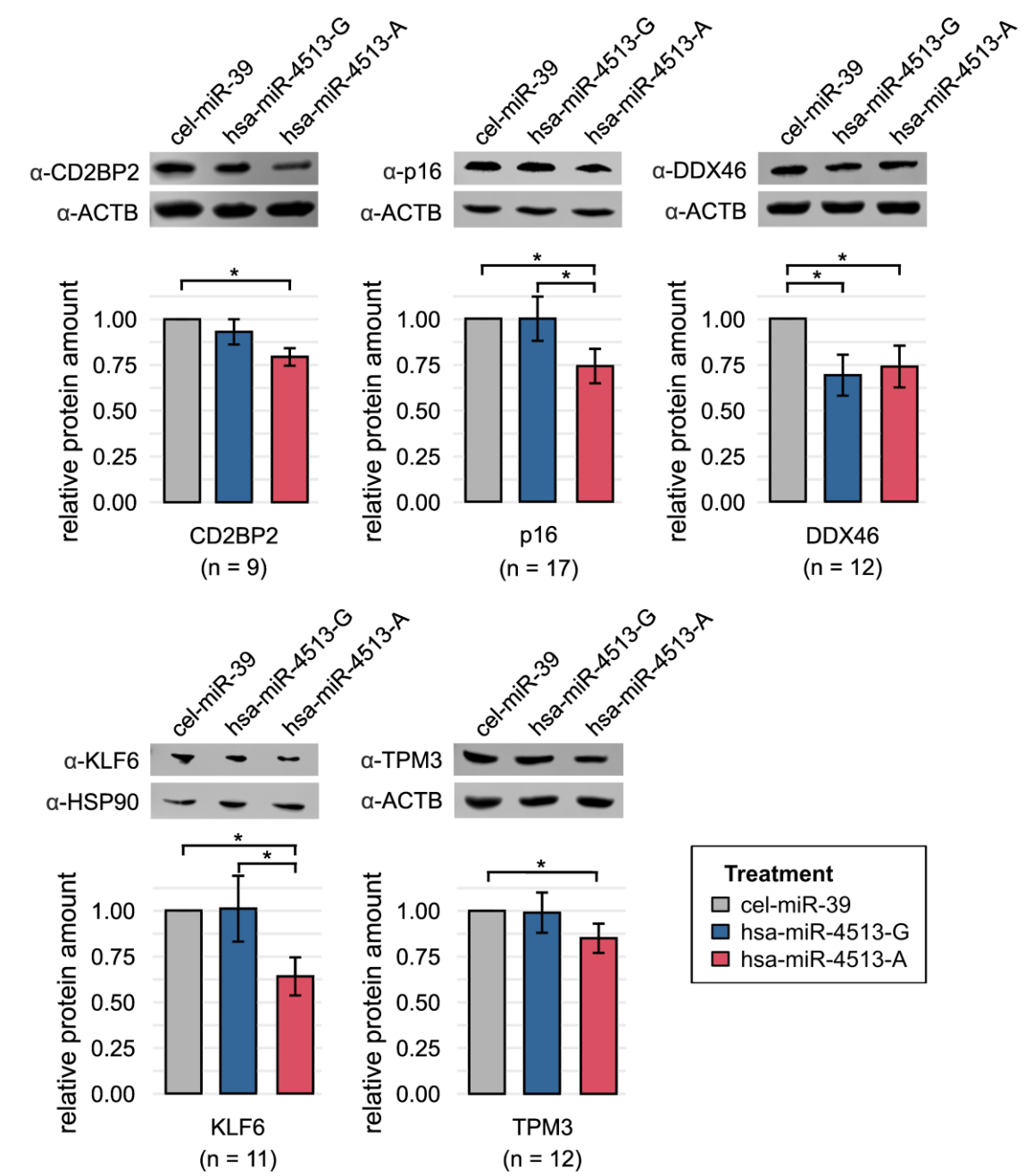

Figure 26. Validation of allele-specific target genes on protein level by Western Blot analysis.
Representative Western Blots of five selected allele-specific target genes of hsa-miR-4513 with their respective loading control ACTB. For KLF6, HSP90 was used as loading control. Isoform p16 represents one of the protein products of the *CDKN2A* gene. All samples were normalized for their respective loading control and the control cel-miR-39. Bar plots show mean values from nine to 17 independent experiments. Bars indicate SE. Statistical significance was analyzed with the Kruskal-Wallis test followed by a Dunn's multiple comparison test to correct for multiple testing. * adjusted p-value < 0.05, n = sample size (Figure modified from Kiel et al., 2021 [95]).

Additionally, one protein product of an allele-specific target gene of hsa-miR-4513-G was investigated, namely ITPRIPL2. Currently, little is known about the *ITPRIPL2* gene and also

about the protein and it was not possible to detect a specific protein immunostaining in the Western Blot analysis. Therefore, no statement can be made about a regulatory effect of hsa-miR-4513 on ITPRIPL2.

Overall, the investigated genes and their protein products, with the exception of *ITPRIPL2*, are valid target genes of hsa-miR-4513. Additionally, four genes confirmed their allele-specific regulation through rs2168518 in hsa-miR-4513, namely *CD2BP2*, *CDKN2A*, *KLF6* and *TPM3*.

5.4.5 Validation of selected allele-specific target genes *via* luciferase reporter assay

A luciferase reporter assay was used to validate the allele-specific binding of the two hsa-miR-4513 variants on the 3'-UTR of their target genes. For this purpose, HEK293T cells were co-transfected with the miRNA mimics of hsa-miR-4513-A, hsa-miR-4513-G or the control cel-miR-39 and a luciferase reporter vector. The reporter vector contains a *luciferase* coding region in combination with the 3'-UTR derived from the target gene transcript of interest. If a specific binding of the miRNA occurs, the luminescence signal emitted by the luciferase is diminished. If no specific miRNA binding occurs, for example if the miRNA is not able to bind due to alterations in its seed region, the luciferase signal remains unchanged (**Figure 27**).

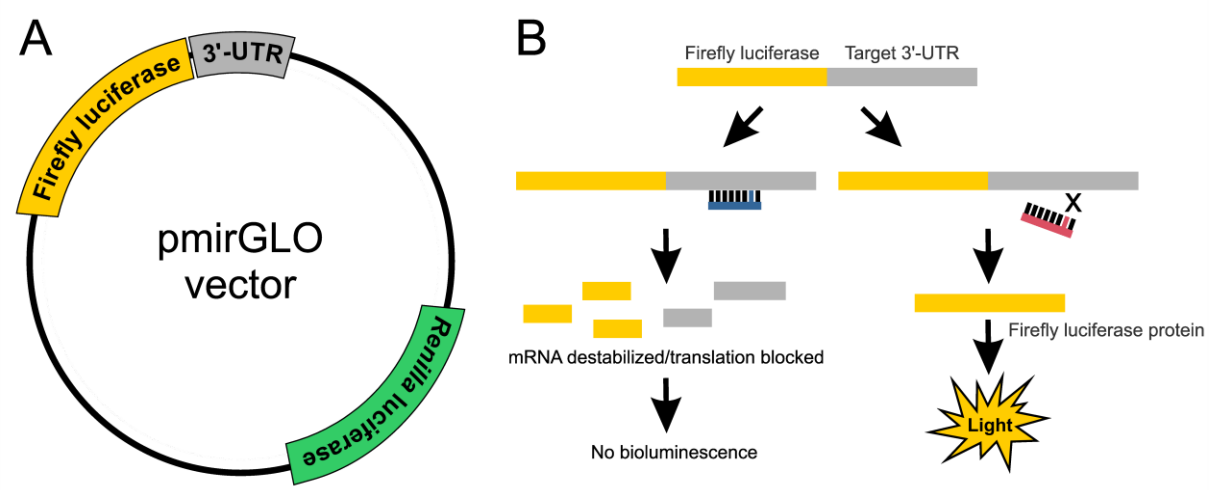

Figure 27. Schematic principle of the luciferase reporter assay.
(A) The 3'-UTR of target genes of the miRNA of interest were inserted into the pmirGLO reporter vector as the 3'-UTR of the *firefly luciferase* gene. **(B)** In case a specific binding of the miRNA to the 3'-UTR is possible, binding leads to the destabilization of the mRNA transcript or blocks the translation of the firefly luciferase. This results in a reduced bioluminescence. If the miRNA is not able to bind to the 3'-UTR, the firefly luciferase transcript can be translated and a light signal is detectable (Figure modified from Kiel et al., 2021 [95]).

For all exemplary target genes, 3'-UTR sequences of the transcripts of interest were obtained from the UCSC Genome browser tool [96,97] and screened for potential binding sites of hsa-miR-4513 with a length of at least seven nucleotides. Remarkably, all transcripts investigated contain allele-specific binding sites for hsa-miR-4513 (**Figure 28**). Transcripts of four target genes, namely *CDKN2A* (four transcripts investigated), *DDX46*, *TPM3* and *ITPRIPL2*, contain binding sites perfectly complementary to the seed region of hsa-miR-4513. For *CDKN2A* four transcripts created by alternative splicing were investigated and all contain the same binding region for hsa-miR-4513-A. Transcripts of two target genes, *CD2BP2* and *KLF6*, contain allele-specific binding sites for hsa-miR-4513 extending the seed region of hsa-miR-4513, but still include the polymorphic site. Overall, the allele-specificity of the binding sites perfectly match the previously obtained results of allele-specific mRNA repression.

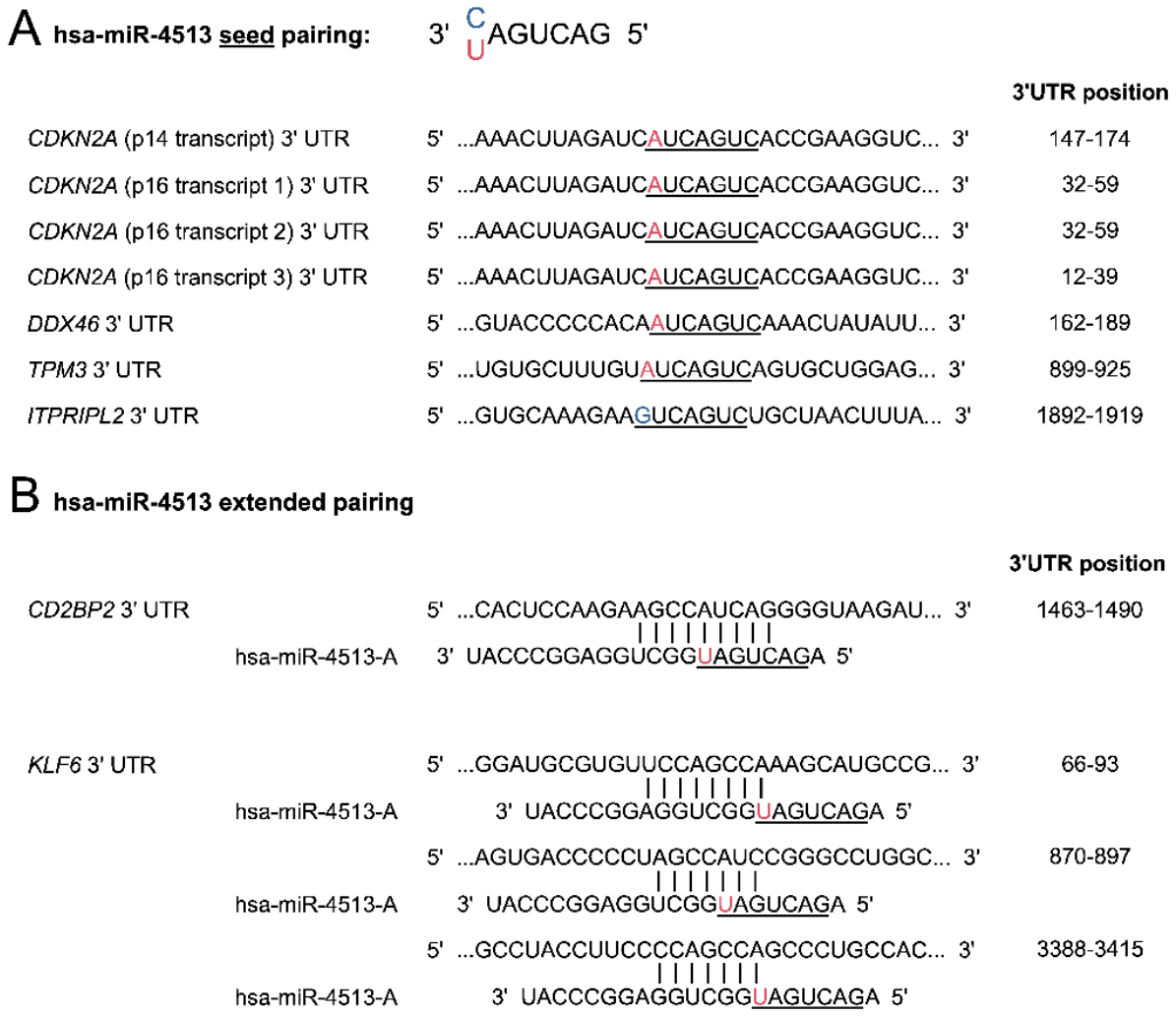

Figure 28. Allele-specific binding sites in the 3'-UTR of allele-specific target genes of hsa-miR-4513.
The UCSC Genome Browser online database [96] was used to retrieve 3'-UTR sequences of allele-specific target genes of hsa-miR-4513. 3'-UTR sequences were screened for potential binding sites of hsa-miR-4513 with at least seven nucleotides. 3'-UTR positions start with 1 for the first nucleotide after the stop codon of the coding sequence. All investigated exemplary allele-specific target gene transcripts displayed allele-specific binding sites for the

expected hsa-miR-4513 variant. **(A)** Target gene transcripts with a perfectly complementary sequence for the allele-specific seed sequence of hsa-miR-4513. For *CDKN2A* four different isoforms were investigated and all of them contain the same binding region for hsa-miR-4513-A. **(B)** Target gene transcripts with complementary sequences for an extended seed sequence pairing of hsa-miR-4513, which include the rs2168518 position in the miRNA for binding to the transcript (Figure modified from Kiel et al., 2021 [95]).

As a quality check for the luciferase reporter assay, the transfection efficiency of co-transfection with miRNA mimics, including hsa-miR-4513-A, hsa-miR-4513-G or cel-miR-39, and the empty luciferase reporter vector pmirGLO was tested. Expression of miRNAs was determined by qRT-PCR 24 h after co-transfection. In total, a valid overexpression of miRNAs after co-transfection was observed, ranging from 762-fold to 2,330-fold (**Figure 29**).

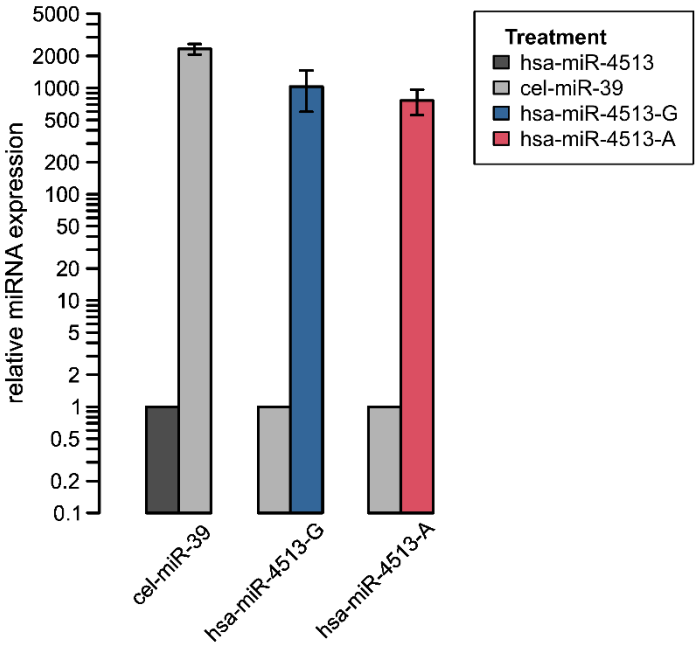

Figure 29. Relative miRNA expression in human embryonic kidney (HEK293T) cells after co-transfection with a luciferase reporter vector.
HEK293T cells were co-transfected with miRNA mimics of hsa-miR-4513-A, hsa-miR-4513-G or the control cel-miR-39 and the empty luciferase reporter vector pmirGLO. Cells were transfected in 96-well plates and four wells were combined to one sample. 24 h after transfection RNA was isolated and transfection efficiency was determined *via* qRT-PCR. Relative miRNA expression was determined in comparison to the respective control. Cel-miR-39 served as control for hsa-miR-4513-A and hsa-miR-4513-G, while a combination of cells transfected with hsa-miR-4513-A and hsa-miR-4513-G served as control for cel-miR-39. Shown are mean values from four independent experiments, with 2 replicates each. Bars indicate SE (Figure modified from Kiel et al., 2021 [95]).

To ensure reliability of the luciferase reporter assay, a reporter vector containing an internal transfection control was used. The luminescence signal of the firefly luciferase was normalized to a second luminescence signal of a *Renilla* luciferase, which is independent of miRNA binding (**Figure 27A**). Further, binding of the three miRNA mimics to the empty reporter vector pmirGLO was tested. Although cells co-transfected with hsa-miR-4513-A and hsa-miR-4513-G showed a slightly reduced luminescence signal in comparison to the control group

transfected with cel-miR-39, this difference was not statistically significant (Dunn's multiple comparison test, adjusted p-value > 0.05) (**Figure 30**).

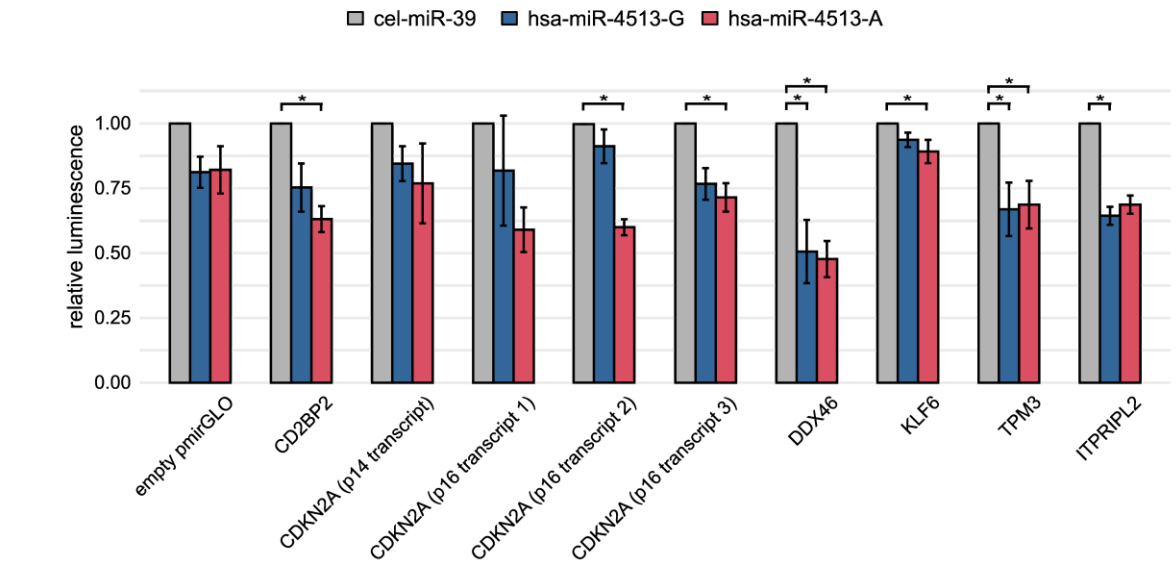

Figure 30. Allele-specific binding of hsa-miR-4513 to the 3'UTR of target transcripts determined by luciferase reporter assay.

HEK293T cells were co-transfected with miRNA mimics of hsa-miR-4513-A, hsa-miR-4513-G or cel-miR-39 and the luciferase reporter vector pmirGLO containing the 3'-UTR of allele-specific transcripts of interest. The luminescence signal was measured 24 h after co-transfection and corrected for transfection efficiency by a second luciferase signal, a *Renilla* luciferase, which is independent of miRNA binding. Values were further normalized to the control miRNA cel-miR-39. For *CDKN2A*, four transcripts were investigated. Shown are mean values from four independent experiments, with four to six replicates each. Bars indicate SE and statistical significance was tested with a Kruskal-Wallis test followed by a Dunn's multiple comparison test to correct for multiple testing. * adjusted p-values < 0.05 (Figure modified from Kiel et al., 2021 [95]).

In contrast, all selected target genes exhibited a significant reduction in luminescence when transfected with one of the hsa-miR-4513 alleles in comparison to the control group (Dunn's multiple comparison test, adjusted p-value < 0.05). For three genes, *CD2BP2*, *KLF6* and *ITPRIPL2*, a significant reduction in luminescence occurred for only one hsa-miR-4513 allele in comparison to the control group (*CD2BP2* hsa-miR-4513-A vs control adjusted p-value = 0.011, *KLF6* hsa-miR-4513-A vs control adjusted p-value = 0.011, *ITPRIPL2* hsa-miR-4513-G vs control adjusted p-value = 0.016). For two genes, *DDX46* and *TPM3*, a significant reduction of luminescence occurred when co-transfected with both hsa-miR-4513 variants in comparison to the control group (*DDX46* hsa-miR-4513-A vs control adjusted p-value = 0.038 and hsa-miR-4513-G vs control adjusted p-value = 0.033; *TPM3* hsa-miR-4513-A vs control adjusted p-value = 0.038 and hsa-miR-4513-G vs control adjusted p-value = 0.033).

For *CDKN2A*, four transcripts, which all showed robust expression in primary RNA-Seq data from HUVECs, were investigated. Two of those transcripts, p16 transcript 2 corresponding to ENST00000578845 and p16 transcript 3 corresponding to ENST00000579122, showed a significantly reduced luminescence when co-transfected with hsa-miR-4513-A in comparison to the control (p16 transcript 2 adjusted p-value = 0.016 and p16 transcript 3 adjusted p-value = 0.021).

Overall, the results of the luciferase reporter assay confirmed the earlier analysis and reinforce that the seed polymorphism rs2168518 of hsa-miR-4513 influences gene expression in an allele-specific manner. Target genes, which displayed an allele-specific binding of hsa-miR-4513 in their 3'-UTR are *CD2BP2*, *CDKN2A*, *KLF6* and *ITPRIPL2*.

5.4.6 Medical relevance of allele-specific target genes

The above findings highlight the association of the seed polymorphism rs2168518 with AMD, as well as its pleiotropic effect. In addition, several recent studies also reported associations of rs2168518 or the miRNA hsa-miR-4513 with different phenotypes, including AMD [124], cardiovascular phenotypes [129–131], diabetes and lipid levels [129], as well as cancer [70,135–138]. Combining our data and data from the literature, associations can be classified into six groups including AMD, cardiovascular phenotypes, cancer, lipid traits, metabolic products in urine and diabetes. This wide range of phenotype associations raises the question whether allele-specific target genes of hsa-miR-4513 can be linked to these phenotypes. Therefore, publicly available databases such as OMIM [120] and MGI [121] were screened for phenotype-related key words (**Supplementary Table 10**). Since the previous analyses validly confirmed exemplary selected allele-specific target genes of hsa-miR-4513, all 19 genes replicated by qRT-PCR were included for the following investigation of medical relevance of allele-specific target genes.

In total, ten out of nineteen allele-specific target genes were assigned to previously mentioned phenotype groups, whereby some genes were assigned to multiple phenotypes (**Figure 31**). Two genes were assigned to three phenotypes, namely *CDKN2A* (AMD, cancer and metabolic products in urine) and *FSTL1* (cardiovascular phenotypes, cancer and metabolic products in urine). Another two genes were assigned to two groups of phenotypes, namely *CD2BP2* (cardiovascular phenotypes and metabolic products in urine) and *KLF6* (cardiovascular phenotypes and cancer). Overall, two genes were assigned to AMD, namely *TBC1D4* and *CDKN2A*.

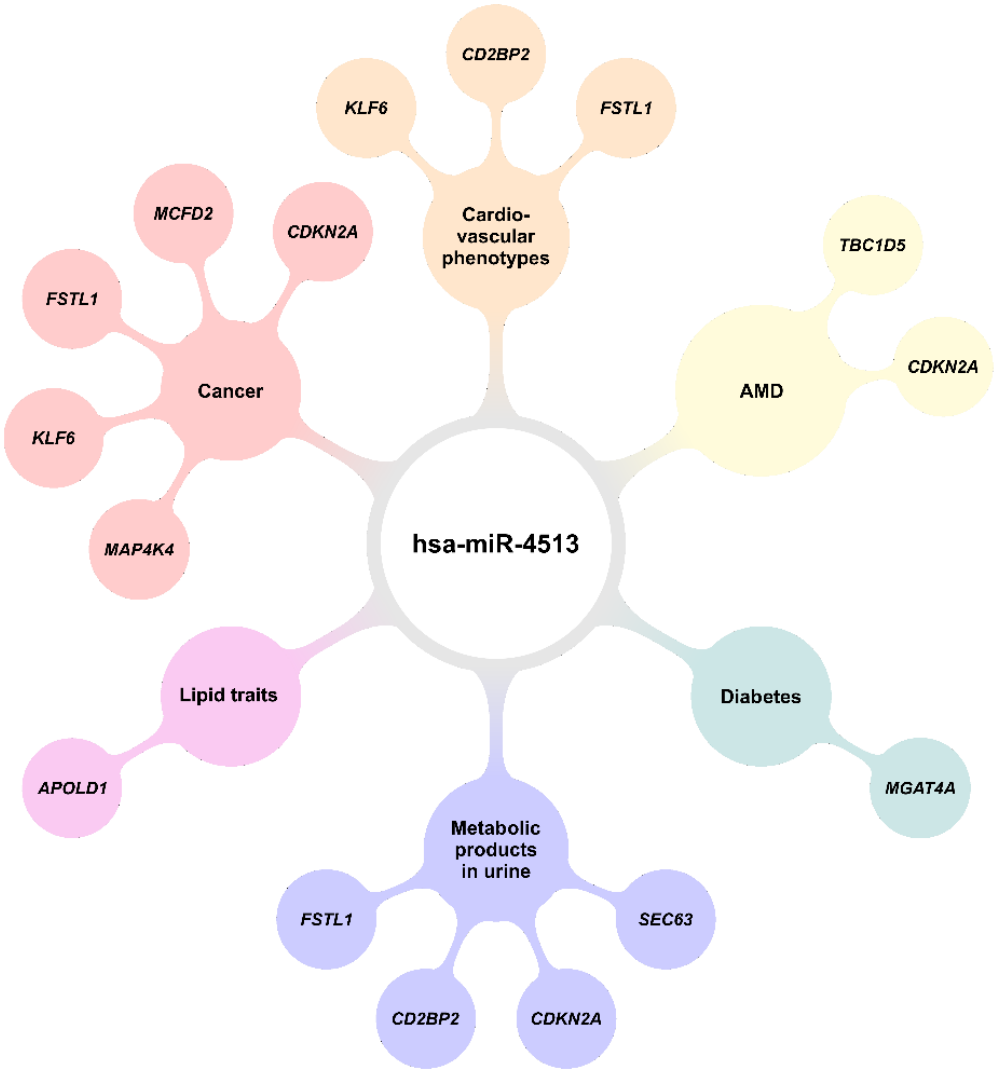

Figure 31. Allele-specific target genes related to phenotypes associated with hsa-miR-4513 or its seed polymorphism rs2168518 according to literature.

Above mentioned analyses as well as several recent studies highlighted the contribution of hsa-miR-4513 and its seed polymorphism rs2168518 to six different phenotype groups, including AMD [124], cardiovascular phenotypes [129–131], cancer [70,135–138], diabetes [129], lipid traits [129], as well as metabolic products in urine. Online databases Online Mendelian Inheritance in Man (OMIM) [120] and Mouse Genome Informatics (MGI) [121] were searched to assign 19 allele-specific target genes of hsa-miR-4513 to individual phenotype groups by specific key words defined as follows: “cell proliferation” or “cell death” (cancer), “cardiovascular system” (cardiovascular phenotypes), “vision/eye” (AMD), “cellular glucose” or “insulin resistance” (diabetes), “homeostasis/metabolism” and “renal/urinary system” (metabolic products in urine), and “lipid binding” (lipid traits) (Figure adopted from Kiel et al., 2021 [95]).

In summary, based on the literature, several allele-specific target genes could be assigned to phenotypes previously associated with hsa-miR-4513 or its seed polymorphisms and therefore have a high potential to resolve the biological mechanism underlying the association with hsa-miR-4513.

6 Discussion

In the last 15 years, GWAS contributed substantially to the identification of genetic signals associated with complex traits and diseases. Those studies are designed to detect genetic associations, but they cannot identify causal genetic variants or dissolve the biological mechanism underlying the association signal. Therefore, even four years after the most recent and most comprehensive GWAS performed for the AMD condition [20], still only little is known about the mechanisms underlying the highly significant genetic association signals identified [26].

To overcome this issue and to seek functional evidence for the genetic associations in AMD, several approaches were applied as part of this thesis. The first approach investigated pleiotropic effects of AMD-associated genes to reveal molecular mechanisms shared between different complex diseases, which might highlight important biological processes contributing to AMD pathobiology. One exemplary and highly interesting pleiotropic locus, namely 15q24.1, identified in the pleiotropy analysis of AMD-associated genes was further characterized in a subsequent approach by detailed *in silico* analyses to elucidate the mechanisms underlying the association of this specific locus with AMD. These *in silico* analyses included investigations of AMD subtype associations, an extended analysis of pleiotropic effects by including data from the UK Biobank, as well as the analysis of TF binding sites. In a further approach, the impact of one polymorphism, rs2168518, located in the pleiotropic locus 15q24.1 on post-transcriptional gene expression regulation was investigated in detail, as this polymorphism is one of the rare polymorphisms in the seed region of a miRNA, namely hsa-miR-4513. As the seed region of a miRNA is crucial for recognition and binding of miRNAs to their target genes, a polymorphism in this highly conserved region might have a great impact on the regulatory function of the miRNA and as a result probably also might influence phenotypic expression. Additionally, miRNAs are discussed as potential biomarkers and drug targets for complex conditions like AMD. Therefore, the final approach of this thesis investigated the expression of miRNAs in a clinically relevant mouse model of laser-induced choroidal NV to evaluate the potential of miRNAs to be applied in the future in such a clinical context for the NV subtype of AMD.

In order to uncover molecular mechanisms of genetic associations with AMD, a first project of this thesis dealt with potential pleiotropic effects of AMD-associated genes, identified in a recent TWAS performed at the Institute of Human Genetics in Regensburg [83]. The aim of the pleiotropy analysis was to identify genes or loci contributing to different complex phenotypes. This approach has the potential to highlight crucial pathological processes involved in distinct diseases and offers the possibility to transfer knowledge from one pathological phenotype to another to increase our understanding of pathobiological

mechanisms. The analysis of pleiotropic effects was achieved by comparing genomic positions of AMD-associated genes with GWAS loci of a broad range of complex phenotypes. This analysis revealed an enrichment for AMD-associated genes to physically overlap with GWAS loci of neurological diseases, metabolic traits, autoimmune diseases and organ function phenotypes. The phenotypes with an enrichment of AMD-associated genes in GWAS loci identified by the pleiotropy analysis can be divided into two groups. The first group is defined by phenotypes known to correlate with AMD represented by neurological diseases, metabolic traits and autoimmune diseases [41,139–145]. In contrast, the second group compromises exclusively phenotypes with no obvious correlation with AMD and includes solely organ function phenotypes. In the following, results of the enrichment analysis will be examined more closely for both result groups to highlight how our knowledge about AMD pathology can benefit from pleiotropy analysis by bringing interesting genes into focus for future AMD-related studies.

The first result group of the enrichment analysis includes phenotypes for which a correlation with AMD is already highly discussed, namely autoimmune diseases, metabolic traits and neurological diseases [41,139–145]. The latter is of special interest as the retina is a neurological tissue and is one of the most affected sites in AMD pathology, therefore AMD is classified as a retinal neurodegenerative disease [146]. It is not surprising that similar pathological processes may contribute to both AMD and other neurological, especially neurodegenerative, diseases. The neurodegenerative disease for which a possible correlation with AMD is most widely discussed, due to similarities of their pathology as well as the fact that both diseases are age-dependent, is Alzheimer's disease [140,147]. This is in line with the finding of this thesis, that eight out of 15 AMD-associated genes located in GWAS loci of neurological diseases correspond to GWAS loci associated with Alzheimer’s disease. Interestingly, these eight genes are located in two distinct loci, both previously reported to be associated with AMD and Alzheimer’s disease [20,148–150]. The first locus at 19p13.3 harbors *ABCA7* and the second locus at 7q22.1 contains seven AMD-associated genes, namely *NYAP1, TSC22D4*, *PMS2P1*, *STAG3L5P*, *PILRA*, *PILRB* and *ZCWPW1*. Research into the biological mechanism of *ABCA7* (*ATP Binding Cassette Subfamily A Member 7*) in Alzheimer’s disease revealed, that ABCA7 deficiency worsens amyloid-β accumulation, which is most likely mediated through an inhibited phagocytotic activity of macrophages and impaired amyloid-β clearance through microglia [151]. Accumulation of amyloid-β occurs not only in Alzheimer’s disease, but similarly was found in AMD patients as component of drusen [152]. While it has been shown that also in healthy retinal tissue amyloid-β accumulates age-dependently accompanied by an up-regulation of macrophages [153], the pathological impact of *ABCA7* on this process was so far not investigated in context of AMD. Therefore, the *ABCA7* locus represents an excellent candidate to demonstrate, how the analysis of pleiotropic effects might contribute to increase the knowledge about functional consequences of genetic associations.

The second result group of the enrichment analysis of AMD-associated genes in GWAS loci of distinct phenotypes is represented solely by organ function phenotypes and displays a result group for which no obvious correlation with AMD was reported before. However, a closer examination of this finding revealed, that the enrichment of AMD-associated genes in GWAS loci of organ function phenotypes is mainly related to the physical overlap with one single locus, 16q23.1, harboring several AMD-associated genes. Remarkably, this locus is not only associated with AMD and organ function related phenotypes, but also with four further phenotypes and therefore represents a strongly pleiotropic locus. Besides the association of this locus with AMD [20] and organ function phenotypes [154], further associations of the same locus are reported for the phenotype group cancer [155], neurological diseases [156], autoimmune diseases [157], and metabolic phenotypes [158]. With six phenotype group associations the 16q23.1 locus exhibited the strongest pleiotropic effect in the analysis conducted. In total, three AMD-associated genes are located in this region, namely *BCAR1*, *CFDP1* and *TMEM170A*. While there is no further evidence for the functional impact of *CFDP1* and *TMEM170A* on AMD pathology, there are some interesting findings regarding *BCAR1*. BCAR1 (Breast Cancer Anti-Estrogen Resistance 1) belongs to the Crk-associated substrate family of adaptor and scaffold proteins and is involved in various intracellular signaling events, as well as multiple biological processes, including amongst others cell motility, adhesion and proliferation [159]. The variety of essential biological mechanisms in which *BCAR1* is involved is a possible explanation for the highly pleiotropic effect observed for the 16q23.1 locus. Especially important for AMD pathology, Crk-associated substrate signaling-adaptor proteins have been reported to be crucial for the organization of the single-cell retinal ganglion cell layer in mice [160]. Further, whole exome sequencing of 63 multiplex families affected by AMD identified two rare coding variants in the *BCAR1* gene [161], which highlights the importance of this gene for AMD pathology. In summary, the enrichment of AMD-associated genes in GWAS loci of organ function phenotypes is probably attributable to one highly pleiotropic locus containing several AMD-associated genes. Within this highly pleiotropic locus, the AMD-associated gene with the apparently highest functional relevance for AMD is represented by *BCAR1*, which is an interesting candidate for further AMD-related research.

Pleiotropy analyses are a promising approach to uncover molecular mechanisms behind genetic associations, as can be seen in the examples already discussed. However, it should be considered, that an observed pleiotropic effect does not necessarily imply pleiotropy, but could also be due to coincidence, because of the complex LD structure in most genomic regions. In fact, almost 250,000 genetic associations with different phenotypes are already documented in the GWAS Catalog (as of February 25, 2021) [162], which demonstrates the high likelihood of randomly overlapping association signals. To distinguish between true pleiotropy and randomly occurring physical overlap of association signals, co-localization

analyses, which compare association signals from one locus with two different phenotypes, can be performed. Thereby, the co-localization analysis does not only include the lead variants of the associations, which may overlap due to the underlying LD structure, but considers all genetic variants in the corresponding locus [116]. It should be mentioned that this approach does not identify one single causal variant, but colocalization studies can be applied to determine whether association signals correspond to the same genetic signal. Overall, this demonstrates the complexity underlying the interpretation of GWAS associations and highlights the necessity to investigate each single genetic signal carefully.

To gain insight into functionality of a genetic association it is crucial to characterize association signals individually and in detail for which *in silico* analyses can be very helpful. However, individual AMD-associated loci have rarely been investigated so far [26]. Therefore, a complex locus on chromosome 15, namely 15q24.1, was characterized in detail as an exemplary locus to demonstrate the complexities when addressing the issue of genetic association and biological function.

Characterization of the 15q24.1 locus and its association with AMD exposed several important findings. Firstly, a closer look at AMD subtypes revealed that the association seems to be mainly related to the neovascular manifestation but not to the atrophic late stage form of the disease. Additionally, analyzing pleiotropic effects of 15q24.1 demonstrated that the identical genetic signal, which is associated with AMD, is also related to blood pressure phenotypes. This suggests, that the 15q24.1 locus is specifically involved in a process related to both neovascularization in AMD and blood pressure regulation, such as processes related to the homeostasis of endothelial cells [163]. This finding is of special interest, as several studies performed association analyses with a specific subtype of AMD, but rarely detected genetic variants, which are indeed specifically associated with one subtype [34–36,164]. Genetic variants associated with one specific subtype of AMD harbor the potential to shed light on biological mechanisms contributing to a specific pathological process like angiogenesis. Further, subtype-specific variants might be useful as progression predictors. For instance, prediction of disease progression might be applied to answer the question if an early stage patient is at high risk to develop late stage AMD or if a patient with GA is at high risk to progress to NV. Both, the use as potential progression predictors and the contribution to specific disease-relevant biological processes, make subtype-specific associated variants of particular interest for AMD research.

On the basis of the subtype-specific association of 15q24.1 with AMD, analysis of molecular traits, in particular gene expression, was performed beyond the course of this work. An eQTL analysis, a popular method to study the functional impact of an association, using data from the genotype-tissue expression project (GTEx) [165] revealed one gene of particular interest,

namely *Cytochrome P450 Family 1 Subfamily A Member 1* (*CYP1A1*). *CYP1A1* represents an remarkable potentially causal candidate as its regulation colocalizes with both the AMD and blood pressure association signal in several tissues [125]. CYP1A1 is involved in the response to oxidative stress by contributing in the detoxification of polycyclic aromatic hydrocarbons [166,167]. This is of special interest, as oxidative stress is an important contributor to AMD pathogenesis [168]. Although genes involved in the detoxification reaction were investigated with regard to AMD before large-scale GWAS were feasible, so far no significant genetic association between *CYP1A1* and AMD was detected [169]. In this context it is of interest that in an animal model of AMD, *CYP1A1* showed a reduced expression in the retina in comparison to control animals [170]. This is in agreement with a reduced *CYP1A1* expression in samples with AMD risk alleles at the 15q24.1 locus in the eQTL results using the GTEx data [125]. Additionally, in line with the blood pressure association, an animal study highlighted the importance of *CYP1A1* for oxidative stress-induced hypertension [171]. Overall, *CYP1A1* represents a promising functional candidate gene at 15q24.1 to contribute to NV pathology.

Delineation of locus 15q24.1 revealed another remarkable finding, namely a gender-specific association with AMD. Interestingly, the association of 15q24.1 was specifically detected in male individuals, but not in females. This gender-specific association with AMD is underpinned by the fact that a larger sample size was available for the female specific analysis in comparison to the male specific association analysis. Interestingly, although blood pressure phenotype associations of 15q24.1 correspond to the same genetic signal as AMD, this association did not display gender-specific effects, with one single exception. Only for one of the ten investigated blood pressure phenotypes, respectively the blood pressure treatment with ramipril, a male specific association was detected. In contrast, another phenotype association, which also corresponds to the same genetic signal, revealed a gender-specific association, but in the opposite direction than AMD. The phenotype code “Hearing difficulty/problems with background noise” only showed an association with 15q24.1 in female individuals. These results support a potential gender-specific regulation mechanism at 15q24.1, although it may be an elusive finding, as it is difficult to investigate. For gender-specific eQTL calculations the statistical power in databases like GTEx is insufficient due to low samples sizes usually in the range of 70 – 600 [165]. Nevertheless, there is evidence, that a gender-specific transcriptional regulation occurs at 15q24.1 through alterations in binding sites of sex-specific TFs, such as Zinc Finger Protein X-Linked (ZFX), Sex Determining Region Y (SRY) and SRY-Box Transcription Factor 9 (SOX9). Those factors play a crucial role in gender differentiation. For instance, a recent study reported that ZFX, for which the coding gene is located on the X chromosome, is a key mediator of sex-chromosome dosage effects of genome expression [172] and both, SRY and SOX9, are important factors for sex determination [133]. It still remains to be resolved how the same genetic signal at 15q24.1

displays different gender specificities between different phenotype associations. While a contribution of gender-specific TFs is likely, the exact mechanism underlying those gender-specific associations needs further investigation.

The results of this thesis highlighted, that an in-depth *in silico* characterization of association signals is a valuable tool to create many new hypotheses. However, bioinformatical approaches cannot take all biological mechanisms into account. For instance, the 15q24.1 locus harbors another functionally highly interesting candidate, a member of the miRNA family of regulatory molecules. MiRNAs are important regulators of post-transcriptional gene expression and are being discussed as promising candidates for future clinical applications.

A recent and broadly discussed clinical application for miRNAs is the usage as biomarkers for complex diseases [77,81,173,174]. Although several studies investigated dysregulated cmiRNAs in blood of AMD patients, they revealed diverse and partly contradictory results [56,76,85–89]. Therefore, the question arises whether miRNAs are suitable as biomarkers for AMD. The contradictory results of previous studies investigating cmiRNAs in AMD might likely be attributable to different study designs, low sample sizes or confounding environmental factors, which can have a dramatic impact on epigenetic regulators like miRNAs [175]. To this end, a clinically relevant and commonly used *in vivo* mouse model with laser-induced NV [176–178] was applied in the course of the present work to identify robustly dysregulated cmiRNAs. In total, three dysregulated cmiRNAs were found, namely mmu-miR-155-5p, mmu-miR-486a-5p and mmu-miR-92a-3p. All three cmiRNAs displayed a robustly altered expression after laser treatment, validated by several replication steps. However, the question arises how specific these three cmiRNAs are for the NV pathology as all of them were previously reported to contribute to several diseases or even to act as potential biomarker for different disorders [179–183], while only miR-155 was previously shown to be dysregulated in AMD patients [89]. Moreover, mmu-miR-486a-5p and mmu-miR-92a-3p were dysregulated mainly on day 3 after laser treatment, which is characterized by an immune reaction due to the laser treatment [176,184]. For this reason, follow-up studies are essential to reproduce the observed findings and to clarify the underlying biological mechanisms, which could provide indications for both, the specificity and the reliability of cmiRNAs as biomarkers for human NV development.

An alternative approach to identify potential cmiRNA biomarkers for NV might be a meta-analysis. By combining data from several independent studies, the sample size increases and with it the statistical power. This is particularly important as most expression differences of cmiRNAs detected are relatively small and high inter-individual cmiRNA expression fluctuations were reported [175,185,186]. It could make sense to focus directly on an altered cmiRNA profile comprising multiple cmiRNAs rather than on individual cmiRNAs. This way, expression fluctuations of individual cmiRNAs would not have such a large impact. A second

alternative approach could focus on the establishment of more stringent protocols for the identification of cmiRNAs. Especially, the origin of the samples investigated might greatly influence the cmiRNA profiles. A study conducted in 2016 showed that inter-individual variability is smaller than inter-tissue variability [187]. Furthermore, a study investigating the difference of cmiRNA profiles between arterial and venous plasma in rats showed that the origin of the plasma already had an impact on the obtained cmiRNA profiles [188]. This suggests that a uniform isolation protocol of cmiRNAs has the potential to greatly improve the reproducibility of cmiRNA expression studies. Overall, the concept of miRNAs as potential disease biomarkers harbors several complex challenges, which need to be resolved before a clinical use can be considered.

Besides the clinical application as biomarkers, miRNAs could also serve as potential therapeutic targets. For such an application an important point to consider is the cell type-specific mechanism of action of miRNAs. To study the cell type-specificity, the expression of two cmiRNAs showing altered expression in the laser mouse model of NV was further investigated in ocular tissues directly affected by the laser treatment, the retina and RPE/choroid. The miRNAs investigated in this study, mmu-miR-486a-5p and mmu-miR-92a-3p, displayed a downregulation after laser induction in blood at day 3, while they were up-regulated after laser induction in the RPE/choroid and further did not show any expression differences in the retina at the same time point. These two miRNAs therefore display a highly tissue dependent expression pattern after laser treatment. This is in line with previous reports, which described considerable expression differences of miRNAs in distinct cell types. For instance, in the developing brain, a robust variation of miRNA expression has been reported in closely related cell types [189]. Moreover, a recent study suggested that expression heterogeneity of intercellular miRNAs might contribute considerably to non-genetic cell to cell variability [190]. The cell type-specific expression pattern of miRNAs highlights the requirement for cell type-specific experimental approaches to investigate miRNA expression, as for example the increasingly emerging single-cell sequencing methods. Knowledge about the cell type-specific expression of miRNAs would also help to enhance the insight into the functional impact of specific miRNAs, which in turn can contribute to the design of specific therapeutic interventions.

While the cell type-specificity of miRNAs remains to be investigated in future studies, their tissue-specificity can be derived from the results of the laser mouse model in this thesis. As previously mentioned, day 3 after laser treatment is characterized by a strong immune reaction [176,184] and, therefore, dysregulation of cmiRNAs mmu-miR-486a-5p and mmu-miR-92a-3p at this time point in blood may be related to the immune response of the treated mice. As the ocular tissue is directly affected by laser damage, alterations in miRNA expression at an early time point after treatment might be related to a stress response mechanism of the eye. Actually,

the observed upregulation of mmu-miR-486a-5p and mmu-miR-92a-3p in the RPE/choroid is in line with results of previous studies investigating those two miRNAs in the context of oxidative stress [191,192]. A recent study reported an upregulation of hsa-miR-486-5p, the human homologue of mmu-miR-486a-5p, in ARPE-19 cells, a human RPE cell line, after induction of oxidative stress [191]. Further, a comparable effect was reported for the second miRNA mmu-miR-92a-3p, where the human homologue hsa-miR-92a-3p was shown to be upregulated upon oxidative stress in HUVECs [192]. Hence, upregulation of mmu-miR-486a-5p and mmu-miR-92a-3p may be a cell type-specific oxidative stress reaction of RPE and endothelial cells in the choroid.

Besides the initial stress response peaking at day 3, the expression of mmu-miR-92a-3p in RPE/choroid steadily increased over time after laser treatment. The later time point after NV induction is characterized by an angiogenic reaction [176]. MiRNA miR-92a-3p is known to be an important regulator of angiogenesis, with most studies reporting an antiangiogenic function [193–196]. However, there is also evidence that modulation of miR-92a-3p expression in endothelial cells, regardless of the direction of expression, may enhance angiogenesis under oxidative stress. It is therefore suggested that once expression of miR-92a-3p sways outside a very narrow homeostatic expression range, angiogenic processes may be triggered [196]. Overall, overexpression of mmu-miR-92a-3p after laser induction in RPE/choroid may be initially related to a stress reaction comparable to oxidative stress, followed by enhanced angiogenesis. On the other hand, an increased expression of mmu-miR-92a-3p during the angiogenic reaction could also indicate an innate reaction to antagonize angiogenesis. In summary, the altered expression of mmu-miR-92a-3p in RPE/choroidal tissue after laser-induced NV is in line with previous studies [193–196] highlighting the importance of this miRNA in angiogenesis.

In addition to the quantity of miRNA expression, alterations in the post-transcriptional target gene regulation might contribute to disease pathologies. MiRNA binding to target genes is mediated by the so called seed region spanning nucleotide 2 – 7 at the 5’-end of the miRNA [62,197]. Genetic variants located in this crucial and highly conserved region are rare and less than 1 % of miRNAs are known to harbor genetic variants in the seed region [64]. Notably, such seed polymorphisms are expected to have a strong influence on the regulatory function of the miRNA [65]. The AMD-associated locus 15q24.1 investigated in the course of this work harbors a seed polymorphism, namely rs2168518, located in hsa-miR-4513.

With the assumption, that miRNA hsa-miR-4513 with its seed polymorphism might contribute to AMD phenotype expression, the influence of the seed polymorphism rs2168518 on gene expression regulation was investigated. Although an overall consistent and reproducible allele-specific regulation of target genes by hsa-miR-4513 in several *in vitro* models was observed,

a few genes failed to show an allele-specific effect of hsa-miR-4513 regulation in individual assays. Those discrepancies can likely be attributed to methodological causes. For instance, different cell lines as well as different time points were used to investigate the effect of the miRNA on their target genes, because the primary cell line used for the identification of miRNA target genes is difficult to transfect. Since co-transfection is required for the luciferase reporter assay and thus both miRNA and target 3'-UTR are present in significant excess, an easier-to-transfect cell line was used for this purpose. However, this may well affect the function of the miRNA, as was mentioned earlier with regard to the tissue specificity of miRNAs [189,190]. Furthermore, the *in vitro* model used to investigate the impact of hsa-miR-4513 relies on an overexpression of the miRNA species. Such a model system is not comparable to the physiological expression of a miRNA, which normally occurs at a much lower level, and might likely diminish allele-specific effects. In case both alleles of the miRNA are able to bind to a target, although with different specificities, the high exogenous expression may still result in a target gene repression of the less specific binding allele. However, there is currently no suitable alternative for such an overexpression model to accurately model the effects of a single base exchange in a miRNA without introducing other confounding factors. On the basis of the above arguments and the otherwise very uniform results, it can be assumed that the lack of allele specificity in individual approaches is rather due to methodological reasons. However, it is noteworthy that due to the rare occurrence of seed polymorphisms in miRNAs [64], there are no comparable large-scale *in vitro* studies, which leaves the assumptions to be based purely on methodological principles.

To investigate functional consequences of a miRNA, the respective target genes need to be investigated regarding their potential role in disease pathogenesis for the phenotype under consideration. In the present work this was done by screening publicly available databases for all allele-specific target genes of hsa-miR-4513 with validated mRNA expression repression. Remarkably, at least one allele-specific target gene was assigned to all six phenotype groups linked to hsa-miR-4513 or the seed polymorphism rs2168518. Overall, 10 out of 19 genes were assigned to at least one phenotype group and two genes were assigned to AMD, namely *TBC1 Domain Family Member 4* (*TBC1D4)* and *Cyclin Dependent Kinase Inhibitor 2A (CDKN2A)*. According to knockout mouse models in the MGI database, a knockout of *TBC1D4* or *CDKN2A* results in an eye phenotype and therefore both genes are likely to contribute to AMD pathology [121]. While the eye phenotype of *TBC1D4* knockout mice relates to an abnormal lens morphology, mice with a *CDKN2A* knock out reveal a variety of eye phenotypes including a failed regression of the hyaloid vascular system of the eye [121]. Overall, *CDKN2A* represents a promising allele-specific target gene of hsa-miR-4513, as its allele specificity was validated on mRNA and protein expression, as well as by luciferase reporter assay. Additionally, a

phenotype assignment revealed a contribution to the vascular system of the eye, which fits to the NV-related association of the seed polymorphism rs2168518 of hsa-miR-4513.

The *CDKN2A* gene encodes at least four distinct proteins, namely p12, p14, p16 and p16γ, generated by alternative splicing [198]. Two of those proteins are specifically expressed in distinct tissues or cell types, with p12 in pancreas and p16γ in tumor samples [198–200]. In contrast, p14 and p16 are expressed ubiquitously, exhibiting crucial functions in cell cycle regulation and tumor suppression [198,201]. However, there is also evidence that the expression of both proteins increases with age [202] and senescent cells expressing p16 have been reported to drive age-related pathologies [203]. Interestingly, not only aging increases p16 expression, but also exposure to chronic psychosocial stress [204]. In addition, a recent study reported *CDKN2A* to contribute to retinal ganglion cell death in an animal model of glaucoma [205]. Overall, the contribution of *CDKN2A* to age-related pathologies and contribution to death of retinal cells make this gene an interesting candidate for further AMD research.

In summary, this work highlights the importance to comprehensively investigate single genetic association signals of a complex disease to uncover biological mechanisms involved in disease pathologies. By combining different molecular functions with a genetic association signal, hypotheses which can enable new insights into pathological processes can be generated. However, different approaches can reveal different biological mechanisms and also varying candidate genes. This illustrates the complexity of even a single association signal and the importance to perform comprehensive *in silico* and *in vitro* analyses. This way, the present work provided valid evidence for two genes potentially contributing to the pathology of AMD mediated through the genetic association at 15q24.1, namely *CYP1A1* and *CDKN2A*. This is in line with the fact that while more and more genetic variants associated with AMD are being found, there has been little significant progress on identifying the underlying biological mechanisms. So, in combination with the environmental and age-related influences on AMD etiology and pathology, it is plausible that multiple genes can be influenced by one single association signal, and thus there has to be not one single obligatory pathway for each genetic signal that contributes to the manifestation of AMD.

Moreover, the presented work emphasizes the importance and complexity of the role of miRNAs in a complex disease like AMD. Although several clinical applications of miRNAs are feasible in the future, the present work highlights how important further investigations into the cell type specificity and target gene regulation are. Furthermore, an environmental influence such as oxidative stress exposure on miRNA expression and function is an important field of research before a clinical application of miRNAs as biomarkers or drug targets for AMD could be considered.

7 References

1. Bourne, R.R.A.; Flaxman, S.R.; Braithwaite, T.; Cicinelli, M. V.; Das, A.; Jonas, J.B.; Keeffe, J.; Kempen, J.H.; Leasher, J.; Limburg, H.; et al. Magnitude, temporal trends, and projections of the global prevalence of blindness and distance and near vision impairment: a systematic review and meta-analysis. *Lancet Glob. Health* **2017**, *5*, e888–e897, doi:10.1016/S2214-109X(17)30293-0.

2. Steinmetz, J.D.; Bourne, R.R.A.; Briant, P.S.; Flaxman, S.R.; Taylor, H.R.B.; Jonas, J.B.; Abdoli, A.A.; Abrha, W.A.; Abualhasan, A.; Abu-Gharbieh, E.G.; et al. Causes of blindness and vision impairment in 2020 and trends over 30 years, and prevalence of avoidable blindness in relation to VISION 2020: the Right to Sight: an analysis for the Global Burden of Disease Study. *Lancet Glob. Health* **2021**, *9*, e144–e160, doi:10.1016/S2214-109X(20)30489-7.

3. Wong, W.L.; Su, X.; Li, X.; Cheung, C.M.G.; Klein, R.; Cheng, C.-Y.; Wong, T.Y. Global prevalence of age-related macular degeneration and disease burden projection for 2020 and 2040: a systematic review and meta-analysis. *Lancet Glob. Health* **2014**, *2*, e106–e116, doi:10.1016/S2214-109X(13)70145-1.

4. Weinreb, R.N.; Aung, T.; Medeiros, F.A. The pathophysiology and treatment of glaucoma: a review. *JAMA* **2014**, *311*, 1901-1911, doi:10.1001/jama.2014.3192.

5. van Lookeren Campagne, M.; LeCouter, J.; Yaspan, B.L.; Ye, W. Mechanisms of age-related macular degeneration and therapeutic opportunities. *J. Pathol.* **2014**, *232*, 151–164, doi:10.1002/path.4266.

6. Nizami, A.A.; Gulani, A.C. Cataract; In: *StatPearls*. Treasure Island (FL): StatPearls Publishing, **2021**.

7. Ang, M.; Gatinel, D.; Reinstein, D.Z.; Mertens, E.; Alió del Barrio, J.L.; Alió, J.L. Refractive surgery beyond 2020. *Eye* **2021**, *35*, 362–382, doi:10.1038/s41433-020-1096-5.

8. Swaroop, A.; Chew, E.Y.; Bowes Rickman, C.; Abecasis, G.R. Unraveling a multifactorial late-onset disease: from genetic susceptibility to disease mechanisms for age-related macular degeneration. *Annu. Rev. Genomics Hum. Genet.* **2009**, *10*, 19–43, doi:10.1146/annurev.genom.9.081307.164350.

9. Lim, L.S.; Mitchell, P.; Seddon, J.M.; Holz, F.G.; Wong, T.Y. Age-related macular degeneration. *Lancet* **2012**, *379*, 1728–1738, doi:10.1016/S0140-6736(12)60282-7.

10. Weber, B.H.F.; Charbel Issa, P.; Pauly, D.; Herrmann, P.; Grassmann, F.; Holz, F.G. The role of the complement system in age-related macular degeneration. *Dtsch. Aerztebl. Int.* **2014**, *111*, 133–138, doi:10.3238/arztebl.2014.0133.

11. Ambati, J.; Fowler, B.J. Mechanisms of age-related macular degeneration. *Neuron* **2012**, *75*, 26–39, doi:10.1016/j.neuron.2012.06.018.

12. Delcourt, C.; Diaz, J.L.; Ponton-Sanchez, A.; Papoz, L. Smoking and age-related macular degeneration. The POLA Study. Pathologies Oculaires Liées à l'Age. *Arch. Ophthalmol.* **1998**, *116*, 1031–1035, doi:10.1001/archopht.116.8.1031.

13. Ding, X.; Patel, M.; Chan, C.-C. Molecular pathology of age-related macular

degeneration. *Prog. Retin. Eye Res.* **2009**, *28*, 1–18, doi:10.1016/j.preteyeres.2008.10.001.

14. Seddon, J.M.; Cote, J.; Page, W.F.; Aggen, S.H.; Neale, M.C. The US twin study of age-related macular degeneration: relative roles of genetic and environmental influences. *Arch. Ophthalmol.* **2005**, *123*, 321–327, doi:10.1001/archopht.123.3.321.

15. Smith, J.G.; Newton-Cheh, C. Genome-wide association study in humans. *Methods Mol. Biol.* **2009**; *573*, 231–258, doi: 10.1007/978-1-60761-247-6_14.

16. Tam, V.; Patel, N.; Turcotte, M.; Bossé, Y.; Paré, G.; Meyre, D. Benefits and limitations of genome-wide association studies. *Nat. Rev. Genet.* **2019**, *20*, 467–484, doi:10.1038/s41576-019-0127-1.

17. Klein, R.J.; Zeiss, C.; Chew, E.Y.; Tsai, J.-Y.; Sackler, R.S.; Haynes, C.; Henning, A.K.; SanGiovanni, J.P.; Mane, S.M.; Mayne, S.T.; et al. Complement factor H polymorphism in age-related macular degeneration. *Science* **2005**, *308*, 385–389, doi:10.1126/science.1109557.

18. Buniello, A.; MacArthur, J.A.L.; Cerezo, M.; Harris, L.W.; Hayhurst, J.; Malangone, C.; McMahon, A.; Morales, J.; Mountjoy, E.; Sollis, E.; et al. The NHGRI-EBI GWAS Catalog of published genome-wide association studies, targeted arrays and summary statistics 2019. *Nucleic Acids Res.* **2019**, *47*, D1005–D1012, doi:10.1093/nar/gky1120.

19. Pearson, T.A.; Manolio, T.A. How to interpret a genome-wide association study. *JAMA* **2008**, *299*, 1335–1344, doi:10.1001/jama.299.11.1335.

20. Fritsche, L.G.; Igl, W.; Bailey, J.N.C.; Grassmann, F.; Sengupta, S.; Bragg-Gresham, J.L.; Burdon, K.P.; Hebbring, S.J.; Wen, C.; Gorski, M.; et al. A large genome-wide association study of age-related macular degeneration highlights contributions of rare and common variants. *Nat. Genet.* **2016**, *48*, 134–143, doi:10.1038/ng.3448.

21. Pruim, R.J.; Welch, R.P.; Sanna, S.; Teslovich, T.M.; Chines, P.S.; Gliedt, T.P.; Boehnke, M.; Abecasis, G.R.; Willer, C.J. LocusZoom: regional visualization of genome-wide association scan results. *Bioinformatics* **2010**, *26*, 2336–2337, doi:10.1093/bioinformatics/btq419.

22. Edwards, S.L.; Beesley, J.; French, J.D.; Dunning, A.M. Beyond GWASs: illuminating the dark road from association to function. *Am. J. Hum. Genet.* **2013**, *93*, 779–797, doi:10.1016/j.ajhg.2013.10.012.

23. Hindorff, L.A.; Sethupathy, P.; Junkins, H.A.; Ramos, E.M.; Mehta, J.P.; Collins, F.S.; Manolio, T.A. Potential etiologic and functional implications of genome-wide association loci for human diseases and traits. *Proc. Natl. Acad. Sci. U S A* **2009**, *106*, 9362–9367, doi:10.1073/pnas.0903103106.

24. Gallagher, M.D.; Chen-Plotkin, A.S. The Post-GWAS Era: From Association to Function. *Am. J. Hum. Genet.* **2018**, *102*, 717–730, doi:10.1016/j.ajhg.2018.04.002.

25. Fritsche, L.G.; Chen, W.; Schu, M.; Yaspan, B.L.; Yu, Y.; Thorleifsson, G.; Zack, D.J.; Arakawa, S.; Cipriani, V.; Ripke, S.; et al. Seven new loci associated with age-related macular degeneration. *Nat. Genet.* **2013**, *45*, 433–439, doi:10.1038/ng.2578.

26. Strunz, T.; Kiel, C.; Sauerbeck, B.L.; Weber, B.H.F. Learning from Fifteen Years of

Genome-Wide Association Studies in Age-Related Macular Degeneration. *Cells* **2020**, *9*, 2267, doi:10.3390/cells9102267.

27. Wu, J.; Sun, X. Complement system and age-related macular degeneration: drugs and challenges. *Drug Des. Devel. Ther.* **2019**, *13*, 2413–2425, doi:10.2147/DDDT.S206355.

28. Kawa, M.P.; Machalinska, A.; Roginska, D.; Machalinski, B. Complement system in pathogenesis of AMD: dual player in degeneration and protection of retinal tissue. *J. Immunol. Res.* **2014**, *2014*, 483960, doi:10.1155/2014/483960.

29. Friedrich, U.; Myers, C.A.; Fritsche, L.G.; Milenkovich, A.; Wolf, A.; Corbo, J.C.; Weber, B.H.F. Risk- and non-risk-associated variants at the 10q26 AMD locus influence ARMS2 mRNA expression but exclude pathogenic effects due to protein deficiency. *Hum. Mol. Genet.* **2011**, *20*, 1387–1399, doi:10.1093/hmg/ddr020.

30. Cheng, Y.; Huang, L.; Li, X.; Zhou, P.; Zeng, W.; Zhang, C. Genetic and functional dissection of ARMS2 in age-related macular degeneration and polypoidal choroidal vasculopathy. *PLoS One* **2013**, *8*, e53665, doi:10.1371/journal.pone.0053665.

31. Kanda, A.; Chen, W.; Othman, M.; Branham, K.E.H.; Brooks, M.; Khanna, R.; He, S.; Lyons, R.; Abecasis, G.R.; Swaroop, A. A variant of mitochondrial protein LOC387715/ARMS2, not HTRA1, is strongly associated with age-related macular degeneration. *Proc. Natl. Acad. Sci. U S A* **2007**, *104*, 16227–16232, doi:10.1073/pnas.0703933104.

32. Grassmann, F.; Heid, I.M.; Weber, B.H.F. Recombinant Haplotypes Narrow the ARMS2/HTRA1 Association Signal for Age-Related Macular Degeneration. *Genetics* **2017**, *205*, 919–924, doi:10.1534/genetics.116.195966.

33. Visscher, P.M.; Brown, M.A.; McCarthy, M.I.; Yang, J. Five years of GWAS discovery. *Am. J. Hum. Genet.* **2012**, *90*, 7–24, doi:10.1016/j.ajhg.2011.11.029.

34. Ruamviboonsuk, P.; Tadarati, M.; Singhanetr, P.; Wattanapokayakit, S.; Kunhapan, P.; Wanitchanon, T.; Wichukchinda, N.; Mushiroda, T.; Akiyama, M.; Momozawa, Y.; et al. Genome-wide association study of neovascular age-related macular degeneration in the Thai population. *J. Hum. Genet.* **2017**, *62*, 957–962, doi:10.1038/jhg.2017.72.

35. Grassmann, F.; Harsch, S.; Brandl, C.; Kiel, C.; Nürnberg, P.; Toliat, M.R.; Fleckenstein, M.; Pfau, M.; Schmitz-Valckenberg, S.; Holz, F.G.; et al. Assessment of Novel Genome-Wide Significant Gene Loci and Lesion Growth in Geographic Atrophy Secondary to Age-Related Macular Degeneration. *JAMA Ophthalmol.* **2019**, *137*, 867-876, doi:10.1001/jamaophthalmol.2019.1318.

36. Winkler, T.W.; Grassmann, F.; Brandl, C.; Kiel, C.; Günther, F.; Strunz, T.; Weidner, L.; Zimmermann, M.E.; Korb, C.A.; Poplawski, A.; et al. Genome-wide association meta-analysis for early age-related macular degeneration highlights novel loci and insights for advanced disease. *BMC Med. Genomics* **2020**, *13*, 120, doi:10.1186/s12920-020-00760-7.

37. Biasella, F.; Plössl, K.; Karl, C.; Weber, B.H.F.; Friedrich, U. Altered Protein Function Caused by AMD-associated Variant rs704 Links Vitronectin to Disease Pathology. *Invest. Opthalmol. Vis. Sci.* **2020**, *61*, 2, doi:10.1167/iovs.61.14.2.

38. Strunz, T.; Grassmann, F.; Gayán, J.; Nahkuri, S.; Souza-Costa, D.; Maugeais, C.;

Fauser, S.; Nogoceke, E.; Weber, B.H.F. A mega-analysis of expression quantitative trait loci (eQTL) provides insight into the regulatory architecture of gene expression variation in liver. *Sci. Rep.* **2018**, *8*, 5865, doi:10.1038/s41598-018-24219-z.

39. Reinisalo, M.; Putula, J.; Mannermaa, E.; Urtti, A.; Honkakoski, P. Regulation of the human tyrosinase gene in retinal pigment epithelium cells: the significance of transcription factor orthodenticle homeobox 2 and its polymorphic binding site. *Mol. Vis.* **2012**, *18*, 38–54.

40. Maugeri, A.; Barchitta, M.; Fallico, M.; Castellino, N.; Reibaldi, M.; Agodi, A. Characterization of SIRT1/DNMTs Functions and LINE-1 Methylation in Patients with Age-Related Macular Degeneration. *J. Clin. Med.* **2019**, *8*, 159, doi:10.3390/jcm8020159.

41. Grassmann, F.; Kiel, C.; Zimmermann, M.E.; Gorski, M.; Grassmann, V.; Stark, K.; International AMD Genomics Consortium (IAMDGC); Heid, I.M.; Weber, B.H.F. Genetic pleiotropy between age-related macular degeneration and 16 complex diseases and traits. *Genome Med.* **2017**, *9*, 29, doi:10.1186/s13073-017-0418-0.

42. Paaby, A.B.; Rockman, M. V. The many faces of pleiotropy. *Trends Genet.* **2013**, *29*, 66–73, doi:10.1016/j.tig.2012.10.010.

43. Tyler, A.L.; Asselbergs, F.W.; Williams, S.M.; Moore, J.H. Shadows of complexity: what biological networks reveal about epistasis and pleiotropy. *Bioessays* **2009**, *31*, 220–227, doi:10.1002/bies.200800022.

44. Solovieff, N.; Cotsapas, C.; Lee, P.H.; Purcell, S.M.; Smoller, J.W. Pleiotropy in complex traits: challenges and strategies. *Nat. Rev. Genet.* **2013**, *14*, 483–495, doi:10.1038/nrg3461.

45. Jordan, D.M.; Verbanck, M.; Do, R. HOPS: a quantitative score reveals pervasive horizontal pleiotropy in human genetic variation is driven by extreme polygenicity of human traits and diseases. *Genome Biol.* **2019**, *20*, 222, doi:10.1186/s13059-019-1844-7.

46. Bulik-Sullivan, B.; Finucane, H.K.; Anttila, V.; Gusev, A.; Day, F.R.; Loh, P.-R.; ReproGen Consortium; Psychiatric Genomics Consortium; Genetic Consortium for Anorexia Nervosa of the Wellcome Trust Case Control Consortium 3; Duncan, L.; et al. An atlas of genetic correlations across human diseases and traits. *Nat. Genet.* **2015**, *47*, 1236–1241, doi:10.1038/ng.3406.

47. Watanabe, K.; Stringer, S.; Frei, O.; Umićević Mirkov, M.; de Leeuw, C.; Polderman, T.J.C.; van der Sluis, S.; Andreassen, O.A.; Neale, B.M.; Posthuma, D. A global overview of pleiotropy and genetic architecture in complex traits. *Nat. Genet.* **2019**, *51*, 1339–1348, doi:10.1038/s41588-019-0481-0.

48. Bird, A. Perceptions of epigenetics. *Nature* **2007**, *447*, 396–398, doi:10.1038/nature05913.

49. Wang, Z.; Long, H.; Chang, C.; Zhao, M.; Lu, Q. Crosstalk between metabolism and epigenetic modifications in autoimmune diseases: a comprehensive overview. *Cell. Mol. Life Sci.* **2018**, *75*, 3353–3369, doi:10.1007/s00018-018-2864-2.

50. Prasher, D.; Greenway, S.C.; Singh, R.B. The impact of epigenetics on cardiovascular

disease. *Biochem. Cell Biol.* **2020**, *98*, 12–22, doi:10.1139/bcb-2019-0045.

51. Miranda Furtado, C.L.; Dos Santos Luciano, M.C.; Silva Santos, R.D.; Furtado, G.P.; Moraes, M.O.; Pessoa, C. Epidrugs: targeting epigenetic marks in cancer treatment. *Epigenetics* **2019**, *14*, 1164–1176, doi:10.1080/15592294.2019.1640546.

52. Kumari, N.; Karmakar, A.; Ganesan, S.K. Targeting epigenetic modifications as a potential therapeutic option for diabetic retinopathy. *J. Cell. Physiol.* **2020**, *235*, 1933–1947, doi:10.1002/jcp.29180.

53. Egger, G.; Liang, G.; Aparicio, A.; Jones, P.A. Epigenetics in human disease and prospects for epigenetic therapy. *Nature* **2004**, *429*, 457–463, doi:10.1038/nature02625.

54. Martier, R.; Sogorb-Gonzalez, M.; Stricker-Shaver, J.; Hübener-Schmid, J.; Keskin, S.; Klima, J.; Toonen, L.J.; Juhas, S.; Juhasova, J.; Ellederova, Z.; et al. Development of an AAV-Based MicroRNA Gene Therapy to Treat Machado-Joseph Disease. *Mol. Ther. Methods Clin. Dev.* **2019**, *15*, 343–358, doi:10.1016/j.omtm.2019.10.008.

55. Revia, R.A.; Stephen, Z.R.; Zhang, M. Theranostic Nanoparticles for RNA-Based Cancer Treatment. *Acc. Chem. Res.* **2019**, *52*, 1496–1506, doi:10.1021/acs.accounts.9b00101.

56. Grassmann, F.; Schoenberger, P.G.A.; Brandl, C.; Schick, T.; Hasler, D.; Meister, G.; Fleckenstein, M.; Lindner, M.; Helbig, H.; Fauser, S.; et al. A circulating microRNA profile is associated with late-stage neovascular age-related macular degeneration. *PLoS One* **2014**, *9*, e107461, doi:10.1371/journal.pone.0107461.

57. Jun, S.; Datta, S.; Wang, L.; Pegany, R.; Cano, M.; Handa, J.T. The impact of lipids, lipid oxidation, and inflammation on AMD, and the potential role of miRNAs on lipid metabolism in the RPE. *Exp. Eye Res.* **2019**, *181*, 346–355, doi:10.1016/j.exer.2018.09.023.

58. Gemenetzi, M.; Lotery, A.J. Epigenetics in age-related macular degeneration: new discoveries and future perspectives. *Cell. Mol. Life Sci.* **2020**, *77*, 807–818, doi:10.1007/s00018-019-03421-w.

59. Natoli, R.; Fernando, N. MicroRNA as Therapeutics for Age-Related Macular Degeneration. *Adv. Exp. Med. Biol.* **2018**, *1074*, 37–43, doi:10.1007/978-3-319-75402-4_5.

60. Carthew, R.W.; Sontheimer, E.J. Origins and Mechanisms of miRNAs and siRNAs. *Cell* **2009**, *136*, 642–655, doi:10.1016/j.cell.2009.01.035.

61. Beitzinger, M.; Meister, G. Experimental identification of microRNA targets by immunoprecipitation of Argonaute protein complexes. *Methods Mol. Biol.* **2011**, *732*, 153–167, doi:10.1007/978-1-61779-083-6_12.

62. Chipman, L.B.; Pasquinelli, A.E. miRNA Targeting: Growing beyond the Seed. *Trends Genet.* **2019**, *35*, 215–222, doi:10.1016/j.tig.2018.12.005.

63. Felekkis, K.; Touvana, E.; Stefanou, C.; Deltas, C. microRNAs: a newly described class of encoded molecules that play a role in health and disease. *Hippokratia* **2010**, *14*, 236–240.

64. Saunders, M.A.; Liang, H.; Li, W.-H. Human polymorphism at microRNAs and microRNA target sites. *Proc. Natl. Acad. Sci. U S A* **2007**, *104*, 3300–3305, doi:10.1073/pnas.0611347104.

65. Ryan, B.M.; Robles, A.I.; Harris, C.C. Genetic variation in microRNA networks: the implications for cancer research. *Nat. Rev. Cancer* **2010**, *10*, 389–402, doi:10.1038/nrc2867.

66. Jafri, I.; Alsharif, G.; Bland, G.N.-I.; Gambhir, K.K. Erythrocyte miRNA 144 and miRNA 451 as Cell Aging Biomarkers in African American Adults. *Open Biochem. J.* **2019**, *13*, 81–87, doi:10.2174/1874091X01913010081.

67. Friedman, R.C.; Farh, K.K.-H.; Burge, C.B.; Bartel, D.P. Most mammalian mRNAs are conserved targets of microRNAs. *Genome Res.* **2009**, *19*, 92–105, doi:10.1101/gr.082701.108.

68. Jing, R.; Zhong, Q.-Q.; Long, T.-Y.; Pan, W.; Qian, Z.-X. Downregulated miRNA-26a-5p induces the apoptosis of endothelial cells in coronary heart disease by inhibiting PI3K/AKT pathway. *Eur. Rev. Med. Pharmacol. Sci.* **2019**, *23*, 4940–4947, doi:10.26355/eurrev_201906_18084.

69. Ding, Y.; Wang, L.; Zhao, Q.; Wu, Z.; Kong, L. MicroRNA-93 inhibits chondrocyte apoptosis and inflammation in osteoarthritis by targeting the TLR4/NF-κB signaling pathway. *Int. J. Mol. Med.* **2019**, *43*, 779–790, doi:10.3892/ijmm.2018.4033.

70. Xu, Y.-X.; Sun, J.; Xiao, W.-L.; Liu, Y.-S.; Yue, J.; Xue, L.-F.; Deng, J.; Zhi, K.-Q.; Wang, Y.-L. MiR-4513 mediates the proliferation and apoptosis of oral squamous cell carcinoma cells via targeting CXCL17. *Eur. Rev. Med. Pharmacol. Sci.* **2019**, *23*, 3821–3828, doi:10.26355/eurrev_201905_17809.

71. Mahesh, G.; Biswas, R. MicroRNA-155: A Master Regulator of Inflammation. *J. Interferon Cytokine Res.* **2019**, *39*, 321–330, doi:10.1089/jir.2018.0155.

72. Yu, A.; Zhang, T.; Zhong, W.; Duan, H.; Wang, S.; Ye, P.; Wang, J.; Zhong, S.; Yang, Z. miRNA-144 induces microglial autophagy and inflammation following intracerebral hemorrhage. *Immunol. Lett.* **2017**, *182*, 18–23, doi:10.1016/j.imlet.2017.01.002.

73. Wang, M.; Liu, C.; Su, Y.; Zhang, K.; Zhang, Y.; Chen, M.; Ge, M.; Gu, L.; Lu, T.; Li, N.; et al. miRNA-34c inhibits myoblasts proliferation by targeting YY1. *Cell Cycle* **2017**, *16*, 1661–1672, doi:10.1080/15384101.2017.1281479.

74. Zhong, G.; Long, H.; Ma, S.; Shunhan, Y.; Li, J.; Yao, J. miRNA-335-5p relieves chondrocyte inflammation by activating autophagy in osteoarthritis. *Life Sci.* **2019**, *226*, 164–172, doi:10.1016/j.lfs.2019.03.071.

75. Qu, X.; Han, J.; Zhang, Y.; Wang, X.; Fan, H.; Hua, F.; Yao, R. TLR4-RelA-miR-30a signal pathway regulates Th17 differentiation during experimental autoimmune encephalomyelitis development. *J. Neuroinflammation* **2019**, *16*, 183, doi:10.1186/s12974-019-1579-0.

76. Blasiak, J.; Watala, C.; Tuuminen, R.; Kivinen, N.; Koskela, A.; Uusitalo-Järvinen, H.; Tuulonen, A.; Winiarczyk, M.; Mackiewicz, J.; Zmorzyński, S.; et al. Expression of VEGFA-regulating miRNAs and mortality in wet AMD. *J. Cell. Mol. Med.* **2019**, *23*, 8464–8471, doi:10.1111/jcmm.14731.

77. Swarbrick, S.; Wragg, N.; Ghosh, S.; Stolzing, A. Systematic Review of miRNA as Biomarkers in Alzheimer's Disease. *Mol. Neurobiol.* **2019**, *56*, 6156–6167, doi:10.1007/s12035-019-1500-y.

78. Schulte, C.; Karakas, M.; Zeller, T. microRNAs in cardiovascular disease – clinical application. *Clin. Chem. Lab. Med.* **2017**, *55*, 687-704, doi:10.1515/cclm-2016-0576.

79. Bernardo, B.C.; Ooi, J.Y.Y.; Lin, R.C.Y.; McMullen, J.R. miRNA therapeutics: a new class of drugs with potential therapeutic applications in the heart. *Future Med. Chem.* **2015**, *7*, 1771–1792, doi:10.4155/fmc.15.107.

80. Backes, C.; Meese, E.; Keller, A. Specific miRNA Disease Biomarkers in Blood, Serum and Plasma: Challenges and Prospects. *Mol. Diagn. Ther.* **2016**, *20*, 509–518, doi:10.1007/s40291-016-0221-4.

81. Mazumder, S.; Datta, S.; Ray, J.G.; Chaudhuri, K.; Chatterjee, R. Liquid biopsy: miRNA as a potential biomarker in oral cancer. *Cancer Epidemiol.* **2019**, *58*, 137–145, doi:10.1016/j.canep.2018.12.008.

82. Ji, C.; Guo, X. The clinical potential of circulating microRNAs in obesity. *Nat. Rev. Endocrinol.* **2019**, *15*, 731–743, doi:10.1038/s41574-019-0260-0.

83. Strunz, T.; Lauwen, S.; Kiel, C.; International AMD Genomics Consortium (IAMDGC); den Hollander, A.; Weber, B.H.F. A transcriptome-wide association study based on 27 tissues identifies 106 genes potentially relevant for disease pathology in age-related macular degeneration. *Sci. Rep.* **2020**, *10*, 1584, doi:10.1038/s41598-020-58510-9.

84. Ratnapriya, R.; Sosina, O.A.; Starostik, M.R.; Kwicklis, M.; Kapphahn, R.J.; Fritsche, L.G.; Walton, A.; Arvanitis, M.; Gieser, L.; Pietraszkiewicz, A.; et al. Retinal transcriptome and eQTL analyses identify genes associated with age-related macular degeneration. *Nat. Genet.* **2019**, *51*, 606–610, doi:10.1038/s41588-019-0351-9.

85. Berber, P.; Grassmann, F.; Kiel, C.; Weber, B.H.F. An Eye on Age-Related Macular Degeneration: The Role of MicroRNAs in Disease Pathology. *Mol. Diagn. Ther.* **2017**, *21*, 31–43, doi:10.1007/s40291-016-0234-z.

86. Ertekin, S.; Yıldırım, O.; Dinç, E.; Ayaz, L.; Fidancı, S.B.; Tamer, L. Evaluation of circulating miRNAs in wet age-related macular degeneration. *Mol. Vis.* **2014**, *20*, 1057–1066.

87. Ménard, C.; Rezende, F.A.; Miloudi, K.; Wilson, A.; Tétreault, N.; Hardy, P.; SanGiovanni, J.P.; De Guire, V.; Sapieha, P. MicroRNA signatures in vitreous humour and plasma of patients with exudative AMD. *Oncotarget* **2016**, *7*, 19171–19184, doi:10.18632/oncotarget.8280.

88. Ren, C.; Liu, Q.; Wei, Q.; Cai, W.; He, M.; Du, Y.; Xu, D.; Wu, Y.; Yu, J. Circulating miRNAs as Potential Biomarkers of Age-Related Macular Degeneration. *Cell. Physiol. Biochem.* **2017**, *41*, 1413–1423, doi:10.1159/000467941.

89. Romano, G.L.; Platania, C.B.M.; Drago, F.; Salomone, S.; Ragusa, M.; Barbagallo, C.; Di Pietro, C.; Purrello, M.; Reibaldi, M.; Avitabile, T.; et al. Retinal and Circulating miRNAs in Age-Related Macular Degeneration: An In vivo Animal and Human Study. *Front. Pharmacol.* **2017**, *8*, 168, doi:10.3389/fphar.2017.00168.

90. Karlstetter, M.; Kopatz, J.; Aslanidis, A.; Shahraz, A.; Caramoy, A.; Linnartz-Gerlach, B.; Lin, Y.; Lückoff, A.; Fauser, S.; Düker, K.; et al. Polysialic acid blocks mononuclear phagocyte reactivity, inhibits complement activation, and protects from vascular damage in the retina. *EMBO Mol. Med.* **2017**, *9*, 154–166, doi:10.15252/emmm.201606627.

91. Kiel, C.; Berber, P.; Karlstetter, M.; Aslanidis, A.; Strunz, T.; Langmann, T.; Grassmann, F.; Weber, B.H.F. A Circulating MicroRNA Profile in a Laser-Induced Mouse Model of Choroidal Neovascularization. *Int. J. Mol. Sci.* **2020**, *21*, 2689, doi:10.3390/ijms21082689.

92. Hurteau, G.J.; Spivack, S.D.; Brock, G.J. Potential mRNA degradation targets of hsa-miR-200c, identified using informatics and qRT-PCR. *Cell Cycle* **2006**, *5*, 1951–1956, doi:10.4161/cc.5.17.3133.

93. Yoon, H.; Belmonte, K.C.; Kasten, T.; Bateman, R.; Kim, J. Intra- and Inter-individual Variability of microRNA Levels in Human Cerebrospinal Fluid: Critical Implications for Biomarker Discovery. *Sci. Rep.* **2017**, *7*, 12720, doi:10.1038/s41598-017-13031-w.

94. Livak, K.J.; Schmittgen, T.D. Analysis of relative gene expression data using real-time quantitative PCR and the 2(−Delta Delta C(T)) Method. *Methods* **2001**, *25*, 402–408, doi:10.1006/meth.2001.1262.

95. Kiel, C.; Strunz, T.; Hasler, D.; Meister, G.; Grassmann, F.; Weber, B.H.F. Seed sequence polymorphism rs2168518 and allele-specific target gene regulation of hsa-miR-4513. *Hum. Mol. Genet.* **2021**, ddab292, doi:10.1093/hmg/ddab292.

96. Kent, W.J.; Sugnet, C.W.; Furey, T.S.; Roskin, K.M.; Pringle, T.H.; Zahler, A.M.; Haussler, D. The human genome browser at UCSC. *Genome Res.* **2002**, *12*, 996–1006, doi:10.1101/gr.229102.

97. Karolchik, D.; Hinrichs, A.S.; Furey, T.S.; Roskin, K.M.; Sugnet, C.W.; Haussler, D.; Kent, W.J. The UCSC Table Browser data retrieval tool. *Nucleic Acids Res.* **2004**, *32*, D493-496, doi:10.1093/nar/gkh103.

98. R Core Team. R: A language and environment for statistical computing. R Foundation for Statistical Computing, Vienna, Austria, **2019**, Available online: https://www.R-project.org/.

99. Ogle, D.H. FSA: Fisheries Stock Analysis. R package version 0.4.31, **2014**, Available online: https://github.com/droglenc/FSA.

100. Pinheiro, J.; Bates, D.; Saikat, D.; Sarkar, D.; R Development Core Team nlme: Linear and Nonlinear Mixed Effects Models, **2016**, Available online: https://CRAN.R-project.org/package=nlme.

101. Heinze, G.; Ploner, M.; Dunkler, D.; Southworth, H. logistf: Firth's bias reduced logistic regression, **2013**, Available online: https://CRAN.R-project.org/package=logistf.

102. Robinson, M.D.; McCarthy, D.J.; Smyth, G.K. edgeR: a Bioconductor package for differential expression analysis of digital gene expression data. *Bioinformatics* **2010**, *26*, 139–140, doi:10.1093/bioinformatics/btp616.

103. Benjamini, Y.; Hochberg, Y. Controlling the False Discovery Rate: A Practical and

Powerful Approach to Multiple Testing. *J. R. Stat. Soc. Ser. B* **1995**, *57*, 289–300, doi:10.1111/j.2517-6161.1995.tb02031.x.

104. Pollard, K.S.; Dudoit, S.; van der Laan, M.J. Multiple Testing Procedures: the multtest Package and Applications to Genomics. In *Bioinformatics and Computational Biology Solutions Using R and Bioconductor*; Gentleman, R., Carey, V.J., Huber, W., Irizarry, R.A., Dudoit, S., Eds.; Springer (Statistics for Biology and Health Series), **2005**; pp. 249–271, doi:10.1007/0-387-29362-0_15.

105. Welter, D.; MacArthur, J.; Morales, J.; Burdett, T.; Hall, P.; Junkins, H.; Klemm, A.; Flicek, P.; Manolio, T.; Hindorff, L.; et al. The NHGRI GWAS Catalog, a curated resource of SNP-trait associations. *Nucleic Acids Res.* **2014**, *42*, D1001–D1006, doi:10.1093/nar/gkt1229.

106. 1000 Genomes Project Consortium; Abecasis, G.R.; Auton, A.; Brooks, L.D.; DePristo, M.A.; Durbin, R.M.; Handsaker, R.E.; Kang, H.M.; Marth, G.T.; McVean, G.A. An integrated map of genetic variation from 1,092 human genomes. *Nature* **2012**, *491*, 56–65, doi:10.1038/nature11632.

107. Yates, A.; Akanni, W.; Amode, M.R.; Barrell, D.; Billis, K.; Carvalho-Silva, D.; Cummins, C.; Clapham, P.; Fitzgerald, S.; Gil, L.; et al. Ensembl 2016. *Nucleic Acids Res.* **2016**, *44*, D710–D716, doi:10.1093/nar/gkv1157.

108. Jorgenson, E.; Sciortino, S.; Shen, L.; Ranatunga, D.; Hoffmann, T.; Kvale, M.; Banda, Y.; Kwok, P.-Y.; Walter, L.; Risch, N.; et al. B4-4: Genome-Wide Association Study of Macular Degeneration: Early Results from the Kaiser Permanente Research Program on Genes, Environment, and Health (RPGEH). *Clin. Med. Res.* **2013**, *11*, 146–147, doi:10.3121/cmr.2013.1176.b4-4.

109. Hoffmann, T.J.; Kvale, M.N.; Hesselson, S.E.; Zhan, Y.; Aquino, C.; Cao, Y.; Cawley, S.; Chung, E.; Connell, S.; Eshragh, J.; et al. Next generation genome-wide association tool: design and coverage of a high-throughput European-optimized SNP array. *Genomics* **2011**, *98*, 79–89, doi:10.1016/j.ygeno.2011.04.005.

110. Kvale, M.N.; Hesselson, S.; Hoffmann, T.J.; Cao, Y.; Chan, D.; Connell, S.; Croen, L.A.; Dispensa, B.P.; Eshragh, J.; Finn, A.; et al. Genotyping Informatics and Quality Control for 100,000 Subjects in the Genetic Epidemiology Research on Adult Health and Aging (GERA) Cohort. *Genetics* **2015**, *200*, 1051–1060, doi:10.1534/genetics.115.178905.

111. Hoffmann, T.J.; Van Den Eeden, S.K.; Sakoda, L.C.; Jorgenson, E.; Habel, L.A.; Graff, R.E.; Passarelli, M.N.; Cario, C.L.; Emami, N.C.; Chao, C.R.; et al. A large multiethnic genome-wide association study of prostate cancer identifies novel risk variants and substantial ethnic differences. *Cancer Discov.* **2015**, *5*, 878–891, doi:10.1158/2159-8290.CD-15-0315.

112. UK Biobank — Neale lab Available online: http://www.nealelab.is/uk-biobank (accessed on Jun 30, 2020).

113. PheWeb Available online: http://pheweb.sph.umich.edu (accessed on Jun 30, 2020).

114. Rapid GWAS of thousands of phenotypes for 337,000 samples in the UK Biobank — Neale lab Available online: http://www.nealelab.is/blog/2017/7/19/rapid-gwas-of-thousands-of-phenotypes-for-337000-samples-in-the-uk-biobank (accessed on Jun 30,

2020).

115. My.LocusZoom.org Available online: https://my.locuszoom.org/ (accessed on Jun 30, 2020).

116. Giambartolomei, C.; Vukcevic, D.; Schadt, E.E.; Franke, L.; Hingorani, A.D.; Wallace, C.; Plagnol, V. Bayesian test for colocalisation between pairs of genetic association studies using summary statistics. *PLoS Genet.* **2014**, *10*, e1004383, doi:10.1371/journal.pgen.1004383.

117. Data Showcase | UK Biobank Available online: https://www.ukbiobank.ac.uk/data-showcase/ (accessed on Jun 30, 2020).

118. Boyle, A.P.; Hong, E.L.; Hariharan, M.; Cheng, Y.; Schaub, M.A.; Kasowski, M.; Karczewski, K.J.; Park, J.; Hitz, B.C.; Weng, S.; et al. Annotation of functional variation in personal genomes using RegulomeDB. *Genome Res.* **2012**, *22*, 1790–1797, doi:10.1101/gr.137323.112.

119. Regulome search – Regulome Available online: https://www.regulomedb.org/regulome-search/ (accessed on Jul 20, 2020).

120. Online mendelian inheritance in man “OMIM” Available online: https://www.omim.org/ (accessed on Nov 13, 2020).

121. MGI-Mouse Genome Informatics Available online: http://www.informatics.jax.org/ (accessed on Nov 13, 2020).

122. Turley, P.; Walters, R.K.; Maghzian, O.; Okbay, A.; Lee, J.J.; Fontana, M.A.; Nguyen-Viet, T.A.; Wedow, R.; Zacher, M.; Furlotte, N.A.; et al. Multi-trait analysis of genome-wide association summary statistics using MTAG. *Nat. Genet.* **2018**, *50*, 229–237, doi:10.1038/s41588-017-0009-4.

123. Han, X.; Gharahkhani, P.; Mitchell, P.; Liew, G.; Hewitt, A.W.; MacGregor, S. Genome-wide meta-analysis identifies novel loci associated with age-related macular degeneration. *J. Hum. Genet.* **2020**, *65*, 657–665, doi:10.1038/s10038-020-0750-x.

124. Ghanbari, M.; Erkeland, S.J.; Xu, L.; Colijn, J.M.; Franco, O.H.; Dehghan, A.; Klaver, C.C.W.; Meester-Smoor, M.A. Genetic variants in microRNAs and their binding sites within gene 3′UTRs associate with susceptibility to age-related macular degeneration. *Hum. Mutat.* **2017**, *38*, 827–838, doi:10.1002/humu.23226.

125. Kiel, C.; Strunz, T.; International AMD Genomics Consortium Project Manager Susan Blanton IAMDGC; Grassmann, F.; Weber, B.H.F. Pleiotropic Locus 15q24.1 Reveals a Gender-Specific Association with Neovascular but Not Atrophic Age-Related Macular Degeneration (AMD). *Cells* **2020**, *9*, 2257, doi:10.3390/cells9102257.

126. International Consortium for Blood Pressure Genome-Wide Association Studies; Ehret, G.B.; Munroe, P.B.; Rice, K.M.; Bochud, M.; Johnson, A.D.; Chasman, D.I.; Smith, A. V; Tobin, M.D.; Verwoert, G.C.; et al. Genetic variants in novel pathways influence blood pressure and cardiovascular disease risk. *Nature* **2011**, *478*, 103–109, doi:10.1038/nature10405.

127. Bentham, J.; Morris, D.L.; Cunninghame Graham, D.S.; Pinder, C.L.; Tombleson, P.; Behrens, T.W.; Martín, J.; Fairfax, B.P.; Knight, J.C.; Chen, L.; et al. Genetic association

analyses implicate aberrant regulation of innate and adaptive immunity genes in the pathogenesis of systemic lupus erythematosus. *Nat. Genet.* **2015**, *47*, 1457–1464, doi:10.1038/ng.3434.

128. van der Harst, P.; Zhang, W.; Mateo Leach, I.; Rendon, A.; Verweij, N.; Sehmi, J.; Paul, D.S.; Elling, U.; Allayee, H.; Li, X.; et al. Seventy-five genetic loci influencing the human red blood cell. *Nature* **2012**, *492*, 369–375, doi:10.1038/nature11677.

129. Ghanbari, M.; de Vries, P.S.; de Looper, H.; Peters, M.J.; Schurmann, C.; Yaghootkar, H.; Dörr, M.; Frayling, T.M.; Uitterlinden, A.G.; Hofman, A.; et al. A genetic variant in the seed region of miR-4513 shows pleiotropic effects on lipid and glucose homeostasis, blood pressure, and coronary artery disease. *Hum. Mutat.* **2014**, *35*, 1524–1531, doi:10.1002/humu.22706.

130. Li, Q.; Chen, L.; Chen, D.; Wu, X.; Chen, M. Influence of microRNA-related polymorphisms on clinical outcomes in coronary artery disease. *Am. J. Transl. Res.* **2015**, *7*, 393–400.

131. Mir, R.; Jha, C.K. ; Elfaki, I.; Javid, J.; Rehman, S.; Khullar, N.; Banu, S.; Chahal, S.M.S. Incidence of MicroR-4513C/T Gene Variability in Coronary Artery Disease - A Case-Control Study. *Endocr. Metab. Immune Disord. Drug Targets* **2019**, *19*, 1216–1223, doi:10.2174/1871530319666190417111940.

132. Sudlow, C.; Gallacher, J.; Allen, N.; Beral, V.; Burton, P.; Danesh, J.; Downey, P.; Elliott, P.; Green, J.; Landray, M.; et al. UK biobank: an open access resource for identifying the causes of a wide range of complex diseases of middle and old age. *PLoS Med.* **2015**, *12*, e1001779, doi:10.1371/journal.pmed.1001779.

133. Tower, J. Sex-Specific Gene Expression and Life Span Regulation. *Trends Endocrinol. Metab.* **2017**, *28*, 735–747, doi:10.1016/j.tem.2017.07.002.

134. Strunz, T.; Kiel, C.; Grassmann, F.; Ratnapriya, R.; Kwicklis, M.; Karlstetter, M.; Fauser, S.; Arend, N.; Swaroop, A.; Langmann, T.; et al. A mega-analysis of expression quantitative trait loci in retinal tissue. *PLoS Genet.* **2020**, *16*, e1008934, doi:10.1371/journal.pgen.1008934.

135. Li, Y.; Zhu, H.; Wang, J.; Qian, X.; Li, N. miR-4513 promotes breast cancer progression through targeting TRIM3. *Am. J. Transl. Res.* **2019**, *11*, 2431–2438.

136. Ding, H.; Shi, Y.; Liu, X.; Qiu, A. MicroRNA-4513 Promotes Gastric Cancer Cell Proliferation and Epithelial–Mesenchymal Transition Through Targeting KAT6B. *Hum. Gene Ther. Clin. Dev.* **2019**, *30*, 142–148, doi:10.1089/humc.2019.094.

137. Zhu, M.; Wang, F.; Mi, H.; Li, L.; Wang, J.; Han, M.; Gu, Y. Long noncoding RNA MEG3 suppresses cell proliferation, migration and invasion, induces apoptosis and paclitaxel-resistance via miR-4513/PBLD axis in breast cancer cells. *Cell Cycle* **2020**, *19*, 3277–3288, doi:10.1080/15384101.2020.1839700.

138. Zhang, N.; Li, Y.; Zheng, Y.; Zhang, L.; Pan, Y.; Yu, J.; Yang, M. miR-608 and miR-4513 significantly contribute to the prognosis of lung adenocarcinoma treated with EGFR-TKIs. *Lab. Invest.* **2019**, *99*, 568–576, doi:10.1038/s41374-018-0164-y.

139. Choi, S.; Jahng, W.J.; Park, S.M.; Jee, D. Association of Age-Related Macular Degeneration on Alzheimer or Parkinson Disease: A Retrospective Cohort Study. *Am.*

J. Ophthalmol. **2020**, *210*, 41–47, doi:10.1016/j.ajo.2019.11.001.

140. Kaarniranta, K.; Salminen, A.; Haapasalo, A.; Soininen, H.; Hiltunen, M. Age-Related Macular Degeneration (AMD): Alzheimer's Disease in the Eye? *J. Alzheimers Dis.* **2011**, *24*, 615–631, doi:10.3233/JAD-2011-101908.

141. Kiel, C.; Weber, B.H.F.; Grassmann, F. Pleiotropic Effects of Risk Factors in Age-Related Macular Degeneration and Seemingly Unrelated Complex Diseases. *Adv. Exp. Med. Biol.* **2018**, 1074, 247–255, doi:10.1007/978-3-319-75402-4_30.

142. Cougnard-Grégoire, A.; Delyfer, M.-N.; Korobelnik, J.-F.; Rougier, M.-B.; Le Goff, M.; Dartigues, J.-F.; Barberger-Gateau, P.; Delcourt, C. Elevated high-density lipoprotein cholesterol and age-related macular degeneration: the Alienor study. *PLoS One* **2014**, *9*, e90973, doi:10.1371/journal.pone.0090973.

143. Colijn, J.M.; den Hollander, A.I.; Demirkan, A.; Cougnard-Grégoire, A.; Verzijden, T.; Kersten, E.; Meester-Smoor, M.A.; Merle, B.M.J.; Papageorgiou, G.; Ahmad, S.; et al. Increased High-Density Lipoprotein Levels Associated with Age-Related Macular Degeneration: Evidence from the EYE-RISK and European Eye Epidemiology Consortia. *Ophthalmology* **2019**, *126*, 393–406, doi:10.1016/j.ophtha.2018.09.045.

144. Zhang, M.; Jiang, N.; Chu, Y.; Postnikova, O.; Varghese, R.; Horvath, A.; Cheema, A.K.; Golestaneh, N. Dysregulated metabolic pathways in age-related macular degeneration. *Sci. Rep.* **2020**, *10*, 2464, doi:10.1038/s41598-020-59244-4.

145. Camelo, S. Potential Sources and Roles of Adaptive Immunity in Age-Related Macular Degeneration: Shall We Rename AMD into Autoimmune Macular Disease? *Autoimmune Dis.* **2014**, *2014*, 532487, doi:10.1155/2014/532487.

146. Cuenca, N.; Fernández-Sánchez, L.; Campello, L.; Maneu, V.; De la Villa, P.; Lax, P.; Pinilla, I. Cellular responses following retinal injuries and therapeutic approaches for neurodegenerative diseases. *Prog. Retin. Eye Res.* **2014**, *43*, 17–75, doi:10.1016/j.preteyeres.2014.07.001.

147. Biscetti, L.; Luchetti, E.; Vergaro, A.; Menduno, P.; Cagini, C.; Parnetti, L. Associations of Alzheimer's disease with macular degeneration. *Front. Biosci. (Elite Ed).* **2017**, *9*, 174–191, doi:10.2741/e794.

148. Logue, M.W.; Schu, M.; Vardarajan, B.N.; Farrell, J.; Lunetta, K.L.; Jun, G.; Baldwin, C.T.; DeAngelis, M.M.; Farrer, L.A. Search for age-related macular degeneration risk variants in Alzheimer disease genes and pathways. *Neurobiol. Aging* **2014**, *35*, 1510.e7-18, doi:10.1016/j.neurobiolaging.2013.12.007.

149. Hollingworth, P.; Harold, D.; Sims, R.; Gerrish, A.; Lambert, J.-C.; Carrasquillo, M.M.; Abraham, R.; Hamshere, M.L.; Pahwa, J.S.; Moskvina, V.; et al. Common variants at ABCA7, MS4A6A/MS4A4E, EPHA1, CD33 and CD2AP are associated with Alzheimer's disease. *Nat. Genet.* **2011**, *43*, 429–435, doi:10.1038/ng.803.

150. Lambert, J.C.; Ibrahim-Verbaas, C.A.; Harold, D.; Naj, A.C.; Sims, R.; Bellenguez, C.; DeStefano, A.L.; Bis, J.C.; Beecham, G.W.; Grenier-Boley, B.; et al. Meta-analysis of 74,046 individuals identifies 11 new susceptibility loci for Alzheimer's disease. *Nat. Genet.* **2013**, *45*, 1452–1458, doi:10.1038/ng.2802.

151. Aikawa, T.; Holm, M.L.; Kanekiyo, T. ABCA7 and Pathogenic Pathways of Alzheimer's

Disease. *Brain Sci.* **2018**, *8*, 27, doi:10.3390/brainsci8020027.

152. Dentchev, T.; Milam, A.H.; Lee, V.M.Y.; Trojanowski, J.Q.; Dunaief, J.L. Amyloid-beta is found in drusen from some age-related macular degeneration retinas, but not in drusen from normal retinas. *Mol. Vis.* **2003**, *9*, 184–90.

153. Hoh Kam, J.; Lenassi, E.; Jeffery, G. Viewing ageing eyes: diverse sites of amyloid Beta accumulation in the ageing mouse retina and the up-regulation of macrophages. *PLoS One* **2010**, *5*, e13127, doi:10.1371/journal.pone.0013127.

154. Artigas, M.S.; Loth, D.W.; Wain, L.V.; Gharib, S.A.; Obeidat, M.; Tang, W.; Zhai, G.; Zhao, J.H.; Smith, A.V.; Huffman, J.E.; et al. Genome-wide association and large-scale follow up identifies 16 new loci influencing lung function. *Nat. Genet.* **2011**, *43*, 1082–1090, doi:10.1038/ng.941.

155. Amundadottir, L.T. Pancreatic Cancer Genetics. *Int. J. Biol. Sci.* **2016**, *12*, 314–325, doi:10.7150/ijbs.15001.

156. Gormley, P.; Anttila, V.; Winsvold, B.S.; Palta, P.; Esko, T.; Pers, T.H.; Farh, K.-H.; Cuenca-Leon, E.; Muona, M.; Furlotte, N.A.; et al. Meta-analysis of 375,000 individuals identifies 38 susceptibility loci for migraine. *Nat. Genet.* **2016**, *48*, 856–866, doi:10.1038/ng.3598.

157. Bradfield, J.P.; Qu, H.-Q.; Wang, K.; Zhang, H.; Sleiman, P.M.; Kim, C.E.; Mentch, F.D.; Qiu, H.; Glessner, J.T.; Thomas, K.A.; et al. A genome-wide meta-analysis of six type 1 diabetes cohorts identifies multiple associated loci. *PLoS Genet.* **2011**, *7*, e1002293, doi:10.1371/journal.pgen.1002293.

158. Morris, A.P.; Voight, B.F.; Teslovich, T.M.; Ferreira, T.; Segrè, A.V.; Steinthorsdottir, V.; Strawbridge, R.J.; Khan, H.; Grallert, H.; Mahajan, A.; et al. Large-scale association analysis provides insights into the genetic architecture and pathophysiology of type 2 diabetes. *Nat. Genet.* **2012**, *44*, 981–990, doi:10.1038/ng.2383.

159. del Pilar Camacho Leal, M.; Sciortino, M.; Tornillo, G.; Colombo, S.; Defilippi, P.; Cabodi, S. p130Cas/BCAR1 scaffold protein in tissue homeostasis and pathogenesis. *Gene* **2015**, *562*, 1–7, doi:10.1016/j.gene.2015.02.027.

160. Riccomagno, M.M.; Sun, L.O.; Brady, C.M.; Alexandropoulos, K.; Seo, S.; Kurokawa, M.; Kolodkin, A.L. Cas adaptor proteins organize the retinal ganglion cell layer downstream of integrin signaling. *Neuron* **2014**, *81*, 779–786, doi:10.1016/j.neuron.2014.01.036.

161. Ratnapriya, R.; Acar, İ.E.; Geerlings, M.J.; Branham, K.; Kwong, A.; Saksens, N.T.M.; Pauper, M.; Corominas, J.; Kwicklis, M.; Zipprer, D.; et al. Family-based exome sequencing identifies rare coding variants in age-related macular degeneration. *Hum. Mol. Genet.* **2020**, *29*, 2022–2034, doi:10.1093/hmg/ddaa057.

162. GWAS Catalog Available online: https://www.ebi.ac.uk/gwas/ (accessed on Mar 12, 2021).

163. Eelen, G.; de Zeeuw, P.; Treps, L.; Harjes, U.; Wong, B.W.; Carmeliet, P. Endothelial Cell Metabolism. *Physiol. Rev.* **2018**, *98*, 3–58, doi:10.1152/physrev.00001.2017.

164. Xu, Y.; Guan, N.; Xu, J.; Yang, X.; Ma, K.; Zhou, H.; Zhang, F.; Snellingen, T.; Jiao, Y.;

Liu, X.; et al. Association of CFH, LOC387715, and HTRA1 polymorphisms with exudative age-related macular degeneration in a northern Chinese population. *Mol. Vis.* **2008**, *14*, 1373–1381.

165. GTEx Consortium; Aguet, F.; Barbeira, A.N.; Bonazzola, R.; Brown, A.; Castel, S.E.; Jo, B.; Kasela, S.; Kim-Hellmuth, S.; Liang, Y.; et al. The GTEx Consortium atlas of genetic regulatory effects across human tissues. *Science* **2020**, *369*, 1318–1330, doi:10.1126/science.aaz1776.

166. Gonzalez, F.J. Molecular genetics of the P-450 superfamily. *Pharmacol. Ther.* **1990**, *45*, 1–38, doi:10.1016/0163-7258(90)90006-n.

167. Shi, Z.; Dragin, N.; Gálvez-Peralta, M.; Jorge-Nebert, L.F.; Miller, M.L.; Wang, B.; Nebert, D.W. Organ-specific roles of CYP1A1 during detoxication of dietary benzo[a]pyrene. *Mol. Pharmacol.* **2010**, *78*, 46–57, doi:10.1124/mol.110.063438.

168. Jarrett, S.G.; Boulton, M.E. Consequences of oxidative stress in age-related macular degeneration. *Mol. Aspects Med.* **2012**, *33*, 399–417, doi:10.1016/j.mam.2012.03.009.

169. Esfandiary, H.; Chakravarthy, U.; Patterson, C.; Young, I.; Hughes, A.E. Association study of detoxification genes in age related macular degeneration. *Br. J. Ophthalmol.* **2005**, *89*, 470–474, doi:10.1136/bjo.2004.047340.

170. Perepechaeva, M.L.; Grishanova, A.Y.; Rudnitskaya, E.A.; Kolosova, N.G. The Mitochondria-Targeted Antioxidant SkQ1 Downregulates Aryl Hydrocarbon Receptor-Dependent Genes in the Retina of OXYS Rats with AMD-Like Retinopathy. *J. Ophthalmol.* **2014**, *2014*, 530943, doi:10.1155/2014/530943.

171. Kopf, P.G.; Scott, J.A.; Agbor, L.N.; Boberg, J.R.; Elased, K.M.; Huwe, J.K.; Walker, M.K. Cytochrome P4501A1 is required for vascular dysfunction and hypertension induced by 2,3,7,8-tetrachlorodibenzo-p-dioxin. *Toxicol. Sci.* **2010**, *117*, 537–546, doi:10.1093/toxsci/kfq218.

172. Raznahan, A.; Parikshak, N.N.; Chandran, V.; Blumenthal, J.D.; Clasen, L.S.; Alexander-Bloch, A.F.; Zinn, A.R.; Wangsa, D.; Wise, J.; Murphy, D.G.M.; et al. Sex-chromosome dosage effects on gene expression in humans. *Proc. Natl. Acad. Sci. U S A* **2018**, *115*, 7398–7403, doi:10.1073/pnas.1802889115.

173. Ma, Y. The Challenge of microRNA as a Biomarker of Epilepsy. *Curr. Neuropharmacol.* **2018**, *16*, 37-42, doi:10.2174/1570159X15666170703102410.

174. Fazmin, I.T.; Achercouk, Z.; Edling, C.E.; Said, A.; Jeevaratnam, K. Circulating microRNA as a Biomarker for Coronary Artery Disease. *Biomolecules* **2020**, *10*, 1354, doi:10.3390/biom10101354.

175. Condrat, C.E.; Thompson, D.C.; Barbu, M.G.; Bugnar, O.L.; Boboc, A.; Cretoiu, D.; Suciu, N.; Cretoiu, S.M.; Voinea, S.C. miRNAs as Biomarkers in Disease: Latest Findings Regarding Their Role in Diagnosis and Prognosis. *Cells* **2020**, *9*, 276, doi:10.3390/cells9020276.

176. Lambert, V.; Lecomte, J.; Hansen, S.; Blacher, S.; Gonzalez, M.-L.A.; Struman, I.; Sounni, N.E.; Rozet, E.; de Tullio, P.; Foidart, J.M.; et al. Laser-induced choroidal neovascularization model to study age-related macular degeneration in mice. *Nat. Protoc.* **2013**, *8*, 2197–2211, doi:10.1038/nprot.2013.135.

177. Ménard, C.; Wilson, A.M.; Dejda, A.; Miloudi, K.; Binet, F.; Crespo-Garcia, S.; Parinot, C.; Pilon, F.; Juneau, R.; Andriessen, E.M.; et al. miR-106b suppresses pathological retinal angiogenesis. *Aging (Albany NY).* **2020**, *12*, 24836–24852, doi:10.18632/aging.202404.

178. Wolf, A.; Herb, M.; Schramm, M.; Langmann, T. The TSPO-NOX1 axis controls phagocyte-triggered pathological angiogenesis in the eye. *Nat. Commun.* **2020**, *11*, 2709, doi:10.1038/s41467-020-16400-8.

179. Eissa, M.G.; Artlett, C.M. The MicroRNA miR-155 Is Essential in Fibrosis. *Noncoding RNA* **2019**, *5*, 23, doi:10.3390/ncrna5010023.

180. Michaille, J.-J.; Awad, H.; Fortman, E.C.; Efanov, A.A.; Tili, E. miR-155 expression in antitumor immunity: The higher the better? *Genes Chromosomes Cancer* **2019**, *58*, 208–218, doi:10.1002/gcc.22698.

181. Ding, E.; Guo, J.; Bai, Y.; Zhang, H.; Liu, X.; Cai, W.; Zhong, L.; Zhu, B. MiR-92a and miR-486 are potential diagnostic biomarkers for mercury poisoning and jointly sustain NF-κB activity in mercury toxicity. *Sci. Rep.* **2017**, *7*, 15980, doi:10.1038/s41598-017-13230-5.

182. Yang, S.; Sui, J.; Liu, T.; Wu, W.; Xu, S.; Yin, L.; Pu, Y.; Zhang, X.; Zhang, Y.; Shen, B.; et al. Expression of miR-486-5p and its significance in lung squamous cell carcinoma. *J. Cell. Biochem.* **2019**, *120*, 13912–13923, doi:10.1002/jcb.28665.

183. Wang, Z.; Zhang, J.; Zhang, S.; Yan, S.; Wang, Z.; Wang, C.; Zhang, X. MiR-30e and miR-92a are related to atherosclerosis by targeting ABCA1. *Mol. Med. Rep.* **2019**, *19*, 3298–3304, doi:10.3892/mmr.2019.9983.

184. Lückoff, A.; Caramoy, A.; Scholz, R.; Prinz, M.; Kalinke, U.; Langmann, T. Interferon-beta signaling in retinal mononuclear phagocytes attenuates pathological neovascularization. *EMBO Mol. Med.* **2016**, *8*, 670–678, doi:10.15252/emmm.201505994.

185. Wang, H.; Peng, R.; Wang, J.; Qin, Z.; Xue, L. Circulating microRNAs as potential cancer biomarkers: the advantage and disadvantage. *Clin. Epigenetics* **2018**, *10*, 59, doi:10.1186/s13148-018-0492-1.

186. Pereira, P.M.; Marques, J.P.; Soares, A.R.; Carreto, L.; Santos, M.A.S. MicroRNA expression variability in human cervical tissues. *PLoS One* **2010**, *5*, e11780, doi:10.1371/journal.pone.0011780.

187. Ludwig, N.; Leidinger, P.; Becker, K.; Backes, C.; Fehlmann, T.; Pallasch, C.; Rheinheimer, S.; Meder, B.; Stähler, C.; Meese, E.; et al. Distribution of miRNA expression across human tissues. *Nucleic Acids Res.* **2016**, *44*, 3865–3877, doi:10.1093/nar/gkw116.

188. Xu, W.; Zhou, Y.; Xu, G.; Geng, B.; Cui, Q. Transcriptome analysis reveals non-identical microRNA profiles between arterial and venous plasma. *Oncotarget* **2017**, *8*, 28471–28480, doi:10.18632/oncotarget.15310.

189. Nowakowski, T.J.; Rani, N.; Golkaram, M.; Zhou, H.R.; Alvarado, B.; Huch, K.; West, J.A.; Leyrat, A.; Pollen, A.A.; Kriegstein, A.R.; et al. Regulation of cell-type-specific transcriptomes by microRNA networks during human brain development. *Nat. Neurosci.*

2018, *21*, 1784–1792, doi:10.1038/s41593-018-0265-3.

190. Wang, N.; Zheng, J.; Chen, Z.; Liu, Y.; Dura, B.; Kwak, M.; Xavier-Ferrucio, J.; Lu, Y.-C.; Zhang, M.; Roden, C.; et al. Single-cell microRNA-mRNA co-sequencing reveals non-genetic heterogeneity and mechanisms of microRNA regulation. *Nat. Commun.* **2019**, *10*, 95, doi:10.1038/s41467-018-07981-6.

191. Ayaz, L.; Dinç, E. Evaluation of microRNA responses in ARPE-19 cells against the oxidative stress. *Cutan. Ocul. Toxicol.* **2018**, *37*, 121–126, doi:10.1080/15569527.2017.1355314.

192. Chen, Z.; Wen, L.; Martin, M.; Hsu, C.-Y.; Fang, L.; Lin, F.-M.; Lin, T.-Y.; Geary, M.J.; Geary, G.G.; Zhao, Y.; et al. Oxidative stress activates endothelial innate immunity via sterol regulatory element binding protein 2 (SREBP2) transactivation of microRNA-92a. *Circulation* **2015**, *131*, 805–814, doi:10.1161/CIRCULATIONAHA.114.013675.

193. Bonauer, A.; Carmona, G.; Iwasaki, M.; Mione, M.; Koyanagi, M.; Fischer, A.; Burchfield, J.; Fox, H.; Doebele, C.; Ohtani, K.; et al. MicroRNA-92a controls angiogenesis and functional recovery of ischemic tissues in mice. *Science* **2009**, *324*, 1710–1713, doi:10.1126/science.1174381.

194. Fujita, M.; Otani, H.; Iwasaki, M.; Yoshioka, K.; Shimazu, T.; Shiojima, I.; Tabata, Y. Antagomir-92a impregnated gelatin hydrogel microsphere sheet enhances cardiac regeneration after myocardial infarction in rats. *Regen. Ther.* **2016**, *5*, 9–16, doi:10.1016/j.reth.2016.04.002.

195. Kalinina, N.; Klink, G.; Glukhanyuk, E.; Lopatina, T.; Efimenko, A.; Akopyan, Z.; Tkachuk, V. miR-92a regulates angiogenic activity of adipose-derived mesenchymal stromal cells. *Exp. Cell Res.* **2015**, *339*, 61–66, doi:10.1016/j.yexcr.2015.10.007.

196. Zhang, L.; Zhou, M.; Qin, G.; Weintraub, N.L.; Tang, Y. MiR-92a regulates viability and angiogenesis of endothelial cells under oxidative stress. *Biochem. Biophys. Res. Commun.* **2014**, *446*, 952–958, doi:10.1016/j.bbrc.2014.03.035.

197. Hammond, S.M. An overview of microRNAs. *Adv. Drug Deliv. Rev.* **2015**, *87*, 3–14, doi:10.1016/j.addr.2015.05.001.

198. Serra, S.; Chetty, R. p16. *J. Clin. Pathol.* **2018**, *71*, 853–858, doi:10.1136/jclinpath-2018-205216.

199. Lin, Y.-C.; Diccianni, M.B.; Kim, Y.; Lin, H.-H.; Lee, C.-H.; Lin, R.-J.; Joo, S.H.; Li, J.; Chuang, T.-J.; Yang, A.-S.; et al. Human p16gamma, a novel transcriptional variant of p16(INK4A), coexpresses with p16(INK4A) in cancer cells and inhibits cell-cycle progression. *Oncogene* **2007**, *26*, 7017–7027, doi:10.1038/sj.onc.1210507.

200. Robertson, K.D.; Jones, P.A. Tissue-specific alternative splicing in the human INK4a/ARF cell cycle regulatory locus. *Oncogene* **1999**, *18*, 3810–3820, doi:10.1038/sj.onc.1202737.

201. Sherr, C.J. The INK4a/ARF network in tumour suppression. *Nat. Rev. Mol. Cell Biol.* **2001**, *2*, 731–737, doi:10.1038/35096061.

202. Krishnamurthy, J.; Torrice, C.; Ramsey, M.R.; Kovalev, G.I.; Al-Regaiey, K.; Su, L.; Sharpless, N.E. Ink4a/Arf expression is a biomarker of aging. *J. Clin. Invest.* **2004**, *114*,

1299–1307, doi:10.1172/JCI22475.

203. Naylor, R.M.; Baker, D.J.; van Deursen, J.M. Senescent cells: a novel therapeutic target for aging and age-related diseases. *Clin. Pharmacol. Ther.* **2013**, *93*, 105–116, doi:10.1038/clpt.2012.193.

204. Rentscher, K.E.; Carroll, J.E.; Repetti, R.L.; Cole, S.W.; Reynolds, B.M.; Robles, T.F. Chronic stress exposure and daily stress appraisals relate to biological aging marker p16INK4a. *Psychoneuroendocrinology* **2019**, *102*, 139–148, doi:10.1016/j.psyneuen.2018.12.006.

205. Tawarayama, H.; Feng, Q.; Murayama, N.; Suzuki, N.; Nakazawa, T. Cyclin-Dependent Kinase Inhibitor 2b Mediates Excitotoxicity-Induced Death of Retinal Ganglion Cells. *Invest. Opthalmol. Vis. Sci.* **2019**, *60*, 4479-4488, doi:10.1167/iovs.19-27396.

206. Machiela, M.J.; Chanock, S.J. LDlink: a web-based application for exploring population-specific haplotype structure and linking correlated alleles of possible functional variants. *Bioinformatics* **2015**, *31*, 3555–3557, doi:10.1093/bioinformatics/btv402.

207. LDlink | An Interactive Web Tool for Exploring Linkage Disequilibrium in Population Groups Available online: https://ldlink.nci.nih.gov/?tab=home (accessed on Jul 20, 2020).

List of abbreviations

Abbreviation	Meaning
µ	Micro
°C	Degree Celsius
3'-UTR	3'-untranslated region
ABCA7	ATP Binding Cassette Subfamily A Member 7
ACTB	β-Actin
AMD	Age-related macular degeneration
APS	Ammoniumpersulfate
ARMS2	Age-Related Maculopathy Susceptibility 2
ATP	Adenosintriphosphate
bp	Base pair
BCAR1	Breast Cancer Anti-Estrogen Resistance 1
C3	Complement C3
CDKN2A	Cyclin Dependent Kinase Inhibitor 2A
cDNA	Complementary DNA
CFH	Complement Factor H
CI	Confidence interval
cmiRNA	Circulating microRNA
CYP1A1	Cytochrome P450 Family 1 Subfamily A Member 1
cpm	Counts per million
Ct	Cycle threshold
DBP	Diastolic blood pressure
DMEM	Dulbecoco's modified eagle medium
DNA	Deoxyribonucleicacid
dNTP	Deoxynucleotidetriphosphate
DPBS	Dulbecco's phosphate buffered saline
E. coli	*Escherichia coli*
ECL	Enhanced chemiluminescence
EDTA	Ethylendiamintetraacetate
eQTL	Expression quantitative trait locus
et al.	et aliter (and others)
DMSO	Dimethylsulfoxide
FBS	Fetal bovine serum
FDR	False discovery rate
g	Gram
GA	Geographic atrophy
GERA	Genetic Epidemiology Research on Adult Health and Aging
GO	Gene Ontology
GTEx	Genotype-tissue expression project
GWAS	Genome-wide association study
h	Hour
HDL	High-density lipoprotein
HEK293T	Human embryonic kidney cells
HPRT1	Hypoxanthine Phosphoribosyltransferase 1
HSP90	Heat shock protein 90
HTRA1	High-Temperature Requirement A Serine Peptidase 1
HUVEC	Human umbilical vein endothelial cells
IAMDGC	International AMD Genomics Consortium
IPTG	Isopropyl-β-D-thiogalactopyranoside
L	Liter
LB	Lysogeny broth
LD	Linkage disequilibrium

LDL	Low-density lipoprotein
m	Milli
M	Molar
mAB	Monoclonal antibody
Mbp	Mega base pairs
MGI	Mouse Genome Informatics
min	Minute
miRNA	microRNA
mRNA	Messenger ribonucleicacid
MTAG	Multiple trait analysis of genome-wide association studies
n	Nano
NGS	Next generation sequencing
NV	Neovascularization
OCT	Optical coherence tomography
OMIM	Online Mendelian Inheritance in Man
OR	Odds ratio
p	Pico
pAB	Polyclonal antibody
PCR	Polymerase chain reaction
pre-miRNA	Precursor microRNA
pri-miRNA	Primary microRNA transcript
PVDF	Polyvinylidene difluoride
QC	Quality control
qRT-PCR	Quantitative reverse transcription polymerase chain reaction
RISC	RNA-induced silencing complex
RNA	Ribonucleicacid
RNA-Seq	Ribonucleicacid sequencing
RPGEH	Research Program on Genes, Environment and Health
RPE	Retinal pigment epithelium
rpm	Revolutions per minute
RT	Room temperature
s	Second
SBP	Systolic blood pressure
SD	Standard deviation
SDS	Sodium dodecyl sulfate
SE	Standard error
SOX9	SRY-Box Transcription Factor 9
SRY	Sex Determining Region Y
TBC1D4	TBC1 Domain Family Member 4
TBE	Tris Borat EDTA
TBS	Tris-buffered saline
TEMED	Tetramethylethylendiamine
TF	Transcription factor
TMM	Trimmed mean of M-values
Tris	Tris(hydroxymethyl)-aminomethan
TWAS	Transcriptome-wide association study
V	Volt
VEGFA	Vascular Endothelial Growth Factor A
X-Gal	5-Bromo-4-chloro-3-indoxyl-β-D-galactopyranoside
ZFX	Zing Finger Protein X-Linked

List of figures

Figure 1. Pathological findings in age-related macular degeneration (AMD). 6
Figure 2. Exemplary plot of a locus detected by a genome-wide association study (GWAS). 8
Figure 3. Cumulative GWAS and functional follow-up studies per year. 9
Figure 4. Previously investigated AMD-associated GWAS loci. 10
Figure 5. Schematic overview of different ways to characterize genetic associations. 12
Figure 6. Types of pleiotropy. 13
Figure 7. Biogenesis of microRNAs (miRNA). 15
Figure 8. Workflow of the study design for identification of circulating miRNAs (cmiRNA) in a mouse model of laser-induced NV. 59
Figure 9. Comparison of cmiRNA profiles in NGS data. 60
Figure 10. Comparison of slopes from differential expression models of day 3 and 14 samples compared with day 0 baseline controls and untreated control samples. 61
Figure 11. Validated cmiRNAs with a significant change in expression after laser-treatment in the qRT-PCR replication study. 62
Figure 12. Relative expression of two miRNAs identified in blood of laser-treated mice in ocular tissue. 63
Figure 13. Study design to identify pleiotropic effects of AMD-associated genes. 65
Figure 14. AMD-associated genes overlapping with GWAS loci. 65
Figure 15. Overlap of AMD-associated genes with GWAS loci of different phenotype groups. 66
Figure 16. Genome-wide association of rs2168518 with AMD. 69
Figure 17. Association of rs2168518 with AMD in male and female individuals. 71
Figure 18. Conditional analysis to dissolve the association signal at 15q24.1. 72
Figure 19. Schematic summary of pleiotropy analyses of rs2168518 in the UK Biobank data. 73
Figure 20. LocusZoom plots of association signals at 15q24.1. 75
Figure 21. Schematic overview of altered transcription factor (TF) binding sites at 15q24.1. 77
Figure 22. Schematic study design for identification of allele-specific target genes of rs2168518 in hsa-miR-4513. 78
Figure 23. Relative miRNA expression in HUVECs 48 h after transfection. 79
Figure 24. Allele-specific target genes of hsa-miR-4513. 80
Figure 25. Replication of allele-specific target genes *via* qRT-PCR. 81
Figure 26. Validation of allele-specific target genes on protein level by Western Blot analysis. 83
Figure 27. Schematic principle of the luciferase reporter assay. 84
Figure 28. Allele-specific binding sites in the 3'-UTR of allele-specific target genes of hsa-miR-4513. 85
Figure 29. Relative miRNA expression in human embryonic kidney (HEK293T) cells after co-transfection with a luciferase reporter vector. 86
Figure 30. Allele-specific binding of hsa-miR-4513 to the 3'UTR of target transcripts determined by luciferase reporter assay. 87
Figure 31. Allele-specific target genes related to phenotypes associated with hsa-miR-4513 or its seed polymorphism rs2168518 according to literature. 89

List of tables

Table 1. Escherichia coli (E. coli) strains used. 17
Table 2. Names and tissue of origin of cell lines used. 17
Table 3. List of cell culture media and supplements/additives used. 17
Table 4. Name, sequence and specification of oligonucleotides used as miRNA mimics for eukaryotic cell transfection. 18
Table 5. Name, sequence and application of oligonucleotides used for miRNA detection *via* quantitative reverse transcription PCR (qRT-PCR). 18
Table 6. Name, sequence and corresponding probe number for oligonucleotides used for qRT-PCR. 19
Table 7. Name, sequence and purpose of oligonucleotides used for PCR and sequencing reactions. 21
Table 8. List of expression constructs, application and source. 23
Table 9. Specifications of primary antibodies used for Western Blot. 24
Table 10. Specifications of secondary antibodies used for Western Blot. 25
Table 11. List of enzymes used. 25
Table 12. List of kit systems used. 25
Table 13. List of chemicals/reagents used. 26
Table 14. Composition of buffers and solutions used. 29
Table 15. List of consumables used. 30
Table 16. List of instruments used. 31
Table 17. List of software used. 34
Table 18. Composition of poly(A) tailing reaction mix. 38
Table 19. Composition of mixture for Universal RT oligonucleotide primer addition. 38
Table 20. Composition of complementary DNA (cDNA) synthesis reaction mix for polyA tailed miRNAs. 38
Table 21. Reaction mix for cDNA synthesis of mRNA. 39
Table 22. qRT-PCR conditions for miRNA detection. 39
Table 23. Composition of qRT-PCR reation mix for mRNA detection. 40
Table 24. qRT-PCR conditions for mRNA detection. 40
Table 25. Composition of acrylamide resolving gels. 41
Table 26. Composition of 3 % acrylamide stacking gels. 41
Table 27. 3‘-Untranslated regions (3‘-UTR) and their amplification conditions. 43
Table 28. PCR reaction mix with GoTaq® DNA polymerase. 43
Table 29. PCR reaction mix with Phusion™ High-Fidelity DNA polymerase. 44
Table 30. PCR reaction mix with GoTaq® Long PCR DNA polymerase. 44
Table 31. PCR conditions for PCR amplification with GoTaq® and Phusion™ DNA polymerases. 44
Table 32. PCR conditions for PCR amplification with GoTaq® Long PCR DNA polymerase. 45
Table 33. pGEM®-T vector ligation mix. 46
Table 34. Reaction mixture for Sanger sequencing. 47
Table 35. Thermocycler program for cycle sequencing. 47
Table 36. Mixture for restriction digestion of plasmid DNA. 48

List of tables

Table 37. Composition of Antarctic Phosphatase reaction mixture..... 48
Table 38. Reaction mixtures for ligation of 3'-UTRs into the luciferase reporter vector..... 49
Table 39. PCR reaction mix for colony PCR. 49
Table 40. Overview of phenotype groups..... 64
Table 41. AMD-associated genes overlapping with GWAS loci of more than one phenotype group (Table modified from Strunz et al., 2020 [83]). 67
Table 42. Association of rs2168518 with AMD subtypes in the IAMDGC dataset (Table modified from Kiel et al., 2020 [125]). 70

List of supplementary tables

Supplementary Table 1. Overview about phenotype groups (modified after Strunz et al., 2020 [83]). 124
Supplementary Table 2. Genetic variants in linkage disequilibrium (LD, $R^2 > 0.8$) with rs2168518 in Europeans (Table adopted from Kiel et al., 2020 [125]). 127
Supplementary Table 3. Circulating miRNAs (cmiRNA) detected in the initial next generation sequencing (NGS) analysis (Table modified from Kiel *et al.*, 2020 [91]). 128
Supplementary Table 4. Replication of cmiRNAs by qRT-PCR (Table modified from Kiel et al., 2020 [91]). 129
Supplementary Table 5. Expression of mmu-miR-486a-5p and mmu-miR-92a-3p in retina and RPE/choroid (Table modified from Kiel et al., 2020 [91]). 131
Supplementary Table 6. Association of rs2168518 in the UK Biobank genome-wide association study (GWAS) summary statistics (Table adopted from Kiel et al., 2020 [125]). 132
Supplementary Table 7. Allele-specific target genes of hsa-miR-4513-G (Table modified from Kiel et al., 2021 [95]). 134
Supplementary Table 8. Allele-specific target genes of hsa-miR-4513-A (Table modified from Kiel et al., 2021 [95]). 135
Supplementary Table 9. Replication of allele-specific target genes of hsa-miR-4513-A and hsa-miR-4513-G by qRT-PCR (Table modified from Kiel et al., 2021 [95]). 136
Supplementary Table 10. Biological and medical relevance of allele-specific target genes of hsa-miR-4513 (Table modified from Kiel et al., 2021 [95]). 138

Acknowledgements

My special thanks go to my supervisor Prof. Dr. Bernhard Weber for giving me the opportunity to work and grow on very different projects and for always fully supporting me. The numerous opportunities that have been revealed during this time, like participating and presenting my work on international meetings, as well as the supportive discussions have given me the chance to grow both professionally and personally.

I would like to thank my mentors Prof. Dr. Thomas Langmann and Prof. Dr. Gunter Meister for their advice and the critical discussions, as well as the successful cooperations.

I would like to thank Dr. Felix Grassmann for his guidance and full support. Our numerous discussions helped me solve many problems and revealed repeatedly new and interesting avenues.

In particular, I would like to thank Lisa Parakenings for her excellent technical support. Without your far-reaching assistance, it would not have been possible for me to carry out so many different projects at the same time.

I would like to say a big thank you to Dr. Tobias Strunz. We have become a great team over time and have implemented many interesting new projects together. The many discussions have always been helpful and have often revealed new perspectives.

A big thank you goes to Dr. Karolina Plößl for her numerous and diverse advice, no matter whether it was about lab work or proofreading. And of course, for the culinary pleasures at the joint lunches.

I would like to thank Patricia Berber very much for her support in our joint project, which definitely made it easier not to lose our sense of humor even in difficult phases.

A big thank you to all my colleagues at the Institute of Human Genetics for the great working atmosphere and all the support and advice of all kind.

I would like to say a special thank you to my family, my partner and my friends. Without your support I would never have come this far. The fact that you all celebrate successes with me and help me through difficult times means an incredible amount to me.

Supplements

Supplementary Table 1. Overview about phenotype groups (modified after Strunz et al., 2020 [83]**).**

Phenotype group	Phenotype	PMID of GWAS	Variants	Variants included in TWAS
Aging	Leukocyte telomere length	23535734	7	7
AMD	Age-related macular degeneration	26691988	52	52
Anthropometric traits	Body fat percentage	26833246	12	12
	Body mass index	25673413	97	81
	Height	20881960	180	177
	Waist-hip ratio	25673412	49	47
Autoimmune diseases	Self-reported allergies	23817569	16	16
	Crohn's disease	23128233	106	106
	Atopic dermatitis	26482879; 23727859	31	22
	Inflammatory bowel disease	23128233	117	116
	Multiple sclerosis	21833088	55	51
	Psoriasis	23143594	41	39
	Rheumatoid arthritis	24390342; 23143596	101	79
	Systemic lupus erythematosis	26502338	43	41
	Type 1 diabetes	21980299; 19430480; 18978792; 17632545; 17554260; 19966805	51	41
	Ulcerative colitis	23128233	74	73
Blood cell traits	Haemoglobin	23222517	20	20
	Mean cell haemoglobin	23222517	36	36
	Mean cell haemoglobin concentration	23222517	13	13
	Mean cell volume	23222517	43	43
	Mean platelet volume	22139419	29	29
	Packed cell volume	23222517	15	15
	Platelet count	22139419	56	55
	Red blood cell phenotypes	23222517	75	74
	Red blood cell count	23222517	26	25
Cancer	Basal cell carcinoma	27539887; 25855136; 21700618	35	34
	Breast cancer - max. beta	25751625	94	92
	Breast cancer - only BRC	25751625	94	83
	Chronic lymphocytic leukemia	23770605; 24292274	30	27
	Cutaneous malignant melanoma	21983785; 21983787; 26237428; 23455637	20	20
	Colorectal cancer	25990418; 23266556; 21655089	28	25
	Cutaneous squamous cell carcinoma	26829030; 27424798	14	12
	Breast cancer - estrogen receptor negative	25751625	79	15
	Breast cancer - estrogen receptor positive	25751625	79	46

	Multiple myeloma	27363682	17	17
	Pancreatic cancer	26929738	13	13
	Prostate cancer	25217961; 23535732; 19767753; 18264098; 21743467; 18264097; 19767754; 19767752; 17401366; 21743057; 18758462; 17603485; 23065704	100	80
Cardiovascular phenotypes	Coronary artery disease	23202125; 26343387	61	61
	Diastolic blood pressure	21909115	29	26
	General blood pressure	21909115	29	29
	Hypertension	21909115	29	11
	Systolic blood pressure	21909115	29	25
Eye phenotypes	Central corneal thickness	23291589	26	26
	Myopia	23468642	22	22
	Optic disc - Cup area	25631615	22	22
	Optic disc - Disc area	25631615	14	13
	Primary open-angled glaucoma	26752265	9	9
	Vertical cup-disc ratio	25241763	18	18
Immune-related phenotypes	C-reactive protein	21300955	18	18
	Immune cell count	25772697	1225	72
	Pro-imflammatory cell count	25772697	1225	57
Lifestyle	Educational attainment	27225129	74	74
	Morningness	27494321	22	20
Metabolic phenotypes	LEP - alkaline phosphatase	22001757	43	14
	LEP - alanine transaminase	22001757	43	4
	Bone mineral density - femoral neck	22504420	64	50
	Bone mineral density - lumbar spine	22504420	64	48
	Eye colour	18483556; 18488028; 17952075	6	6
	Fibrinogen concentration	26561523	41	40
	LEP - γ-glutamyl transferase	22001757	43	25
	Hair colour	18483556; 18488028; 17952075	10	10
	High-density lipoprotein	24097068	71	71
	Low-density lipoprotein	24097068	58	58
	Liver enzymes in plasma	22001757	43	42
	Pigmentation	18483556; 18488028; 17952075	12	12
	Serum calcium concentration	24068962	7	7
	Serum urate concentration	23263486	35	32
	Type 2 diabetes	24509480; 22885922	72	53
	Total cholesterol	24097068	74	74
	Triglycerides	24097068	40	39
	Circulating VEGF levels	26910538	10	10
	Vitamin D level	20541252	4	3
	Alzheimer's disease	24162737	21	20

Neurological diseases	Major depressive disorder	27479909	17	17
	Migraine	23793025; 27322543	53	39
	Parkinson's disease	25064009	32	29
	Schizophrenia	25056061	128	124
Organ function traits	estimated glomerular filtration rate of creatinine	26831199; 20383146	55	54
	forced expiratory volume in 1 second	26635082; 20010834; 21946350	37	12
	forced expiratory volume in 1 second/forced vital capacity	21946350; 26635082; 20010835; 20010834	45	29
	forced vital capacity	24929828; 26635082	10	9
	Lung function	21946350; 26635082; 24929828; 20010834; 20010835	75	48

PMID = PubMed Identifier; GWAS = Genome-wide association study; Variants = Number of genetic variants associated with the respective phenotype; TWAS = Transcriptome-wide association study; AMD = age-related macular degeneration.

Supplementary Table 2. Genetic variants in linkage disequilibrium (LD, R^2 > 0.8) with rs2168518 in Europeans (Table adopted from Kiel et al., 2020 [125]**).**

RS ID	Coordinates (GRCh37)	Alleles	MAF	Distance	R2	Correlated alleles
rs2472304	chr15:75044238	G/A	0.4006	-36840	0.8564	G=G,A=A
rs2470890	chr15:75047426	C/T	0.4036	-33652	0.8378	G=C,A=T
rs2960192	chr15:75049943	G/A	0.3986	-31135	0.8561	G=G,A=A
rs36117428	chr15:75050575	-/AA	0.4155	-30503	0.8181	G=-,A=AA
rs12903896	chr15:75052495	C/T	0.4046	-28583	0.8419	G=C,A=T
rs11072507	chr15:75054866	G/C	0.3976	-26212	0.8598	G=G,A=C
rs138783032	chr15:75057745	A/-	0.4016	-23333	0.8838	G=A,A=-
rs12903541	chr15:75059627	A/G	0.3887	-21451	0.8941	G=A,A=G
rs11632414	chr15:75061916	A/G	0.3936	-19162	0.9064	G=A,A=G
rs12909307	chr15:75061929	A/G	0.3936	-19149	0.9064	G=A,A=G
rs11072508	chr15:75062397	C/T	0.3946	-18681	0.9025	G=C,A=T
rs4886410	chr15:75065644	G/C	0.3867	-15434	1	G=G,A=C
rs12905199	chr15:75070196	A/G	0.3867	-10882	1	G=A,A=G
rs1378942	chr15:75077367	C/A	0.3867	-3711	1	G=C,A=A
rs1378941	chr15:75080150	C/A	0.3867	-928	1	G=C,A=A
rs2168518	chr15:75081078	G/A	0.3867	0	1	G=G,A=A
rs3784789	chr15:75082552	C/G	0.3867	1474	1	G=C,A=G
rs1378940	chr15:75083494	C/A	0.3867	2416	1	G=C,A=A
rs62006566	chr15:75086534	C/T	0.3976	5456	0.947	G=C,A=T
rs62006567	chr15:75086545	C/T	0.3976	5467	0.947	G=C,A=T
rs12898997	chr15:75090349	C/T	0.3956	9271	0.955	G=C,A=T
rs35206230	chr15:75097780	C/T	0.3956	16702	0.955	G=C,A=T
rs34862454	chr15:75101530	C/T	0.3956	20452	0.955	G=C,A=T
rs12591513	chr15:75102714	G/A	0.3956	21636	0.955	G=G,A=A
rs12594062	chr15:75102851	T/C	0.3956	21773	0.955	G=T,A=C
rs11630478	chr15:75102923	G/T	0.3956	21845	0.955	G=G,A=T
rs11636952	chr15:75114322	T/C	0.3698	33244	0.8353	G=T,A=C

MAF = Minor allele frequency, distance = distance to rs2168518 in base pairs. Data was extracted with the LDproxy tool from LDlink [206,207] for rs2168518 as reference variant.

Supplementary Table 3. Circulating miRNAs (cmiRNA) detected in the initial next generation sequencing (NGS) analysis (Table modified from Kiel *et al.*, 2020 [91]**).**

		Comparison with day 0			Comparison with untreated controls		
		Slope	**95% CI**	**p-value**	**Slope**	**95% CI**	**p-value**
Day 0 vs day 3 candidates	mmu-miR-148b-5p	-0.523	NA	0.027	-0.360	-0.774-0.055	0.081
	mmu-miR-18a-3p	-1.028	NA	0.015	-1.134	-2.064--0.204	0.022
	mmu-miR-20a-5p	0.402	0.005-0.799	0.048	0.346	-0.13-0.822	0.134
	mmu-miR-298-5p	-0.821	-1.543--0.099	0.033	-0.559	-1.556-0.439	0.237
	mmu-miR-326-3p	-0.747	-1.041--0.453	0.001	*Previously excluded*		
	mmu-miR-449a-5p	1.623	0.44-2.805	0.017	0.743	-0.449-1.934	0.192
	mmu-miR-486a-5p	-1.053	-2.068--0.037	0.045	-1.186	-2.534-0.162	0.078
	mmu-miR-92a-3p	-0.517	-0.944--0.091	0.026	-0.534	-1.051--0.016	0.045
Day 0 vs day 14 candidates	mmu-let-7i-3p	1.251	0.071-2.43	0.041	1.164	0.166-2.163	0.027
	mmu-miR-148b-5p	-0.602	-1.128--0.076	0.032	-0.439	-1.038-0.16	0.132
	mmu-miR-155-5p	0.628	0.211-1.045	0.012	0.372	-0.104-0.847	0.111
	mmu-miR-15b-3p	0.438	0.004-0.872	0.049	0.198	-0.255-0.65	0.350
	mmu-miR-1964-3p	0.763	0.049-1.477	0.040	0.011	-0.866-0.887	0.979
	mmu-miR-301b-3p	-1.112	-2.124--0.1	0.037	-0.159	-1.626-1.308	0.812
	mmu-miR-503-5p	-1.047	-1.891--0.202	0.024	-0.090	-1.429-1.249	0.882

CmiRNA profiles of laser-treated mice on day 3 or day 14 were compared with day 0 (baseline) samples by applying a linear mixed effects model. CmiRNA fitting the following criteria were selected for further investigation: p-value < 0.05 and absolute slope > 0.4. Afterwards, expression of selected cmiRNAs was compared between day 0 baseline samples and untreated control samples in a Firth's bias-reduced logistic regression model (p-value < 0.05, absolute slope > 0.4). mmu-miR-326-3p was differentially expressed between the two control groups and therefore excluded from further analysis. The remaining cmiRNAs were tested in comparison with the untreated control samples by a linear fixed effects model. Candidates were regarded as valid if the slope indicates in the same direction as in the comparison with the day 0 samples and if the absolute slope was above 0.2. CmiRNAs not reaching these criteria were excluded from further analysis and displayed in grey. CI = Confidence interval.

Supplementary Table 4. Replication of cmiRNAs by qRT-PCR (Table modified from Kiel et al., 2020 [91]**).**

		batch 1				batch 2				combined			
		n	**Slope**	**95% CI**	**p-value**	**n**	**Slope**	**95% CI**	**p-value**	**n**	**Slope**	**95% CI**	**p-value**
Day 0 vs day 3	mmu-miR-148b-5p	12	0.027	-0.056-0.111	0.438	18	-0.093	-0.284-0.097	0.276	30	-0.045	-0.152-0.063	0.389
	mmu-miR-18a-3p	12	-0.048	-0.231-0.135	0.532	8	-0.048			20	-0.048	*-0.182-0.086*	0.51
	mmu-miR-20a-5p	12	0.21	*0.047-0.372*	0.053	14	-0.196	-0.784-0.391	0.365	26	-0.007	-0.261-0.248	0.906
	mmu-miR-298-5p	12	-0.062	-0.145-0.02	0.11	17	0.017	-0.128-0.161	0.788	29	-0.018	-0.097-0.06	0.6
	mmu-miR-449a-5p	12	-0.007	-0.25-0.237	0.946	9	0.071	-0.553-0.695	0.672	21	0.018	-0.175-0.211	0.967
	mmu-miR-486a-5p	12	-0.193	-0.313--0.073	**0.009**	17	-0.263	-0.54-0.015	0.059	29	-0.233	-0.373--0.094	**0.003**
	mmu-miR-92a-3p	12	-0.12	-0.228--0.011	**0.036**	18	-0.034	-0.127-0.059	0.407	30	-0.072	-0.137--0.006	**0.032**
	mmu-let-7i-3p	12	-0.047	*-0.121-0.027*	0.265	14	-0.224	-0.613-0.165	0.164	26	-0.134	-0.285-0.018	0.07
	mmu-miR-155-5p	12	-0.026	*-0.141-0.089*	0.679	16	-0.023	-0.224-0.177	0.761	28	-0.02	-0.141-0.101	0.666
Day 0 vs day 7	mmu-miR-148b-5p	12	0.049	-0.006-0.103	0.071	19	-0.043	-0.122-0.035	0.234	31	-0.007	-0.06-0.045	0.794
	mmu-miR-18a-3p	12	-0.031	-0.098-0.035	0.282	11	-0.037	-0.716-0.641	0.61	23	-0.034	*-0.088-0.020*	0.278
	mmu-miR-20a-5p	12	0.152	0.06-0.243	**0.008**	17	-0.044	-0.19-0.102	0.489	29	0.034	-0.064-0.132	0.461
	mmu-miR-298-5p	12	-0.041	-0.089-0.007	0.077	18	0.002	*-0.068-0.071*	0.962	30	-0.015	*-0.060-0.029*	0.513
	mmu-miR-449a-5p	12	0.002	-0.089-0.093	0.956	10	0.458	-2.364-3.28	0.287	22	0.2	-0.069-0.469	0.161
	mmu-miR-486a-5p	12	-0.098	*-0.164--0.032*	**0.033**	20	-0.064	-0.129-0.001	0.054	32	-0.077	-0.126--0.027	**0.005**
	mmu-miR-92a-3p	12	-0.074	-0.14--0.009	**0.033**	19	0.032	-0.049-0.113	0.377	31	-0.009	-0.065-0.048	0.707
	mmu-let-7i-3p	12	-0.047	*-0.080-0.014*	**0.037**	18	-0.083	*-0.175-0.009*	0.12	30	-0.069	-0.131--0.006	**0.039**
	mmu-miR-155-5p	12	-0.04	-0.136-0.056	0.334	18	0.17	-0.046-0.385	0.103	30	0.082	-0.047-0.21	0.191
Day 0 vs day 14	mmu-miR-148b-5p	12	0.009	-0.014-0.032	0.35	20	-0.021	*-0.051-0.010*	0.215	32	-0.01	*-0.030-0.011*	0.378
	mmu-miR-18a-3p	12	0.002	-0.078-0.083	0.944	8	0.044			20	0.019	-0.037-0.074	0.438
	mmu-miR-20a-5p	12	0.135	-0.112-0.382	0.22	18	-0.009	-0.09-0.072	0.801	30	0.05	-0.049-0.148	0.304
	mmu-miR-298-5p	12	-0.017	-0.038-0.004	0.088	17	0.049	0.017-0.08	**0.009**	29	0.018	-0.013-0.049	0.254
	mmu-miR-449a-5p	12	-0.007	*-0.038-0.023*	0.655	9	-0.094	-0.104--0.083	**0.006**	21	-0.009	*-0.043-0.024*	0.521

mmu-miR-486a-5p	12	-0.034	-0.075-0.008	0.091	20	-0.025	*-0.076-0.026*	0.367	32	-0.028	-0.065-0.009	0.124
mmu-miR-92a-3p	12	-0.029	-0.054--0.004	**0.033**	20	0.017	-0.009-0.044	0.175	32	-0.001	-0.022-0.02	0.923
mmu-let-7i-3p	12	-0.009	-0.033-0.014	0.363	17	-0.044	-0.107-0.02	0.136	29	-0.03	*0.059-0.000*	0.082
mmu-miR-155-5p	12	0.03	*-0.015-0.075*	0.245	15	0.085	-0.008-0.179	0.064	27	0.059	0.012-0.106	**0.023**

CmiRNAs identified in the NGS analysis were independently replicated by qRT-PCR in two independent batches of laser-treated mice. Blood samples were taken on day 0 for baseline cmiRNA expression and on day 3, 7 and 14. A linear mixed effects model was applied to detect statistical differences in expression. CmiRNAs which did not replicate their effect direction from the NGS analysis were excluded from further analysis (displayed in grey). 95% confidence intervals (CI) in italic could not be defined by the model and were therefore estimated using beta estimate and SE. Significant p-values are indicated in bold (p-value < 0.05). n = sample size.

Supplementary Table 5. Expression of mmu-miR-486a-5p and mmu-miR-92a-3p in retina and RPE/choroid (Table modified from Kiel et al., 2020 [91]**).**

		Control vs. day 3					Control vs. day 7					Control vs. day 14				
		n	**Slope**	**95% CI**	**p-value**	**q-value**	**n**	**Slope**	**95% CI**	**p-value**	**q-value**	**n**	**Slope**	**95% CI**	**p-value**	**q-value**
Retina	mmu-miR-486a-5p	24	-0.004	-0.127-0.119	0.942	0.942	24	0.011	-0.132-0.153	0.877	0.877	24	0.046	-0.131-0.223	0.591	0.712
	mmu-miR-92a-3p	24	-0.058	-0.17-0.054	0.290	0.581	24	0.019	-0.13-0.167	0.797	0.877	24	0.023	-0.106-0.152	0.712	0.712
RPE/choroid	mmu-miR-486a-5p	24	0.408	0.188-0.628	0.001	**0.002**	24	0.060	-0.048-0.168	0.257	0.257	22	0.062	0.012-0.111	0.017	**0.019**
	mmu-miR-92a-3p	24	0.196	0.023-0.369	0.028	**0.028**	24	0.332	0.073-0.59	0.015	**0.029**	22	0.466	0.084-0.848	0.019	**0.019**

Expression of cmiRNAs identified in blood of laser treated mice were investigated in ocular tissue of laser treated mice, including retina and RPE/choroid. A linear regression model was applied to detect expression differences between samples of day 3, 7 or 14 and untreated control individuals, followed by a FDR correction. Q-values < 0.05 are regarded as significant (highlighted in bold). n = sample size, CI = Confidence interval.

Supplementary Table 6. Association of rs2168518 in the UK Biobank genome-wide association study (GWAS) summary statistics (Table adopted from Kiel et al., 2020 [125]**).**

	PheWeb association	**Summary statistics association**			**Coloc probability with AMD (IAMDGC)**	
UK Biobank phenotype	**p-value**	**Gender**	**p-value**	**Gender specificity**	**Same signal**	**Two signals**
Diastolic blood pressure, automated reading	**1.5×10^{-23}**	both sexes	**2.3×10^{-27}**	no	0.604	0.385
		female	**7.3×10^{-18}**		**0.964**	0.035
		male	**2.6×10^{-11}**		0.610	0.379
Vascular/heart problems diagnosed by doctor: high blood pressure	**7.2×10^{-23}**	both sexes	**2.2×10^{-26}**	no	**0.976**	0.024
		female	**2.9×10^{-14}**		**0.918**	0.079
		male	**9.9×10^{-14}**		**0.970**	0.029
Vascular/heart problems diagnosed by doctor: none of the above	**2.6×10^{-21}**	both sexes	**2.8×10^{-25}**	no	**0.970**	0.029
		female	**9.1×10^{-14}**		**0.860**	0.136
		male	**4.1×10^{-13}**		**0.969**	0.030
Non-cancer illness code, self-reported: hypertension	**2.7×10^{-21}**	both sexes	**2.2×10^{-24}**	no	**0.975**	0.024
		female	**3.2×10^{-13}**		**0.936**	0.062
		male	**9.1×10^{-13}**		**0.965**	0.034
Systolic blood pressure, automated reading	**1.6×10^{-11}**	both sexes	**9.3×10^{-14}**	no	0.735	0.258
		female	**1.1×10^{-10}**		**0.969**	0.030
		male	7.7×10^{-05}		0.428	0.523
Medication for cholesterol, blood pressure or diabetes: blood pressure medication	**6.3×10^{-11}**	male	**3.6×10^{-12}**		**0.938**	0.061
Medication for cholesterol, blood pressure, diabetes, or take exogenous hormones: blood pressure medication	**3.9×10^{-10}**	female	**8.6×10^{-12}**		**0.890**	0.106
Creatinine (enzymatic) in urine	**5.3×10^{-09}**	both sexes	2.9×10^{-07}	no	0.037	**0.936**
		female	8.9×10^{-08}		0.038	**0.934**
		male	0.031		0.037	**0.936**
Treatment/medication code: ramipril	7.4×10^{-08}	both sexes	8.0×10^{-08}	yes, only in male	**0.964**	0.035
		female	0.103		0.034	0.067
		male	**4.0×10^{-08}**		**0.898**	0.099
Treatment/medication code: bendroflumethiazide	1.2×10^{-07}	both sexes	5.3×10^{-08}	no	**0.948**	0.051
		female	9.6×10^{-06}		**0.901**	0.080
		male	1.4×10^{-03}		0.486	0.085

Medication for cholesterol, blood pressure or diabetes: none of the above	1.3×10^{-07}	male	**1.2×10^{-08}**		**0.830**	0.165
Hearing difficulty/problems with background noise	4.1×10^{-06}	both sexes	1.4×10^{-06}	yes, only in female	**0.917**	0.079
		female	**6.0×10^{-09}**		**0.966**	0.033
		male	0.345		0.007	0.062
Birth weight of first child	1.2×10^{-05}	female	2.5×10^{-05}		0.785	0.175
Mineral and other dietary supplements: glucosamine	2.5×10^{-05}	both sexes	3.6×10^{-05}	no	**0.877**	0.068
		female	9.4×10^{-03}		0.118	0.098
		male	8.2×10^{-04}		0.469	0.056
Sodium in urine	7.2×10^{-05}	both sexes	8.4×10^{-04}	no	0.037	**0.935**
		female	1.6×10^{-03}		0.037	**0.935**
		male	0.106		0.010	0.300
Eye problems/disorders: macular degeneration	5.1×10^{-03}	both sexes	2.7×10^{-03}			
		female	0.157			
		male	2.8×10^{-03}			

The PheWeb browser [113] containing GWAS summary statistics of the UK Biobank data [132] was searched to investigate a potential pleiotropic effect of rs2168518. Fifteen phenotypes displayed a significant association with rs2168518 (p-value < 1×10^{-04}), of which eight reached genome-wide significance (p-value < 5×10^{-08}). The association of rs2168518 with “Eye problems/disorders: macular degeneration” failed to reach statistical significance. Publicly available GWAS summary statistics of the UK Biobank data [112] were screened for gender specific association signals and gender specificity was determined by colocalization (probability > 0.8 in one gender). To investigate whether the association signal of the respective phenotype corresponds to the same association signal as AMD in the IAMDGC dataset [20] (both sexes combined) a colocalization analysis was applied. Coloc probabilities for “same signal” indicate that the same genetic signal underlies the association of the respective phenotype and AMD. In contrast, coloc probabilities for “two signals” indicate that different genetic signals are responsible for the respective association signals. Genome-wide association p-values (p-value < 5×10^{-08}) are indicated in bold, as well as coloc probabilities > 0.8.

Supplementary Table 7. Allele-specific target genes of hsa-miR-4513-G (Table modified from Kiel et al., 2021 [95]**).**

		hsa-miR-4513-G vs cel-miR-39			hsa-miR-4513-A vs hsa-miR-4513-G		
Gene ID	**Gene symbol**	**Slope [95% CI]**	**p-value**	**q-value**	**Slope [95% CI]**	**p-value**	**q-value**
ENSG00000178878	*APOLD1*	-0.498 [-0.608 - -0.388]	4.12×10^{-07}	1.82×10^{-03}	0.308 [0.185 - 0.432]	1.46×10^{-04}	7.98×10^{-03}
ENSG00000127022	*CANX*	-0.209 [-0.275 - -0.143]	1.62×10^{-05}	5.50×10^{-03}	0.199 [0.119 - 0.279]	1.62×10^{-04}	8.47×10^{-03}
ENSG00000148730	*EIF4EBP2*	-0.224 [-0.293 - -0.154]	1.39×10^{-05}	5.39×10^{-03}	0.21 [0.149 - 0.271]	7.26×10^{-06}	2.34×10^{-03}
ENSG00000163430	*FSTL1*	-0.386 [-0.5 - -0.272]	8.62×10^{-06}	4.21×10^{-03}	0.408 [0.271 - 0.544]	2.92×10^{-05}	3.89×10^{-03}
ENSG00000205730	*ITPRIPL2*	-0.374 [-0.506 - -0.243]	4.51×10^{-05}	8.89×10^{-03}	0.183 [0.116 - 0.25]	6.56×10^{-05}	5.58×10^{-03}
ENSG00000180398	*MCFD2*	-0.249 [-0.322 - -0.175]	8.43×10^{-06}	4.21×10^{-03}	0.224 [0.149 - 0.299]	3.04×10^{-05}	3.89×10^{-03}
ENSG00000071073	*MGAT4A*	-0.194 [-0.261 - -0.127]	3.99×10^{-05}	8.74×10^{-03}	0.275 [0.16 - 0.391]	2.23×10^{-04}	9.98×10^{-03}
ENSG00000095303	*PTGS1*	-0.29 [-0.361 - -0.218]	1.37×10^{-06}	2.35×10^{-03}	0.282 [0.196 - 0.369]	1.24×10^{-05}	2.88×10^{-03}
ENSG00000153707	*PTPRD*	-0.316 [-0.412 - -0.221]	1.08×10^{-05}	4.99×10^{-03}	0.165 [0.096 - 0.234]	2.26×10^{-04}	9.98×10^{-03}
ENSG00000174136	*RGMB*	-0.292 [-0.388 - -0.195]	2.59×10^{-05}	6.43×10^{-03}	0.229 [0.14 - 0.318]	1.12×10^{-04}	7.05×10^{-03}
ENSG00000163946	*TASOR*	-0.291 [-0.389 - -0.193]	3.06×10^{-05}	7.11×10^{-03}	0.223 [0.137 - 0.308]	1.03×10^{-04}	6.75×10^{-03}
ENSG00000131374	*TBC1D5*	-0.429 [-0.53 - -0.329]	7.58×10^{-07}	1.82×10^{-03}	0.294 [0.199 - 0.389]	2.08×10^{-05}	3.24×10^{-03}
ENSG00000140262	*TCF12*	-0.38 [-0.48 - -0.28]	2.69×10^{-06}	3.18×10^{-03}	0.282 [0.208 - 0.357]	2.84×10^{-06}	1.46×10^{-03}
ENSG00000100991	*TRPC4AP*	-0.348 [-0.445 - -0.252]	4.37×10^{-06}	3.93×10^{-03}	0.375 [0.231 - 0.52]	1.05×10^{-04}	6.75×10^{-03}
ENSG00000105939	*ZC3HAV1*	-0.199 [-0.27 - -0.128]	5.41×10^{-05}	9.98×10^{-03}	0.178 [0.118 - 0.239]	3.48×10^{-05}	4.07×10^{-03}

Allele-specific target genes of hsa-miR-4513-G identified in the RNA-Seq data had to fulfill the following criteria: significantly decreased expression in hsa-miR-4513-G samples in comparison to the control samples cel-miR-39 and a significantly altered expression between hsa-miR-4513-A and hsa-miR-4513-G samples (both q-values < 0.01). The slope of the hsa-miR-4513-A vs hsa-miR-4513-G comparison indicate how hsa-miR-4513-A behaves in comparison to hsa-miR-4513-G. CI = confidence interval.

Supplementary Table 8. Allele-specific target genes of hsa-miR-4513-A (Table modified from Kiel et al., 2021 [95]**).**

		hsa-miR-4513-A vs cel-miR-39			hsa-miR-4513-A vs hsa-miR-4513-G		
Gene ID	**Gene symbol**	**Slope [95% CI]**	**p-value**	**q-value**	**Slope [95% CI]**	**p-value**	**q-value**
ENSG00000169217	*CD2BP2*	-0.314 [-0.404 - -0.225]	5.91×10^{-06}	5.62×10^{-03}	-0.326 [-0.405 - -0.247]	1.16×10^{-06}	1.03×10^{-03}
ENSG00000147889	*CDKN2A*	-0.793 [-1.073 - -0.513]	4.75×10^{-05}	9.00×10^{-03}	-0.84 [-1.061 - -0.618]	2.68×10^{-06}	1.43×10^{-03}
ENSG00000145833	*DDX46*	-0.307 [-0.418 - -0.197]	5.58×10^{-05}	9.48×10^{-03}	-0.295 [-0.411 - -0.18]	1.22×10^{-04}	7.31×10^{-03}
ENSG00000122034	*GTF3A*	-0.122 [-0.166 - -0.078]	5.74×10^{-05}	9.48×10^{-03}	-0.158 [-0.216 - -0.1]	6.52×10^{-05}	5.58×10^{-03}
ENSG00000067082	*KLF6*	-0.19 [-0.251 - -0.129]	1.83×10^{-05}	6.12×10^{-03}	-0.169 [-0.213 - -0.125]	2.26×10^{-06}	1.30×10^{-03}
ENSG00000071054	*MAP4K4*	-0.247 [-0.33 - -0.164]	2.93×10^{-05}	7.14×10^{-03}	-0.184 [-0.249 - -0.118]	5.21×10^{-05}	5.29×10^{-03}
ENSG00000025796	*SEC63*	-0.268 [-0.336 - -0.2]	1.78×10^{-06}	2.97×10^{-03}	-0.201 [-0.251 - -0.151]	1.50×10^{-06}	1.03×10^{-03}
ENSG00000143549	*TPM3*	-0.202 [-0.264 - -0.14]	1.20×10^{-05}	5.62×10^{-03}	-0.216 [-0.267 - -0.165]	8.69×10^{-07}	1.03×10^{-03}

Allele-specific target genes of hsa-miR-4513-A identified in the RNA-Seq data had to fulfill the following criteria: significantly decreased expression in hsa-miR-4513-A samples in comparison to the control samples cel-miR-39 and a significantly altered expression between hsa-miR-4513-A and hsa-miR-4513-G samples (both q-values < 0.01). The slope of the hsa-miR-4513-A vs hsa-miR-4513-G comparison indicate how hsa-miR-4513-A behaves in comparison to hsa-miR-4513-G. CI = confidence interval.

Supplementary Table 9. Replication of allele-specific target genes of hsa-miR-4513-A and hsa-miR-4513-G by qRT-PCR (Table modified from Kiel et al., 2021 [95]**).**

				hsa-miR-4513-G vs cel-miR-39		hsa-miR-4513-A vs cel-miR-39		hsa-miR-4513-A vs hsa-miR-4513-G	
	Gene ID	**Gene symbol**	**Kruskal-Wallis p-value**	**p-value**	**Adjusted p-value**	**p-value**	**Adjusted p-value**	**p-value**	**Adjusted p-value**
A allele candidate	ENSG00000169217	*CD2BP2*	6.07×10^{-03}	0.093	0.140	1.40×10^{-03}	**4.21×10^{-03}**	0.130	0.130
	ENSG00000147889	*CDKN2A*	4.99×10^{-04}	0.051	0.051	9.64×10^{-05}	**2.89×10^{-04}**	0.051	0.077
	ENSG00000145833	*DDX46*	2.31×10^{-03}	0.159	0.159	5.32×10^{-04}	**1.59×10^{-03}**	0.040	0.060
	ENSG00000122034	*GTF3A*	1.20×10^{-02}	0.330	0.330	3.48×10^{-03}	**0.010**	0.051	0.077
	ENSG00000067082	*KLF6*	4.11×10^{-03}	0.136	0.136	9.22×10^{-04}	**2.77×10^{-03}**	0.059	0.088
	ENSG00000071054	*MAP4K4*	1.65×10^{-03}	0.020	**0.030**	4.34×10^{-04}	**1.30×10^{-03}**	0.234	0.234
	ENSG00000025796	*SEC63*	9.47×10^{-03}	0.066	0.099	2.45×10^{-03}	**7.34×10^{-03}**	0.234	0.234
	ENSG00000143549	*TPM3*	5.26×10^{-03}	0.492	0.492	1.87×10^{-03}	**5.60×10^{-03}**	0.014	**0.021**
G allele candidate	ENSG00000178878	*APOLD1*	2.87×10^{-03}	9.14×10^{-04}	**2.74×10^{-03}**	0.020	**0.030**	0.401	0.401
	ENSG00000127022	*CANX*	0.058	*not tested*		*not tested*		*not tested*	
	ENSG00000148730	*EIF4EBP2*	0.055	*not tested*		*not tested*		*not tested*	
	ENSG00000163430	*FSTL1*	2.74×10^{-03}	1.17×10^{-03}	**3.51×10^{-03}**	9.41×10^{-03}	**0.014**	0.516	0.516
	ENSG00000205730	*ITPRIPL2*	8.42×10^{-04}	1.75×10^{-04}	**5.25×10^{-04}**	0.034	0.051	0.103	0.103
	ENSG00000180398	*MCFD2*	2.61×10^{-03}	1.05×10^{-03}	**3.15×10^{-03}**	0.010	**0.015**	0.481	0.481
	ENSG00000071073	*MGAT4A*	2.32×10^{-03}	7.96×10^{-04}	**2.39×10^{-03}**	0.013	**0.019**	0.387	0.387
	ENSG00000095303	*PTGS1*	0.119	*not tested*		*not tested*		*not tested*	
	ENSG00000153707	*PTPRD*	3.30×10^{-03}	2.88×10^{-03}	**8.64×10^{-03}**	4.08×10^{-03}	**6.12×10^{-03}**	0.914	0.914
	ENSG00000174136	*RGMB*	1.96×10^{-03}	5.86×10^{-04}	**1.76×10^{-03}**	0.019	**0.028**	0.230	0.230
	ENSG00000163946	*TASOR*	0.075	*not tested*		*not tested*		*not tested*	
	ENSG00000131374	*TBC1D5*	2.47×10^{-03}	9.43×10^{-04}	**2.83×10^{-03}**	0.011	**0.016**	0.448	0.448
	ENSG00000140262	*TCF12*	2.09×10^{-03}	6.49×10^{-04}	**1.95×10^{-03}**	0.015	**0.022**	0.330	0.330
	ENSG00000100991	*TRPC4AP*	1.65×10^{-03}	4.34×10^{-04}	**1.30×10^{-03}**	0.020	**0.030**	0.234	0.234
	ENSG00000105939	*ZC3HAV1*	1.54×10^{-03}	3.89×10^{-04}	**1.17×10^{-03}**	0.021	**0.032**	0.213	0.213

Supplements

Allele-specific target genes of hsa-miR-4513-A and hsa-miR-4513-G identified in the RNA-Seq analysis were independently replicated by qRT-PCR. After a test for statistical significance by the Kruskal-Wallis test, a Dunn's multiple comparison test using the Benjamini and Hochberg method was performed. Significant p-values after adjustment are indicated in bold (adjusted p-value < 0.05).

Supplementary Table 10. Biological and medical relevance of allele-specific target genes of hsa-miR-4513 (Table modified from Kiel et al., 2021 [95]**).**

		MGI		
Gene symbol	**OMIM**	**Mouse phenotype**	**Molecular function (GO Term)**	**Biological process (GO Term)**
APOLD1	-	-	Lipid binding	cell differentiation, system development
CD2BP2	-	Human Diseases: 2x Autism; Mice homozygous for a knock-out allele exhibit lethality between E9.5 and E10.5. Mice homozygous for a conditional allele activated in podocytes exhibit proteinuria, weight loss, premature death, glomerulosclerosis, mesangial cell hyperplasia, renal tubule casts, and podocyte foot process effacement. Phenotypes: cardiovascular system, cellular, embryo, growth/size/body, hematopoietic system, homeostasis/metabolism, immune system, mortality/aging, renal/urinary system	-	-
CDKN2A	Melanoma and neural system tumor syndrome, Melanoma-pancreatic cancer syndrome, Melanoma cutaneous malignant	Null mutants of p16INK4a or p19ARF proteins each show increased tumor susceptibility and sensitivity to carcinogens. Loss of both gives very early onset. p19ARF nulls also show thymic hyperplasia and the eye's hyaloid vascular system fails to regress. Phenotypes: behavior/neurological, cellular, digestive/alimentary system, endocrine/exocrine system, hematopoietic system, homeostasis/metabolism, immune system, integument, mortality/aging, neoplasm, nervous system, renal/urinary system, reproductive system, respiratory system, skeleton, vision/eye	DNA binding, enzyme regulator, transferase	cell death, cell differentiation, cell population proliferation, cellular component organization, establishment of localization, homeostatic process, immune system process, nucleic acid-templated transcription, protein metabolic process, response to stimulus, signaling, system development
DDX46	-	-	carbohydrate derivative binding, hydrolase, RNA binding	-
FSTL1	-	Mice homozygous for a knock-out allele exhibit neonatal lethality, soft and enlarged trachea, cyanosis, primary atelectasis, lung epithelial cell hyperplasia, over-expanded bronchiole, impaired pneumocyte differentiation and maturation, and decreased surfactant	carbohydrate derivative binding	cell death, cell differentiation, homeostatic process, response to stimulus, signaling

		production. Phenotypes: behavior/neurological, cardiovascular system, embryo, growth/size/body, hematopoietic system, homeostasis/metabolism, immune system, integument, limbs/digits/tail, mortality/aging, muscle, nervous system, renal/urinary system, respiratory system, skeleton		
GTF3A	-	-	DNA binding, RNA binding	-
ITPRIPL2	*No entry*	-	*No data*	*No data*
KLF6	Gastric cancer, prostate cancer (both somatic)	Mice homozygous for a null allele exhibit embryonic lethality during organogenesis, small size, pallor, decreased cellular proliferation and delayed liver development. Mice heterozygous for a null allele exhibit delay in embryonic hematopoiesis. Phenotypes: cardiovascular system, cellular, embryo, endocrine/exocrine glands, growth/size/body, hematopoietic system, integument, liver/biliary system, mortality/aging, reproductive system	DNA binding, transcription	nucleic acid-templated transcription, response to stimulus, signaling
MAP4K4	-	Mice homozygous for disruptions in this gene die as embryos around day E9.5-10.5. Phenotypes: embryo, growth/size/body, limbs/digits/tail, mortality/aging	carbohydrate derivative binding, cytoskeletal protein binding, transferase	cell death, cell differentiation, cellular component organization, establishment of localization, homeostatic process, protein metabolic process, response to stimulus, signaling, system development
MCFD2	Factor V and factor VIII, combined deficiency of	Mice homozygous for a null allele exhibit decreased serum factor V and VIII and aspartate transaminase serum levels with accumulation of the proteins in the ER of hepatocytes. Phenotypes: homeostasis/metabolism	-	cell death, establishment of localization

MGAT4A	-	Mice homozygous for a knock-out allele show defects in glucose-stimulated insulin secretion, impaired cellular glucose import, increased susceptibility to weight gain, hyperglycemia, impaired glucose tolerance, insulin resistance, high free fatty acid and triglyceride levels, and hepatic steatosis. Phenotypes: Cellular, growth/size/body, homeostasis/metabolism, liver/biliary system	transferase	carbohydrate derivative metabolism, protein metabolic process
PTPRD	-	Homozygotes for a targeted null mutation exhibit impaired learning of spatial tasks, enhanced long-term potentiation at hippocampal synapses, and high mortality associated with reduced food intake. Phenotypes: adipose tissue, behavior/neurological, growth/size/body, homeostasis/metabolism, mortality/aging, nervous system, skeleton	hydrolase, signaling receptor binding	cell differentiation, cellular component organization, immune system process, protein metabolic process, response to stimulus, signaling, system development
RGMB	-	Mice homozygous for a knock-out allele exhibit lethality at 2 to 3 weeks after birth. Phenotypes: mortality/aging	signaling receptor activity	nucleic acid-templated transcription, response to stimulus, signaling
SEC63	polycystic liver disease	Mice homozygous for a knock-out allele exhibit early embryonic lethality. Mice homozygous for a conditional allele activated in the kidneys or ubiquitously develop polycystic kidney and liver phenotypes, respectively. Phenotypes: homeostasis/metabolism, liver/biliary system, mortality/aging, renal/urinary system	RNA binding, transporter	establishment of localization, system development

TBC1D5	-	Phenotypes: vision/eye (persistence of hyaloid vascular system)	enzyme regulator	cellular component organization, establishment of localization, response to stimulus
TCF12	Craniosynostosis	Mice homozygous for a targeted null mutation exhibit postnatal lethality within two weeks of birth and a 50% reduction in the number of pro-B cells. Phenotypes: behavior/neurological, endocrine/exocrine glands, growth/size/body, hematopoietic system, immune system, mortality/aging, nervous system	DNA binding, transcription	cell differentiation, nucleic acid-templated transcription, system development
TPM3	CAP myopathy, Myopathy (congenital, with fiber-type disproportion), Nemaline myopathy (autosomal dominant or recessive)	Homozygous inactivation of this gene results in early embryonic death, prior to blastocyst formation. Mice homozygous for a targeted allele lacking exon 9 exhibit dysmorphic T-tubules and contraction in skeletal muscles. Phenotypes: mortality/aging, muscle	cytoskeletal protein binding	cellular component organization
TRPC4AP	-	Female mice heterozygous for a knock-out allele exhibit anomalies in the growth phase of the hair cycle (anagen). Phenotypes: integument	-	protein metabolic process, system development

ZC3HAV1	-	Mice homozygous for a knock-out allele exhibit reduced murine leukemia virus replication efficiency in mouse embryonic fibroblasts. Phenotypes: cellular	RNA binding, transferase	immune system process, response to stimulus, signaling, system development

Publicly available databases like Online Mendelian Inheritance in Man (OMIM) [120] and Mouse Genome Informatics (MGI) [121] were screened for the biological and medical relevance of allele-specific target genes of hsa-miR-4513. GO = Gene Ontology.